國立臺灣大學工學院化學工程學系

碩士論文

Department of Chemical Engineering

College of Engineering

National Taiwan University

Master Thesis

鋰離子電池矽與氧化鋯複合負極材料製備與分析

Synthesis and Characterization of Zirconia-Silicon

Composite Anode Materials for Lithium-ion Batteries

郭家邦

Chia-Pang Kuo

指導教授：吳乃立 博士

Advisor: Nae-Lih Wu, Ph.D.

中華民國 102 年 7 月

July, 2013

致謝

　　致謝雖然是論文完成時的最後一筆，對我而言卻是整篇論文最重要的部分。整整碩士兩年加上大學專題一年的實驗室生活，經歷許多也得到許多，在此用淺薄的文字傳達這份感謝。

　　首先要感謝的是爸媽以及老師。沒有爸媽的栽培與鼓勵就沒有今天的我，沒有爸媽的開明與支持，我無法擇其所愛，愛其所擇。謝謝爸媽，希望你們後半生的歲月依然精采燦爛。再來要感謝的是老師，在跟隨老師三年多的時間，最重要的是學到獨立思考的能力，在看待各種事情都有自己獨到的見解，這點惠我良多；在學術上，學習到不只是鋰離子電池的相關概念，更重要的是材料合成與分析的專業與見解。雖然暫時得到一紙文憑，但我知道還有許多努力與改進的空間，從老師那學習到的經驗以及犯過的錯誤，都會成為我未來人生前進的動力，謝謝老師。

　　再來要感謝實驗室一起成長的夥伴們，最早領我進門做實驗的佑展，謝謝你不厭其煩的教導，印象很深刻是你告訴我 BET 是三個科學家名字的縮寫。還有很開朗對人情世故比較細心的彥伯，很優秀打球很厲害並且為新世代好男人的崧傑，籃下很強投影片製作更強的 artist 志毅，運球快到看不到而且電池壽命超長的維凱，個性溫和且博學多聞好像考不倒的榮川，籃球重砲手兼正極大師的文勤，生活經歷豐富喜歡分享的乃璇，很好相處人很有趣且多量多餐的均潔，思考謹慎且做事細心值得佩服的富生，又像爸爸又像哥哥的嘉男，積極做實驗且看很多 paper 的 HiHi，熱情帶有濃厚南部影子的光正，好像是麻將一哥的憲昌，幽默風趣且油而不膩的炯宏，兼修設計師和工程師的文青丹尼，已經在他國努力的 Erwin ，還有同梯的學長姐，怡萱、君睿(焦糖)、奕廷、小詹，你們真是帶給實驗室無限歡笑的模範專題生。還有同屆的彥霖，你的認真踏實值得我學習，而且細心仔細更是我所缺乏的，能跟你同屆共事是一件快活的事情，祝福你畢業後也

I

逐夢踏實。祝福後來加入的負極新生軍宏宥，正極新生軍勁良，實驗室目前僅存的電容一哥孝安，碩士班第二年是關鍵的一年，祝福你們實驗順利。至於剛升等成碩士班的子洋、朱昀，學長我想說：「還有兩年喔……哈哈。」另外感謝專題時期一起來能源材料實驗室的室友仲琪，同學彥勛，因緣際會一起在大學加入了 EML 大家庭，祝福你們發展順利。

另外要特別感謝研究生期間一直得到許多幫助的工研院材化所夥伴，如一直不辭辛勞幫我們的語婷，還有美如、靚瑜等，感謝你們，也感謝吳弘俊博士再合作其間的眾多幫忙。另外有幸在碩一時和偉仁、信良學長合作研究石墨烯材料，這個機會讓我學到許多，感謝你們。在儀器分析上也得到許多幫助，如粉粒體實驗室的綉雲姐和俊吉兄，謝謝你們教我若干儀器操作以及分析，讓我得以完成碩士論文研究；感謝貴儀積學館的素貞姐，在聊天的同時可以迅速拍出清楚的 SEM，這可是了不得的功力。

這份論文得以完善，必須感謝口試委員，老師、劉偉仁教授、吳弘俊博士，在口試的時候給與我許多寶貴的建議和指正，並且讓我更了解我研究的細部概念。最後要感謝也陪伴我三年的女友昭俐，給我無條件的支持和配合，讓我這三年過得踏實而穩定，在我辛苦的時候會為我加油打氣，謝謝妳。

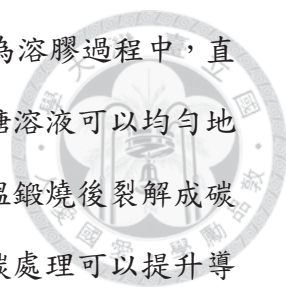謹以這份論文，紀念我的碩士生活，也紀念幫助過我的人們，謝謝你們！

家邦 謹記

2013/07/20

摘要

本論文的主要目的為開發以矽為主體的鋰離子二次電池負極材料,並且與氧化鋯形成複合材料以提高其振實密度及矽負極或矽碳複合負極的體積電容量密度。矽,擁有極高的理論質量電容量密度(大於 3600 mAh/g)、豐富的蘊藏量豐富及安全無毒性的特性,此外,隨著半導體產業成熟所伴隨的提煉技術進步,使其相對價格便宜,為目前極有可能取代石墨(372 mAh/g),成為新世代高電容量鋰離子電池的負極材料之一。但由於充放電時體積劇烈膨脹與低導電度,以及固相電解液介質(SEI)的負面影響,而造成極板結構不穩定以及充放電的電容不可逆性。這些原因使得鋰電池在應用上受到限制,為了克服這些問題,我們使用溶膠凝膠法製作矽與氧化鋯的複合材料,並且利用不同的鍍碳方式,改善氧化鋯不導電的特性,從而製作出一具高振實密度以及高充放電穩定性的矽基複合負極材料。

合成的概念在於將奈米級的矽顆粒與正丙醇鋯(氧化鋯的前驅物)混合均勻於異丙醇溶劑中,使用溶膠凝膠法於其中生成氧化鋯膠體,如此便可以得到矽與氧化鋯複合膠體。將此膠體於高溫鍛燒作緻密化處理,即可得到矽與氧化鋯複合負極材料。鍛燒後得到的複合粉體仍可維持其高孔隙度,並利用這些孔隙體積和氧化鋯的強機械強度,緩衝矽材在充放電過程中的不可逆膨脹。

首先,先從作出高孔隙度的氧化鋯氣凝膠(aerogel)著手,在不使用超臨界流體乾燥法的情況下(常見於製作高孔隙度的凝膠),簡化實驗流程,調整溶膠凝膠法製作凝膠中的各種重要因素,如前驅物濃度、粉體鍛燒溫度、含水量、凝膠狀態等,達到製程最佳化的目標,並且得到高孔隙度的氧化鋯粉體。此外,在真空環境下鍛燒,達到高溫鍛燒(大於 500 度)仍可維持粉體孔隙度的結果。之後,以這些實驗參數為基礎,將奈米級矽顆粒加入凝膠混合均勻,乾燥後將膠體作高溫鍛燒處理得到高孔隙度的矽-氧化鋯粉體。

　　此外，兩種鍍碳方式分別為果糖鍍碳以及瀝青鍍碳。前者為溶膠過程中，直接浸泡穩定的矽與氧化鋯膠體(鍛燒前)於果糖溶液中，使得果糖溶液可以均勻地分散於高孔隙度的膠體中，並且在矽表面形成果糖包覆，在高溫鍛燒後裂解成碳層包覆並得到矽-氧化鋯-碳複合材料，實驗結果顯示，經過鍍碳處理可以提升導電度並大幅降低矽基電極阻抗。後者為將矽與氧化鋯膠體先進行第一步低溫鍛燒(400 度)，得到矽與氧化鋯粉體後再與瀝青丙酮溶液混合，乾燥後做第二次鍛燒，將瀝青裂解成碳而得到矽-氧化鋯-碳複合材料，實驗結果顯示，瀝青分解的碳能填滿孔洞體積，以達到降低表面積並降低 SEI 膜生成而導致的不可逆。

　　此外，兩種不一樣的奈米級矽原料的使用，也於本論文中探討。實驗結果顯示，矽-氧化鋯-碳複合負極樣品在 50 圈的充放電後，仍然可以維持 70% 的電容量。

關鍵字: 鋰離子二次電池，矽，溶膠凝膠法，氧化鋯氣凝膠，複合負極材料。

Abstract

The main purpose of this research is to develop a high tap-density anode material based on silicon for lithium ion batteries. Silicon, in addition to its abundance on earth and its environmentally-friendly property, it also possesses a high theoretical capacity (> 3600 mAh/g) compared to graphite (372 mAh/g). However, the dramatic volumetric variations during cycling and intrinsic low conductivity result in structural instability and poor cyclability. Moreover, the irreversibility caused by solid electrolyte interphase (SEI) formation accelerates the capacity fading as well. In order to solve those problems, we use sol-gel process to make a porous zirconia-silicon composite material and use different carbon coating process to improve the electronic insulation property of zirconia.

To synthesize Si-ZrO$_2$ composite, nano-sized Si is dispersed in iso-propanol and at the same time, the zirconia gel forms by sol-gel method with zirconium propoxide as precursor. After deriving Si-ZrO$_2$ gel, high temperature treatment is conducted to have porous Si-ZrO$_2$ powder. The pore volume and strong mechanical property of zirconia are utilized to buffer the irreversible expansion of Si during cycling.

The preliminary work is to make a porous zirconia which can provide sufficient pore volume for buffering expansion of Si. This research has developed a rather-simple process (without supercritical drying, which is typically regarded as indispensable drying method for deriving aerogel) by controlling several important factors in sol-gel process, such as concentration of precursor, calcination temperature, water content, and gel state to derive porous zirconia. Besides, high-temperature treatment under vacuum environment can preserve more pore volume than that under 3% H$_2$/N$_2$ environment (T > 500℃). After all the factors are well studied, the

silicon is mixed with zirconia aerogel and then calcined to have porous $Si-ZrO_2$ composite powder.

Besides, carbon coating methods consist of fructose carbon coating and pitch carbon coating. The former one is directly soaking stable $Si-ZrO_2$ gel in fructose solution and the fructose solution can permeate into the porous gel and form a fructose layer on Si surface. The fructose layer decomposes into carbon layer after high temperature treatment. The experimental result indicates that the impedance of $Si-ZrO_2$ electrode decreases a lot with increasing conductivity of $Si-ZrO_2-C$. Different from fructose carbon coating, pitch carbon coating adopted two-step calcinations. $Si-ZrO_2$ proceeds the 1st calcination under low temperature (400℃) to have $Si-ZrO_2$ powder and then the powder is mixed with pitch in acetone solution. After drying process, the collected powder proceeds the 2nd calcination to have $Si-ZrO_2-C$. The experimental result shows that the dissociated carbon indeed fills the pore volume and reduces the surface area of porous $Si-ZrO_2$ structure to improve the irreversible capacity from SEI formation.

Last, two kinds of nano silicon with different sizes and qualities are used to form $Si-ZrO_2-C$ composite. The experimental result shows that $Si-ZrO_2-C$ electrode can retain 70% of 1st cycle charge capacity after running 50 cycles.

Table of Contents

Lists of Tables

Lists of Figures

XIV

XVII

XVIII

Chapter 1 Introduction

1.1 Background

Nowadays, technological improvements in rechargeable solid-state batteries are being driven by an ever-increasing demand for portable electronic devices. Lithium-ion batteries (LIBs) are the systems of choice, offering high energy density, high efficiency, flexible and lightweight design, and longer lifespan than comparable battery technologies [1]. These unique properties have made LIBs the power sources of choice for the consumer electronics market with a production of the order of billions of units per year. These batteries are also expected to find a prominent role as ideal electrochemical storage systems in renewable energy plants, as well as power systems for zero emission vehicles, *i.e.* electric vehicles (EVs) or for controlled emission vehicles, *i.e.* hybrid electric vehicles (HEVs) and plug-in electric vehicles (PHEVs) [2].

1.2 Motivation and Objectives

Graphitic carbon has become the material of choice for anode (negative electrode) in the present generation of Li-ion cells. The long-term cycle stability, high reversibility, low cost, and large abundance have made graphitic carbon an attractive anode. Despite the advantages and the advances made in graphite, it has been recognized for some years now that new anode materials are needed. First, graphite suffers from a fundamental limitation in gravimetric capacity and particular in volumetric capacity (theoretical limit of 372 mAh/g and 830 mAh/cc) [3]. More importantly, an increase in the operating voltage above the current values for graphite is highly desirable to inhibit Li metal deposition that can occur at fast rates. The unsafe condition can arise in Li-ion cells that operate with a fully lithiated graphite electrode. If the cells in those batteries are overcharged, especially in large-scale applications, thermal runaway, venting, fire, and explosion could result [4].

With respect to anode materials, metal alloys or intermetallic compounds are attractive alternatives to graphite because they can be selected to operate between 0 and 1 volt above the potential of metallic lithium. Many intermetallic compounds, particularly the binary systems, Li_xM (*e.g.* M = Al, Si, Sn, Sb, Pb) have already been thoroughly investigated [5]. Among them, Silicon is one of the most promising candidates for the next generation of LIBs because of its environmental benignity, great abundance and particularly, excellent high theoretical capacity ($Li_{15}Si_4$, 3579 mAh/g [7] or $Li_{22}Si_5$, 4200 mAh/g [6]). Despite of these favorable features, several problems are encountered for Si anode materials: one is the extremely volume variation (> 250%) during charge/discharge cycling and the other is the low electronic conductivity (~10^{-5} S/cm). The former is claimed to cause poor cycle-life and the latter results in high resistance and low Li uptake. In addition, the irreversibility

caused from solid electrolyte interphase (SEI) formation also speed up the capacity fading rate of Si anodes. These three issues are the Achilles' heel of Si anodes for further commercial applications.
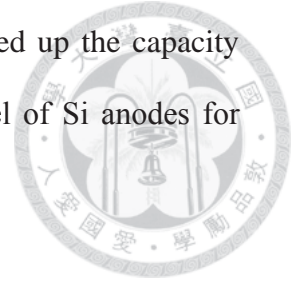
Chapter 2 Theory and Literature Review

2.1 Introduction of Sol-Gel Method

The sol-gel process is a wet-chemical technique that widely used in the fields of material science and ceramic engineering. Such methods are used primarily for the fabrication of materials starting from colloidal solution (sol) that acts as the precursor for an integrated network (gel) of either discrete particles or network polymers. Typical precursors are metal alkoxides and metal salts (such as chlorides, nitrates and acetates), which undergo various forms of hydrolysis and polycondensation reactions [7].

2.1.1 Definition

Sol-gel can be viewed as a colloid system that consists of solute and solvent or a dispersed system that consists of dispersed phase and dispersed medium. And dispersed system can be basically classified to 8 types as Table 2.1 [8].

Sol is actually solid dispersed in liquid, and it can be lyophilic sol or lyophobic sol. The former one has stronger attraction between dispersed phase and dispersed medium. Therefore, solvation could easily happen and make the system stable, for example, starch solution. And the latter one has weaker interaction between dispersed phase and medium. The dispersion exists due to the presence of repulsion of dispersed phase with same charge. Once we add strong electrolyte into the solution, the dispersed phase might sediment due to the neutralization between dispersed phase and ions dissociated from electrolyte. A normal sol-gel process should include several steps as follow [7]:

4

1. Hydrolysis: Hydrolysis means the cleavage of chemical bonds by the addition of water, and in this step, one fragment of the target molecule gains a hydrogen ion.

2. Condensation: A process by which two molecules join together resulting loss of small molecules which is often water or methanol. The type of end product resulting from a condensation polymerization is dependent on the number of functional end groups of the monomer which can react. Monomers with only one reactive group terminate a growing chain, and thus give end products with a lower molecular weight. Linear polymers are created using monomers with two reactive end groups and monomers with more than two end groups give three dimensional polymer which are crosslinked.

3. Gelation : Formation of a "spanning cluster" across the vessel, giving a network which entraps the remaining solution, with high viscosity.

4. Ageing: A range of process, including formation of further cross-links, associated shrinkage of the gel as covalent links replace non-bonded contacts, Ostwald ripening and structural evolution with changes in pore sized and pore wall strengths.

5. Drying: The loss of water, alcohol and other volatile components, first as syneresis (expulsion of the liquid as the gel shrinks), then as evaporation of liquid from within the pore structure with associated development of capillary stress which frequently leads to cracking. This may also include supercritical drying, in which capillary stress is avoided by the use of supercritical fluids (e.g. CO_2) in conditions where there are no liquid-vapor interfaces.

6. Densification: Thermal treatment leading to collapse of the open structure and formation of a dense ceramics.

The properties of sol-gel materials, e.g. transparency, porosity, pore size distribution, surface functionality, strongly depend on the preparation method. By controlling the conditions during the subsequent stages of the process: hydrolysis,

condensation, ageing, drying, one can fine tune the characteristics of the resulting material. The specific introduction of mechanism and control would be presented in the following chapters.
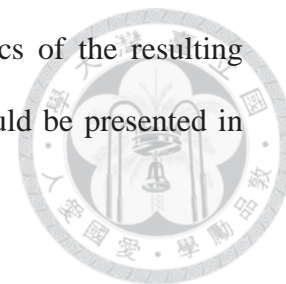
Table 2.1 Classic types of sol-gel system and examples [8].

No.	Dispersed Phase	Dispersed Medium	Name	Examples
1.	L	G	Aerosol	Fog, Mist
2.	S	G	Solid Aerosol	Dust, Smoke
3.	G	L	Foam	Shaving cream
4.	L	L	Emulsion	Milk, Mayonnaise
5.	S	L	Sol	Blood, Mud
6.	G	S	Solid Foam	Dry sponge
7.	L	S	Gel	Wet sponge
8.	S	S	Sold Gel	Rubic, Granite

2.1.2 Different Precursors: Metal Salt and Metal Alkoxide

There are mainly two kinds of precursor, metal salt and metal alkoxide, in sol-gel process. There are pros and cons among two different kinds of precursors. For example, metal alkoxide is expensive and too sensitive to reaction condition to be controlled but a better precursor for deriving high purity metal oxide. Instead, metal salt is rather cheap and less reactive. However, it needs more water to remove unnecessary ions that would affect the quality of product .

The reactivity difference of alkoxide and salt comes from their different electron affinity of metal ion [9]. For metal salt, only being paired with highly electronegative anion can it form stable complex. In contrast, the central metal ion in alkoxide usually has lower electron affinity and the electron cloud is easier to be polarized to form stable complex.

The partial charge model has indicated that the charge of every single atom in a molecule can be calculated [10]. Once two atoms with different electronegativity (EN) link to each other to form a bond, the charge starts to move from high-EN atom to low-EN atom. After the high-EN acquire partial charge, its EN decrease, meanwhile the opposite one increase. Thus, their EN would reach a medium value and no more charge transfer. At this point, the atoms have acquired partial charge, The electronegativity of an atom is related to its partial charge by an equation which is not specifically introduced here. But the spirit of this model is to predict whether the reaction (hydrolysis and condensation) would happen or not. For instance, alkoxide is easier to do nucleophilic substitution with water molecule due to the electronegativity of alkyl groups. As presented in Fig.2.1 [11], the overall process depends on charge distribution and transition state. During the transition state, both $\delta(ROH)$ and $\delta(M)$ are positive is indispensable to separating ROH from metal ion. Therefore, it indicate that

larger δ(ROH) could boost the separating rate.

On the other hand, Table 2.2 shows the essential partial positive charge, δ(M), on the central atom in a series of metal ethoxides [12]. This means that the rate of nucleophilic attack on the central atom of metal alkoxides and related precursors is much faster than that on silicon alkoxide precursors (e.g. hydrolysis rate constants at pH 7 are 5×10^{-9} $M^{-1}s^{-1}$ for Si(OEt)$_4$ and 10^{-3} $M^{-1}s^{-1}$ for Ti(OEt)$_4$), and that hydrated metal ions have an increasing tendency toward acid dissociation as electropositive character of the metal increases.

$$[M...OH_2]^{z+} \rightleftharpoons [M-OH]^{(z-1)+} + H^+ \rightleftharpoons [M=O]^{(z-2)+} + 2H^+ \qquad (2\text{-}1)$$
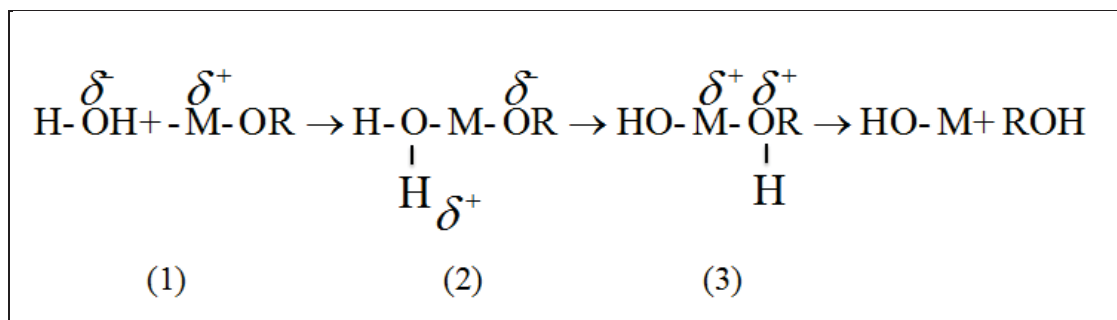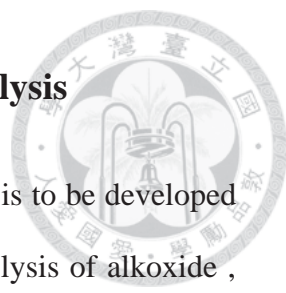
Figure 2.1 The mechanism of nucleophilic substitution in hydrolysis. (1) water molecule temporarily links to alkoxide (2) proton (H+) transfer from entering group (H$_2$O) to leaving group (OR) (3) cleavage of partially positive-charge group [11].

Table 2.2 Estimated partial positive charge of different metal ethoxide [12]

Ethoxide	Zr(OEt)$_4$	Ti(OEt)$_4$	Nb(OEt)$_5$	Ta(OEt)$_5$	Vo(OEt)$_3$	W(OEt)$_6$	Si(OEt)$_4$
δ(M)	+0.65	+0.63	+0.53	+0.49	+0.46	+0.43	+0.32

2.1.3 Hydrolysis : Mechanism of Acidic and Basic Catalysis

Reaction mechanisms must be considered if sol-gel chemistry is to be developed as anything other than an empirical art. The first step of the hydrolysis of alkoxide , e.g. silicon alkoxide, can occur by acid catalysed or base-catalysed process, as shown in Fig 2.2 [9]. The effect of catalysis may be judged by comparing the rate of reacton at different pH values, bearing in mind that the isoelectripic point of silica (where the equilibrium species has zero net charge) is at pH 2.2. Although it is only a crude measure of the relative hydrolysis rates because it includes both hydrolysis and condensation. The time to form a gel (T_{gel}) gives an indication of the relative rates, as shown in Fig. 2.3[9].

The rate trends in acid and base catalysed processes for successive hydrolysis of the four groups around Si can be understood in terms of electronic effects. Alkoxy groups are more electron donating than hydroxyl groups. Thur for the positively-charged transition state of the acid-catalysed reaction, as more alkoxy groups are replaced by hydroxyl groups the transition state becomes less stabilized and the reaction rate decreases. Conversely, for the negatively-charged transition state of the base-catalyzed reaction, more OH groups mean more stabilization of the transition state of the base-catalyzed reaction, more OH groups mean more stabilization of the transition state and faster reaction. Similar arguments obviously show that the reverse esterfication reactions are more likely in acidic conditions, where esterfication stabilizes the transition state, than in basic conditions.
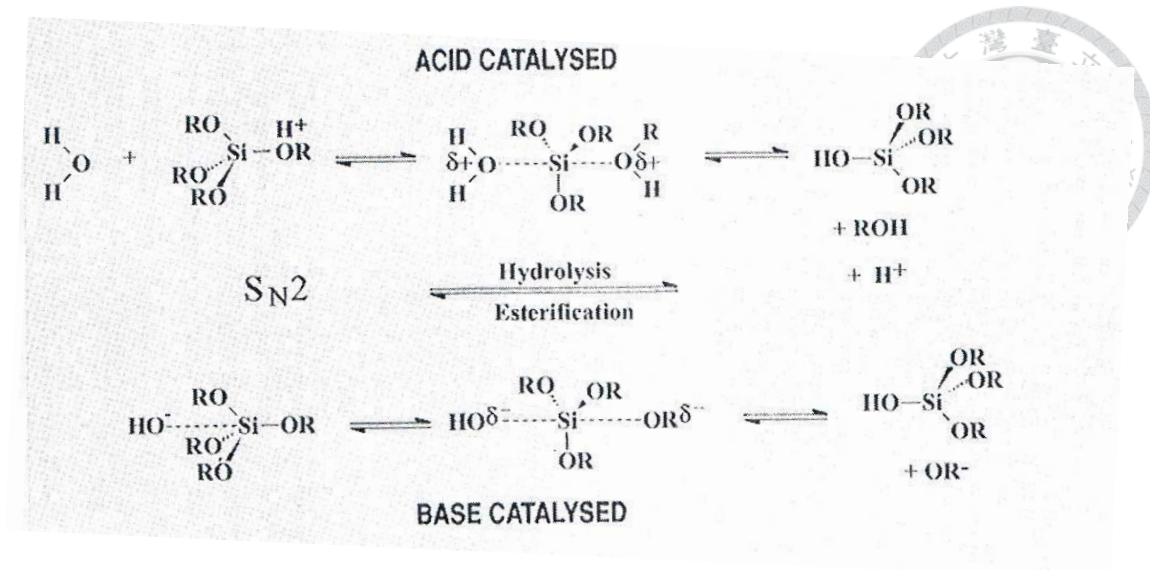
Figure 2.2 Hydrolysis mechanism in sol-gel process [9].
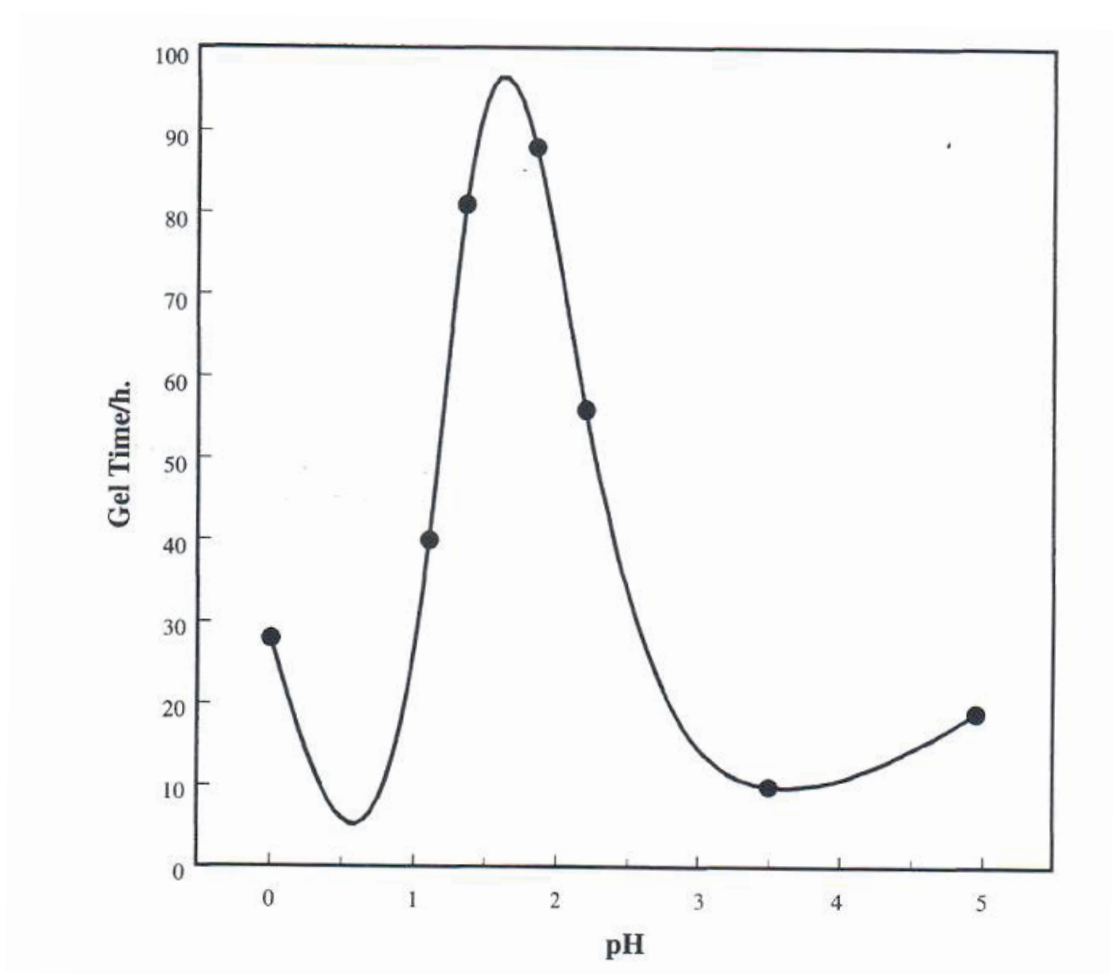
Figure 2.3 Gel time as function of pH for HCl-catalyzed TEOS (H2O:TEOS ratio, R=4) [9].

2.1.4 Hydrolysis : Controllable Factors

Besides the different pH value or catalyst, there are still lots factors affecting hydrolysis, for example, temperature, precursor, co-solvent, water content, etc. One of the most important things in doing sol-gel process is to picking up the important factor and letting other ones remain the same or ever more, neglecting them.

One important fact is on the precursor itself. Besides the partial charge model we have mentioned in chapter 2.1.2. "Precursor substituent" also plays an important role in controlling hydrolysis rate. For example, when the rates of hydrolysis of different silicon alkoxides are compared, it is found that the steric bulk of the alkoxy group exerts a large influence. Larger alkoxy groups lead to more steric hindrance and overcrowding of the transition state, and thus lead to slower reactions. Thus tetramethoxy silane (TMOS) hydrolyses faster than tetraethoxy silane(TEOS) and concerned experimental data is presented in Table 2.3 [13].

The co-solvent effect is simple to be understood. Some alkoxide is hard to dissolve in water. Thus it needs a medium, usually alcohol, which can homogeneously mix with both water and precursor. As seen from Fig. 2.4-a, the ratio of water : alkoxide determines the amount of co-solvent required, but this ratio also influences the reaction rate. The stoichiometric ratio of water:alkoxide for complete hydrolysis is 4. If the amount of water becomes very small, however, the hydrolysis rate slows down due to the reduced reactant concentrations. Similarly, if very large amounts of water are used the other reactant (alkoxide) is effectively diluted and gel times increase (Fig 2.4-b). However, less water than this can be used since the condensation reaction leads to production of water.

Neglecting the co-solvent effect, the water content in the solution can adjust the hydrolysis rate directly. The ratio of water and metal ion concentration (water/M =WR)

is usually adopted as a factor which can reflct the hydrolysis rate. For small WR, the hydrolysis rate is rather slow than condensation, so long-chain polymer usually form. For large WR, a 3D spatial net work usually forms. Thus, a basic idea is that enough amount of water content can guarantee larger gel which can also resist the capillary stress during drying by its strong network structure. However, the actual number of appropriate WR depends is affected by several number. Therefore, hydrolysis rate, h, is used to specifically explain the possible situation with different water content. For example, $M(OR)_n$ as a precursor, there are three situation [14,15]: (1) h<1 : in this range, there are more -M-OR groups than –M-OH groups which is important for pushing condensation happen (i.e. higher reactivity toward condensation). Therefore, it's hard to form a network structure during this range of h. Furthermore, the gel hardly from even for longer time. (2)1<h<n : In this range, there usually form olated polymers, and with longer reaction time, the residual solvent generated from condensation could be excludes which is beneficial for gel formation. (3) h>n : Adding too much water leads to precipitation due to large amount of -M-OH groups and it's hard to form gel.

Table 2.3 Hydrolysis rate of different Si $(OR)_4$ under the same reaction condition [9]

R =	Hydrolysis rate constant / 10^{-2} M^{-1} · s^{-1} · [H$^+$]$^{-1}$
C_2H_5-	5.1
C_4H_9-	1.9
C_6H_{13}-	0.83
$(CH_3)_2CH(CH_2)_3CH(CH_3)CH_2$-	0.30
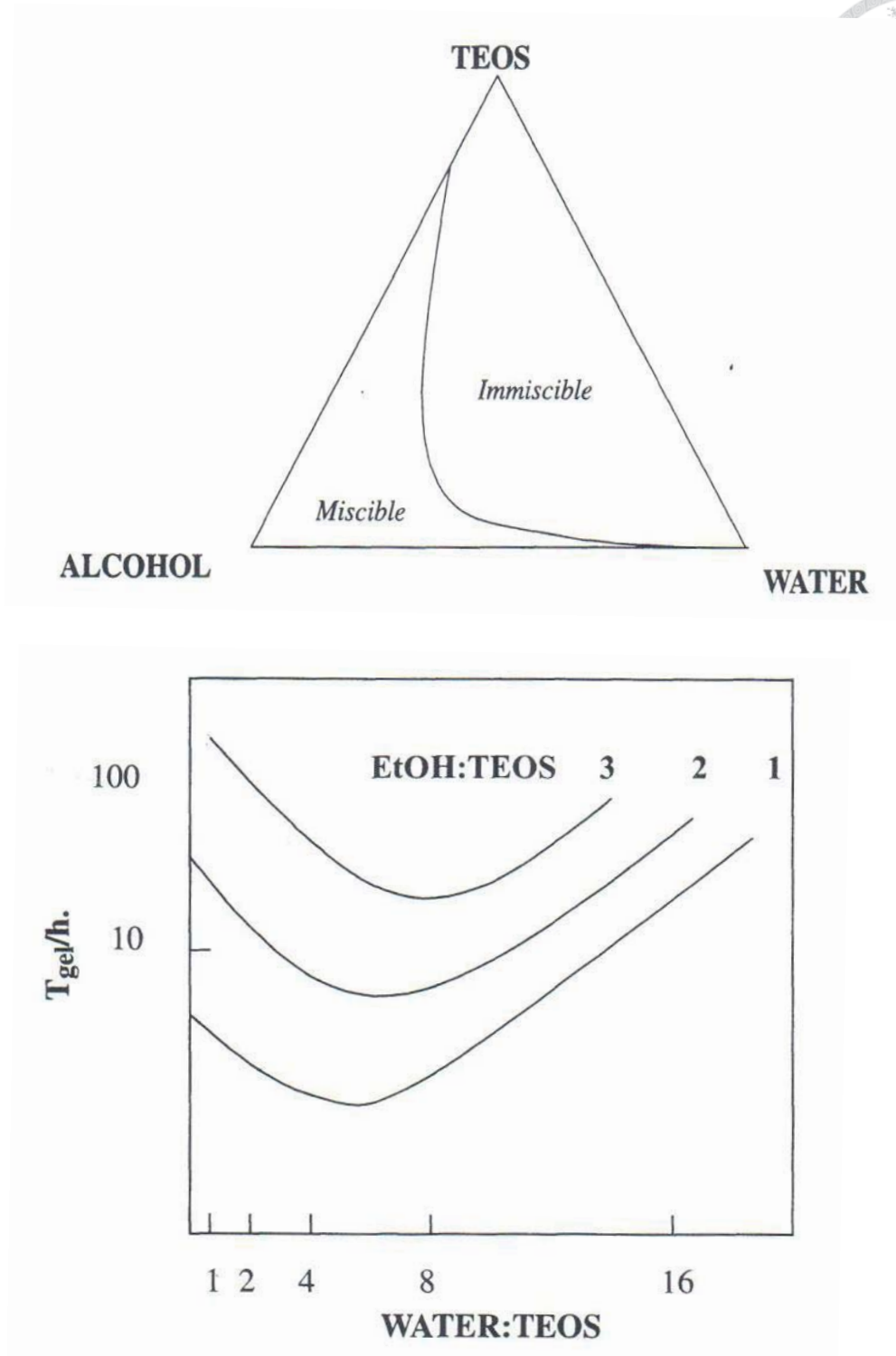
Figure 2.4 (a) The phase diagram for TEOS (b) The gel time vs. water：TEOS ratio under different ETOH:TEOS ratio [9].

2.1.5 Condensation：Mechanism of Acidic and Basic Catalysis

Condensation reaction can be either water condensation or alcohol condensation：

(R_1 : H or other alkyl group)

$$M(OR)_{n-1}OR_1 + HOM(OR)_{n-1} \rightleftharpoons (RO)_{n-1}MOM(OR)_{n-1} + R_1OH \qquad (2\text{-}2)$$

The reverse reactions are hydrolysis and alcoholysis, respectively. As with initial hydrolysis, condensation reactions may be acid or base catalysed, and in either case the reaction proceeds via a rapid formation of a charged intermediate by reaction with a proton or hydroxide ion, followed by slow attack of a second neutral species on this intermediate. (See Fig. 2.5)
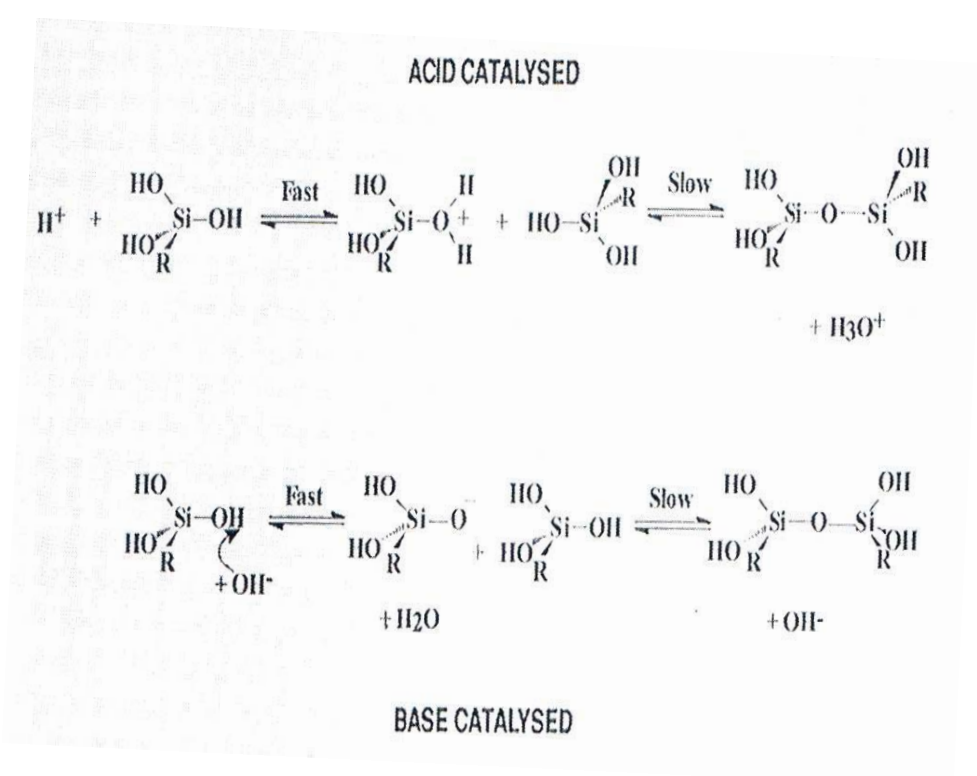
Figure 2.5 Condensation mechanism in sol-gel process [9]
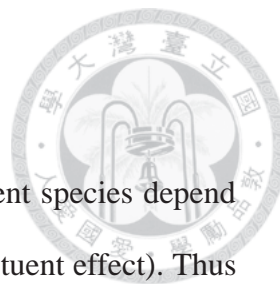
2.1.6 Condensation : Controllable Factors

Just as with hydrolysis, the relative rates of reaction of different species depend on steric effects and the charge on the transition state (i.e. the substituent effect). Thus for acid hydrolysis with a positively charged transition state stabilized by electron donating groups, $(RO)_{n-1}M(OH)$ condenses faster than $(RO)_{n-2}M(OH)_2$, which condenses faster than $(RO)_{n-3}M(OH)_3$,etc. This means that for acid catalyzed reactions, the first step of the hydrolysis is the fastest, and the product of this first step also undergoes the fastest condensation. Hence an open network structure results initially, followed by further hydrolysis and cross-condensation reactions. In contrast, in base catalyzed conditions the negatively charged transition state becomes more stable as more hydroxyl groups replace the electron donating alkoxy groups. Thurs successive hydrolysis steps occur increasingly rapidly, and the fully hydrolyzed species undergoes the fastest condensation reactions. As a consequence, in base catalyzed reactions highly cross-linked large sol-particles are initially obtained which eventually link to form gels with large pores between the interconnected particles [9].(See Fig. 2.6) Hence the choice of acid or base catalysis has a substantial influence on the nature of the gel which is formed.

The alkoxide ligand itself can be used to control reaction rates via both its electronic and steric influence. Thus, increasing the alkyl chain length increases the electron donating ability and reduces the charges on the metal and the transferred proton, as well as increasing the steric bulk of the alkoxy group. All of these factors slow both hydrolysis and condensation reactions, to the extent that for larger groups. Phenoxy compounds are generally found to give slower hydrolysis than alkoxides, in marked contrast to the faster hydrolysis of silicon phenoxide than TEOS. In the silicon compound the negative inductive effect of the phenoxy group dominates,

15

giving larger positive charge on Si and hence faster reaction. However, for metals with d orbitals which can act as π-acceptors for the aromatic ring electrons of the phenoxy group, this effect dominates, reducing the positive charge on the metal and decreasing the reactivity. Finer control is achievable via the use of chelating ligands which form mixed complexes with alkoxide ligand, the chelating ligands being more inert towards displacement and this providing control of the main condensation path way.

A particularly elegant example is the use of acetylacetone to modify the reactivity of tetra(i-proxy)titanium(IV). Addition of one mole of acetylacetone leads to a $(TiOPr^i)_3(acac)$ complex whereas, with tow moles of acetylacetone, $Ti(OPr^i)_2(acac)_2$ is formed [16,17].
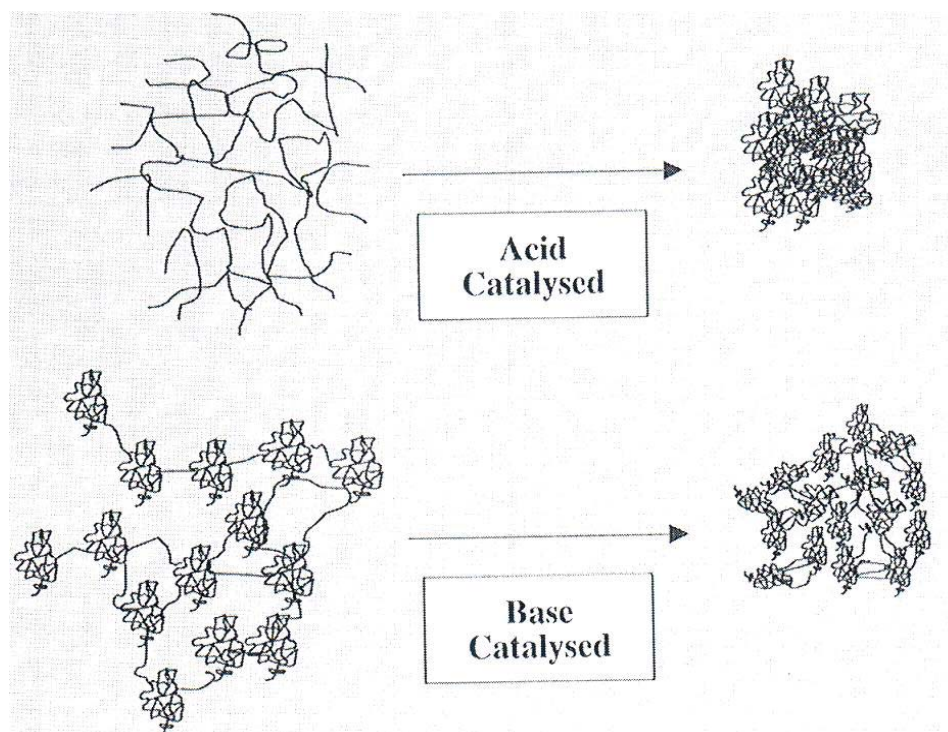
Figure 2.6 The possible microstructural illustration of gel with different catalysis conditions [9].

2.1.7 Gelation

Gelation occurs when links form between sol particles, produced by hydrolysis and condensation, to such an extent that a giant spanning cluster reaches across containing vessel. At this point, although the mixture has a high viscosity so that it does not pour when the vessel is tipped, many sol particles are still present as such, entrapped and entangled in the spanning cluster. This initial gel has a viscosity but low elasticity. There is no exotherm or endotherm, nor any discrete chemical change, at the gel point; only the sudden viscosity increase (See Fig. 2.7[9]). Following gelation, further cross-linking and chemical inclusion of isolated sol particles into the spanning cluster continues, leading to an increase in the elasticity of the sample precise definition of terms such as "gel-point" and "gelling time" with reference to attainment of a particular viscosity value is elusive and probably of little absolute significance.
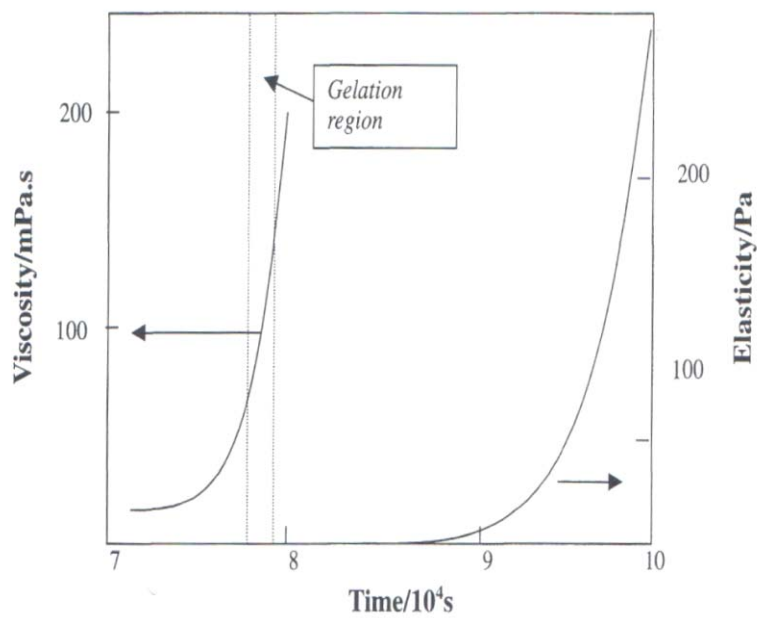
Figure 2.7 The viscosity and elasticity change in relation to gelatoin (TEOS as the precursor) [9].

2.1.8 Ageing

Although understanding of gelation is important in applications requiring processing of either fluid (e.g. spin- or dip-coating) or self-supporting (e.g. casting) precursors, the continuing chemical and physical changes during ageing after gelation are of even more importances. NMR studies of gelled samples [18] show a continuing gradual increase in the number of Q3 and Q4 Si species (i.e. Si attached via 4 oxygen links to three and four other silicon atoms), due to cross-linking via trans-pore condensation reactions of pore-surface hydroxyl groups. This can continue for months for samples at room temperature, the rate depending on pH, temperature and gel composition. The net effect of these processs is a stiffening and shrinkage of the sample. Shrinkage occurs because new bonds are formed where there were formerly only weak interactions between surface hydroxyl and alkoxy groups. This shrinkage leads to expulsion of liquid from the pores of the gel, so that gel samples in sealed containers gradually change in appearance from homogeneous gels to transparent shrunken solid monoliths immersed in liquid. This process is known as syneresis.

Another process associated with ageing is often referred to as coarsening or ripening. In this process, material dissolves from the surface of large particles and deposits on the initially narrow "necks" which join particles to each other.

A final ageing effect may be phase transformation. Where gelation has occurred very quickly (e.g. in base catalysed conditions) or where several precursors of different miscibility with water have been used, there is a possibility that the porous gel contains isolated regions of unreacted precursor. On prolonged soaking in water, this material may react either completely or partially, giving inclusions of material of different structure and composition. If the refractive index of such regions is sufficiently different from that of the host matrix, the whole sample may have a white

opaque appearance characteristic of a phase-separated material. This undesirable situation may be avoided by modifying the reaction rate (e.g. by dilution or pH control) and use of more effective co-solvents in the initial mixture [9].
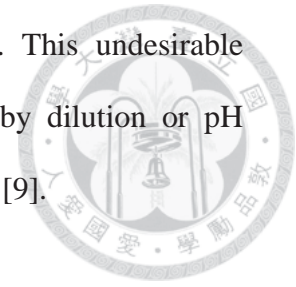
2.1.9 Drying

Basically, drying process can be separated into four stages : (i) the constant rate period (ii) the critical point (iii) first-falling-rate period (iv) second falling-rate period [9]. Here introduce the main parts, (i) and (ii), relating to this research.

During (i) the constant period, initially a gel will shrink by an amount equal to the volume of solvent or other liquid which has evaporated. This phase can only occur in gels which are still very flexible and compliant, and able to adjust to the reduced volume. Note that gels may also shrink faster than the water can evaporate if rapid cross-linking and syneresis is occurring If the gel has become rigid due to cross-linking by the time the excess solvent has evaporated, the constant rate period may cease as soon as the excess solvent arising from syneresis has evaporated. In this case the pore size distribution will be strongly influenced by the cross-linking, whereas gels which shrink by evaporation of water from compliant structures will suffer pore collapse as shrinkage proceeds.

As the gel dries and shrinks, its more compact structure and associated additional cross-linking lead to increased stiffness. At the critical point, the gel becomes sufficiently stiff to resist further shrinkage as liquid continues to evaporate. At this point the liquid begins to recede into the porous structure of the gel. Due to its surface tension and the small size of the gel pores, very large pressures are generated across the curved interfaces of the liquid menisci in the pores. For a typical silica sol-gel

sample of surface area several hundred m^2/g, the forces may exceed 100MPa (i.e. around 1000 atmosphere pressure). Unless the gel has been very carefully prepared to have optimum cross-linking, as well as been very carefully aged, it will crack due to this capillary stress.

On the other hand, since it is the small pores which contribute most to capillary stress, synthesis of gels with large pores (greater than 50 nm) would yield substantial benefits in reducing cracking. For example, mixing a commercial colloidal silica with potassium silicate at high pH and gelling by addition of formamide gives a product in which silicate polymers are nucleated from solution by the silica colloid. Controlled pore sizes between 10 and 360nm were obtained by controlling the ratio of the two starting materials, and the samples with pore sizes greater than 60nm could be dried rapidly without cracking, even in dimensions of many centimeters [19].

2.1.10 Densificatoin

A heat treatment (i.e. densification) is usually conducted when the gel is at the end of drying process and three typical stages are observed by the measurement of linear shrinkage and weight loss as a function of temperature. See Fig. 2.8.

At low temperature (typically $< 200℃$), weight loss occurs as pore surface water or alcohol is desorbed, but with little further shrinkage takes place. At intermediate temperature in the rage from 150-200℃ to typically 500-700℃, samples generally show both weight loss and shrinkage. Three processes occur in this range: loss of organics (leading to weight loss but little shrinkage), further condensation (producing both weight loss and shrinkage) and structural relaxation (giving shrinkage with no associated weight loss). The loss of organics proves that the matrix is still porous in

20

this stage. The spaces previously occupied by the organic species now become pores with similar size and shape to the organics themselves. These "molecular footprints" have been used for generating small pore sizes. However, structural relaxation and further trans-pore condensations gradually lead to the footprints fading, particularly at elevated temperature such as are used for catalytic process.

At temperature above the upper limit for region II behaviors, a sharp increase in shrinkage is observed with little or no further weight loss. The transition temperature is close to the glass transition temperature for the material, above which viscous flow occurs leading to rapid densificaton as thermal energy permits extended structural reorganization. The densification process is strongly favored thermodynamically because of the very large reduction in surface area of the material and the associated large reduction in interfacial energy. The extent of this final shrinkage, as well as the temperature at which it begins, is dependent on the structure of the material at the end of region II and thus on the conditions for all the stages in the process which have been described up to this point. Clearly many variables are involved, and in principle this provides great scope for fine control of the onset and nature of the densification process, which has been widely exploited in ceramic processing.
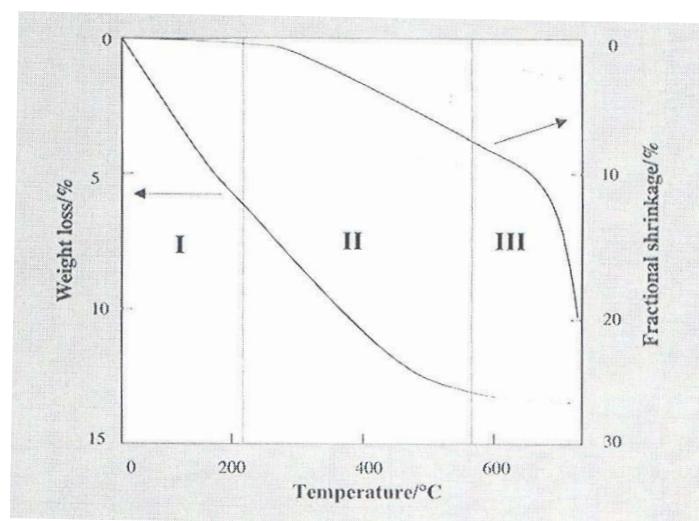
Figure 2.8 Typical stages of densification of silica gel [9].

2.2 Historical Developments of Preparing ZrO$_2$ by Sol-Gel Method

2.2.1 Properties of ZrO$_2$

The basic properties of ZrO$_2$ is illustrated in Table 2.4. Zirconia is chemically unreactive. It is slowly attacked by concentrated hydrofluoric acid and sulfuric acid. When heated with carbon, it converts to zirconium carbide. When heated with carbon in the presence of chlorine, it converts to zirconium tetrachloride. This conversion is the basis for the purification of zirconium metal and is analogous to the Kroll process [20]. Besides, the typical crystal structure of ZrO$_2$ and its phase transformation with different temperature are already well-known. See Fig. 2.9 [21].

The main use of zirconia is in the production of ceramics, with other uses including as a protective coating on particles of titanium dioxide pigments, as a refractory material, in insulation, abrasives and enamels. Stabilized zirconia is used in oxygen sensors and fuel cell membranes because it has the ability to allow oxygen ions to move freely through the crystal structure at high temperatures. This high ionic conductivity (and a low electronic conductivity) makes it one of the most useful electroceramics. Zirconia is a precursor to the electroceramic lead zirconate titanate ("PZT"), which is a high-K dielectric, which is found in myriad components [22].

Table 2.4 Fundamental properties of ZrO_2 [20]

IUPAC Name	Zirconium Dioxide
Molar Mass	123.218 g/mol
Appearance	White powders
Density	5.68 g/cm3 in monoclinic phase
Melting Point	2715℃
Boiling Point	4300℃
Solubility in water	Negligible (soluble in HF)
Refractive Index	2.13
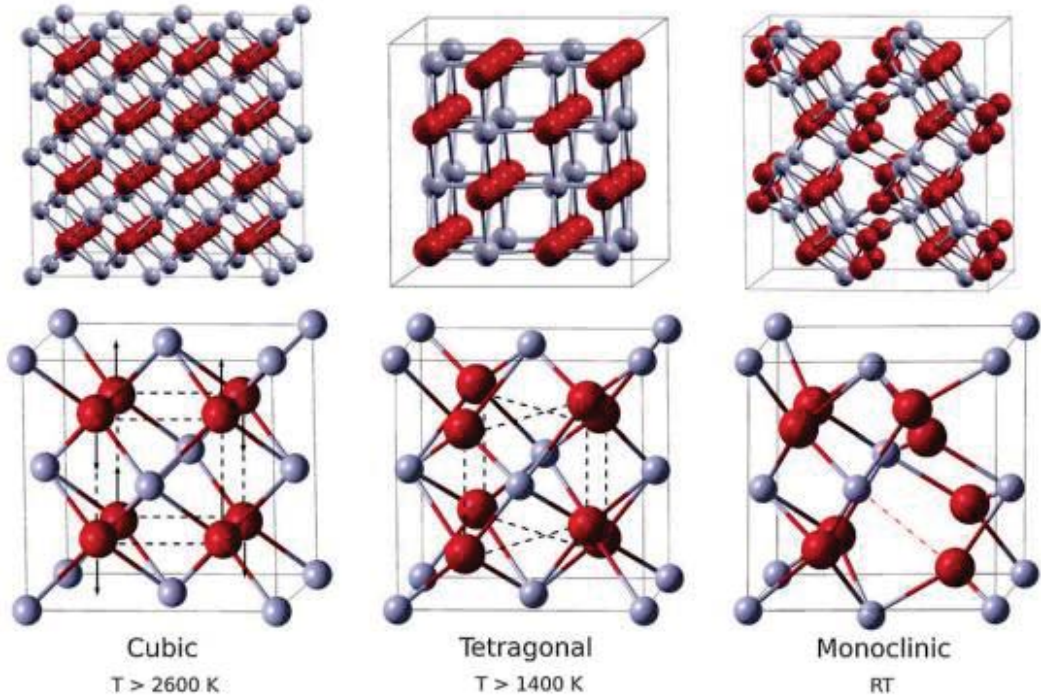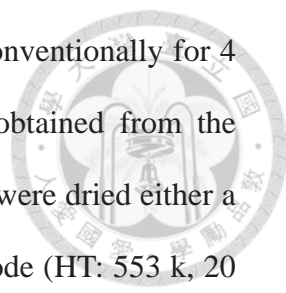
Figure 2.9 Cubic, tetragonal and monoclinic ZrO_2 lattice structures with their relative temperature range of stability. In the upper panel polymorph cells are space-expanded to provide a better view of the three different phases. In the lower panel the cubic cell is taken as reference to show the deformation of the oxygen sub-lattice for t- and m-ZrO_2 (dashed lines and arrows). Large dark red spheres and small light grey spheres represent O and Zr atoms, respectively. [21]

2.2.2 Preparation of ZrO₂ by Zirconium Alkoxide

In a sol-gel processing a mixture of metal alkoxides is combined with a mixture of alcohol and water to form a sol or a gel. The metal alkoxides are partially or completely, hydrolysed and condensed after mixing. The amount of water in the mixture must be precisely controlled to form a sol with a proper viscosity or a gel. However, the pore structure and mechanical strength can easily be affected by very tiny difference of hydrolysis and condensation behavior. In order to solve these problems, different methods are developed to control the sol-gel process.

For example, Yi has used zirconium propoxide as precursor and added some acetic acid to form zirconium propoxide acetate [23]. The results showed that the acetate can efficiently slowed down the hydrolysis rate by forming a chelate which indicates that acetic acid can substitute for one or two propoxy groups of a zirconium propoxide molecule. The reactivity toward chelating for different propoxide also depends on its electropositivity of metal ion. The chelating agent like acetic acid has been broadly utilized to control structure strength, especially for thin film formation which often deals with fracture problem or needs to finely control its pore distribution monotonically. Thus, the typical idea worthy of bearing in mind is that "acetic acid control hydrolysis rate while nitric acid can adjust condensation rate (by tuning pH value).

In addition to forming a thin film, a highly porous structure of metal oxide is required for many applications, for instance, metal oxide as catalyst. J. Mrowiec-Bialon used a supercritical CO_2 drying method to make Zirconium aerogel which can guarantee more surface area and pore volume [24]. The concerned results are presented in Table 2.5 and Fig. 2.10, A1 sample indicate that the alcogel was immersed for 4 days in amylacetate, a low surface tension solvent to replace the

solvent in the pore prior to drying process. A2 sample was aged conventionally for 4 days. A3 alcogel was aged for 15 hr, similarly as the sample obtained from the synthesis moderated by HNO_3 (label N1). The supercritical drying were dried either a "cold" (CO_2: 343 K, 15 MPa, 5 hr, sample A1 and A2) or a hot mode (HT: 553 k, 20 MPa, 5 hr, sample A3) of the process. All aerogel powders were calcined in static air for 2 hr at 773K (label A1C, A2C and A3C). The result shows that A1 sample can remains lot of tiny pores which should come from the replacement of low-tension solvent. However, the structure and high surface area is rather unfavorable in thermodynamic performance during high temperature treatment; thus A1C sample gives less pore volume which reflects the severe sintering of tiny pore. The A3C sample "remains" most pore volume (0.42 from 0.71) which has proved that controlling temperature during drying indeed tune the drying mechanism and furthermore control the pore formation. Besides, from the difference between A2 and A3 sample, the fact that ageing effect exist can be proved. The uniform pore distribution was presented in Fig. 2.10 [24].

Another research by C. Stocker for ZrO_2 aerogel discussed the effect of acid-to-alkoxide ratio, different alcoholic solvent [25]. The specific surface areas of mesoporous aerogel in their research varied from 55-205 m^2/g after calacination in air at 773K. They found that the width of the pore size ditrsibution became smaller with increasing amount of acid (See Fig. 2.11). Besides, the fraction of monoclinic ZrO_2 shares increased with increasing nitric acid-to-alkoxide ratio, the use of a long-chained branched alcoholic solvent, such as t-butanol and increasing temperature. Socker also discussed the solvent effect in the other paper [26], the result showed that under the same condition, using different solvent can effectively shift the pore distribution of gel after calcinations. (See Fig. 2.12)
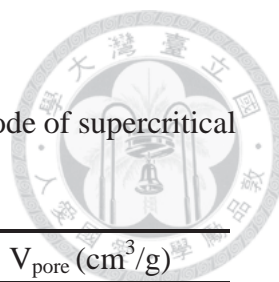
Table 2.5 Surface and pore volume of ZrO_2 powders by different mode of supercritical

drying method [24]

Sample	Mode of Drying	$S_{BET}(m^2/g)$	V_{pore} (cm^3/g)
A1	CO_2	562	1.34
A1C	CO_2	32	0.25
A2	CO_2	278	0.42
A2C	CO_2	32	0.14
A3	HT	151	0.71
A3C	HT	53	0.42
N1	CO_2	345	0.70
N1C	CO_2	60	0.27
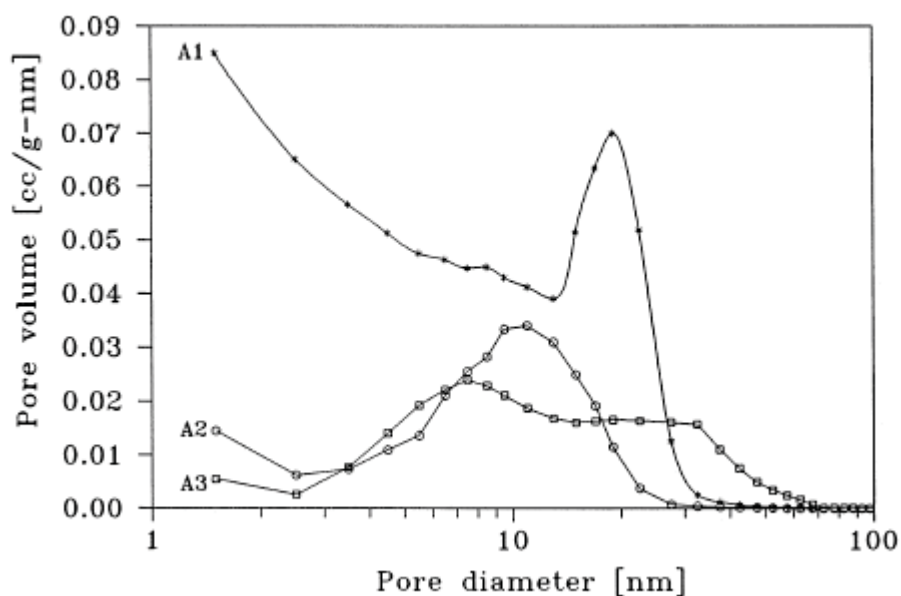
Figure 2.10 Pore distribution of ZrO_2 alcogel under different treatment. [25]
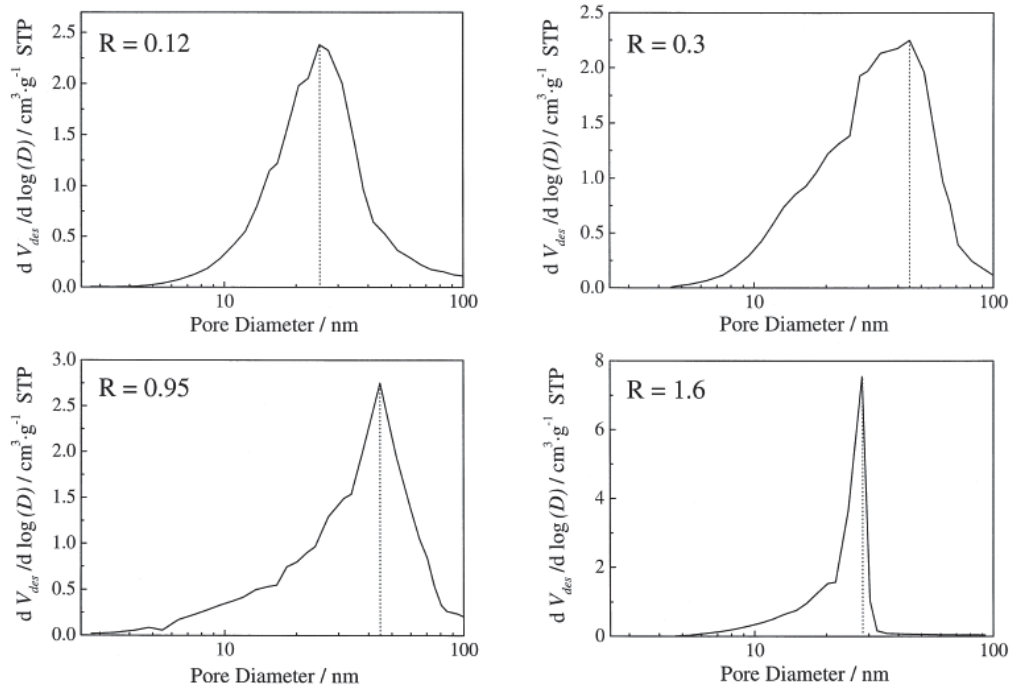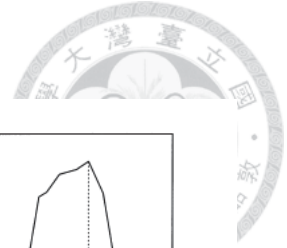
Figure 2.11 Influence of the molar acid-to-alkoxide ratio, R, on pore distribution of the high-temperature supercritical drying zirconia aerogels prepared using EtOH as solvent and calcined at 773K [25].
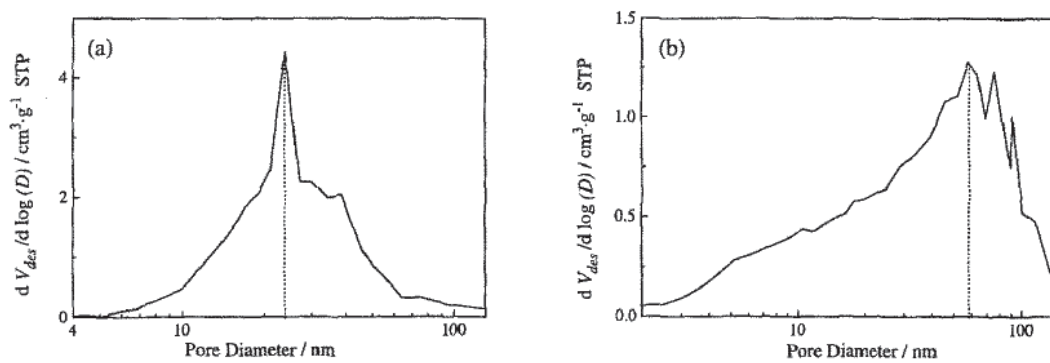
Figure 2.12 Mesopore distribution of zirconia aerogels prepared using (a) ethanol and (b) t-amylalcohol as solvents. Both samples prepared with nitri acid-to-alkoxide ratio, R = 0.08 and calcined in air at 573 K.

2.3 Basic Concepts of Rechargeable Lithium-ion Batteries

Li-ion batteries are one of the great successes of modern materials electrochemistry [27]. Their science and technology have been extensively reported in previous reviews [1,28] and dedicated books [3,29], to which the reader is referred for more details.

The expanding growth in portable electronic devices such as mobile phone, digital camera (DC), and laptop computer over the past two decades has created enormous interest in compact, light-weight batteries offering high energy densities. The growing environmental concerns around the globe are also pushing the development of advanced batteries for electric vehicles (EVs). The energy densities per unit volume (Wh/l) and per unit weight (Wh/kg) of various rechargeable batteries are shown in Fig. 2.13. Li-ion batteries are appealing for these applications because they provide higher energy density than the other rechargeable battery systems, such as lead-acid, nickel-cadmium (Ni-Cd), and nickel-metal hydride (Ni-MH) batteries. The nominal voltage of a lithium ion battery is around 3.7 V, which is much larger than that of conventional nickel batteries (1.2 V) and lead-acid batteries (2 V). The high voltage of the lithium ion battery arises as it uses the chemistry of intercalation reactions of lithium ion with the cathode and anode.

Theoretically, a Li-ion cell involves with a reversible insertion/ extraction of guest species (Li ions) into/from a host matrix (electrode materials) during the discharge/charge process. The lithium insertion/extraction process taking place with a flow of ions through the electrolyte is accompanied by a redox of reaction of the host matrix assisted with a flow of electrons through the external circuit. This concept of rechargeable lithium batteries was first illustrated with a layer structured transition metal sulfide, TiS_2, as the positive electrode (cathode), Li metal as the negative

electrode (anode) and lithium perchlorate in dioxolane as the electrolyte [30]. During discharge, the lithium ion are inserted into the van der Waals gap between the sulfide layers and the charge balance is maintained by a reduction of the Ti^{4+} ions to Ti^{3+}. During charge, exactly the reverse process involving with the extraction of lithium from the van der Waals gap and an oxidation of Ti^{3+} to Ti^{4+} occurs. During the lithium insertion/extraction (discharge/charge) process, the layer structure is maintained, resulting in good reversibility.

Such batteries consisting of lithium insertion compounds as both cathodes and anodes are also known as swing batteries or rocking chair batteries since two-way movement of Li ions between anode and cathode through the electrolyte occurs during charge/discharge processes. Increasing high voltages are associated with increasing difficulty in removing a lithium ion from a particular site during charge or discharge; the site with the lowest potential energy will be occupied first by Li ions. Take $LiCoO_2/C$ for example, which is the most common battery system presently, shown as Fig. 2.14 [28], the reactions can be described as follows:

Cathode reaction:

$$LiCoO_2 \underset{Disch\,arg\,e}{\overset{Ch\,arg\,e}{\rightleftarrows}} Li_{1-x}CoO_2 + x\,Li^+ + x\,e^- \tag{2-2}$$

Anode reaction:

$$C_6 + x\,Li^+ + x\,e^- \underset{Disch\,arg\,e}{\overset{Ch\,arg\,e}{\rightleftarrows}} Li_xC_6 \tag{2-3}$$

Net reaction:

$$LiCoO_2 + C_6 \underset{Disch\,arg\,e}{\overset{Ch\,arg\,e}{\rightleftarrows}} Li_{1-x}CoO_2 + Li_xC_6 \tag{2-4}$$
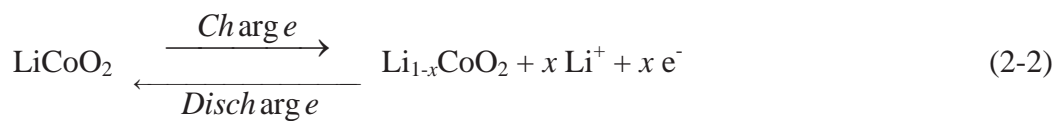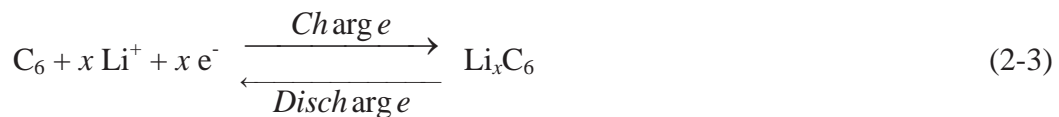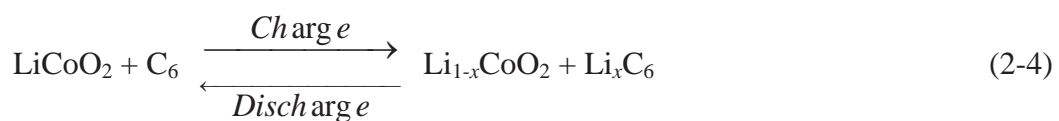
During charging under an applied voltage, de-intercalation of some of the lithium ions from the cathode ($LiCoO_2$) into electrolyte liquid occurs and simultaneously an equivalent amount of lithium ions from the electrolyte intercalate into the carbon anodes. During discharge, the reverse reaction proceeds spontaneously. On both charge and discharge, charge compensation occurs through the external circuit.

From a materials design point of view, the anode insertion compound Li_xM_y should also satisfy several important criteria like the cathode insertion host: a large degree x of lithium insertion/extraction (high capacity), high electronic and ionic conductivity, good chemical and structural stabilities (reversibility), and affordable cost.
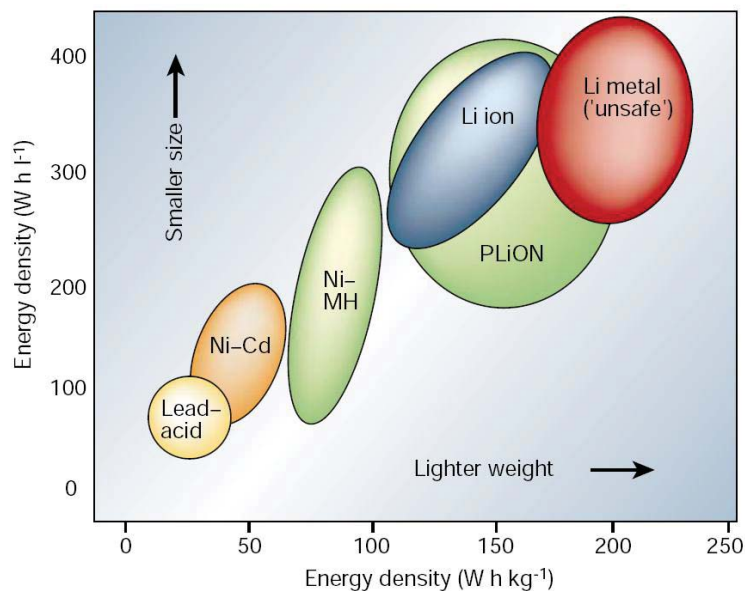
Figure 2.13 Comparison of the different battery technologies in terms of volumetric and gravimetric energy density [1].
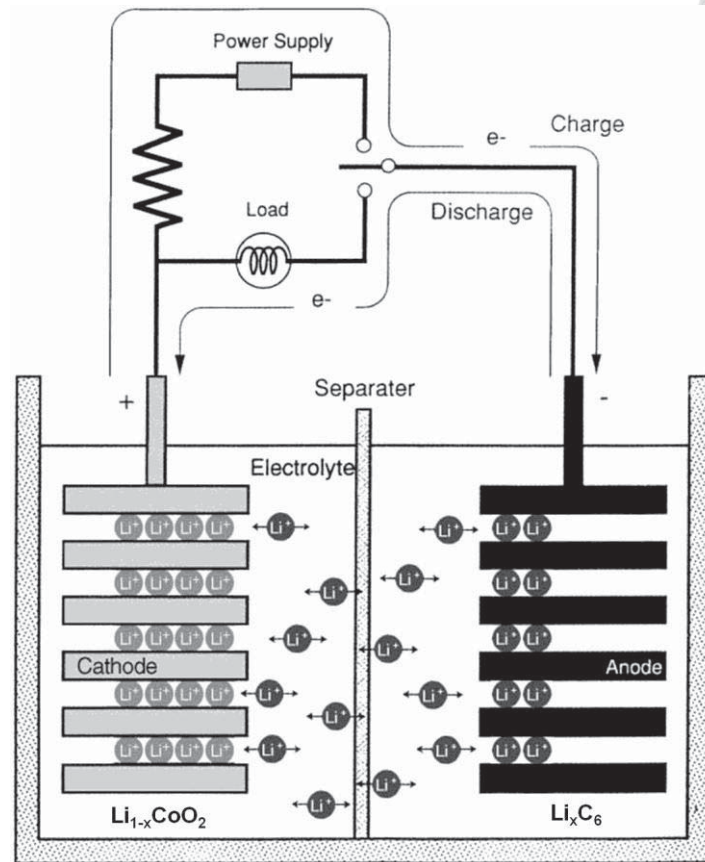
Figure 2.14 Schematic illustration of the charge/discharge process in a lithium-ion cell consisting of lithium insertion compounds as both anode and cathode [28].

2.4 Silicon as an Anode Materials of Lithium-ion Batteries

2.4.1 Pure Si as an Anode for Lithium-ion Batteries

Experimental work on anodes using chemical elements which form alloys with lithium was started in early 1960s. In 1971, Dey [31] found that lithium can be electrochemically alloyed with a number of metals at room temperature, including Sn, Pb, Al, Au, Pt, Zn, Cd, Ag, and Mg. However, the alloying process resulted in complete disintegration of the electrodes and loss of electronic contact. Similarly, Sharma and Seefurth [32] reported the formation of Li–Si alloys in high temperature cells operating in the 400–500 ^{o}C range. It was reported that the alloying process in silicon anodes results in formation of $Li_{12}Si_7$, $Li_{14}Si_6$, $Li_{13}Si_4$, and $Li_{22}Si_5$ alloys [60]. Study of the Li–Si binary system [6,32-34] indicated that each silicon atom can accommodate 4.4 lithium atoms leading to formation of $Li_{22}Si_5$ alloy, i.e., a specific insertion capacity of 4200 mAh/g, the highest among the above alloying elements Figure 2.15 shows the equilibrium open-circuit voltage in the Li-Si system as a function of composition, as determined by use of the coulometric titration technique [6]. In addition to its outstanding capacity, silicon is the second most abundant element on earth. Because of these attributes, a great deal of attention has been given to using silicon as Li-ion cell anode material. However, the alloying process of Li with Si was found to be less reversible at room temperature [35-37].

The Li-Si reaction at room temperature does not appear to follow Fig. 2.16. In fact, Li insertion/extraction in silicon at room temperature has been reported to deviate far from the equilibrium prediction, and the cycling voltage curves are influenced by both the Si particle size and the depth of lithiation. Fig. 2.16 shows the typical voltage curves observed for Si anodes with the particle sizes of few microns

[38]. The first-cycle alloying curves exhibit a single flat plateau at ~0.1 V, indicating a single two-phase addition reaction instead of the multi-phase reactions predicted by the equilibrium Li-Si phase diagram (Fig. 2.16). Moreover, the subsequent alloying curves are slopping-shaped not flat potential plateau. Meanwhile, the de-alloying voltage curves show a strong dependence on the cut-off potential of alloying. If the anode is fully alloyed to 0V, the de-alloying curves exhibit a single plateau at ~0.4V in all the cycles, followed by an upwardly sloping region (Fig. 2.16-(a)). However, if the anode is alloyed to above 50 mV, the de-alloying curves shows two inclined plateaus instead (Fig. 2.16-(b)). The voltage profiles of Si anodes are also affected by the Si particle size. For Si particles of 50–200 nm, their de-alloying curves are round-shaped with no distinct plateau, even after the anodes are fully alloyed to 0 V [39-40]. Fig. 2.17 shows an example where the micron-sized Si sample (S_MCp) has a flat de-alloying plateau at ~0.4 V but the nano-sized sample (S_NCp) (10–100 nm) shows a sloping de-alloying curve even after fully alloyed to 0 V [39].

Several authors have reported that crystalline silicon becomes an amorphous Li-Si alloy when Si reacts electrochemically with Li [41-43]. Limthongkul et al. proposed an electrochemically driven solid-state amorphization mechanism [42]. The electro- chemical lithiation mechanism at room temperature was reported in detail by *ex situ* and *in situ* X-ray diffraction (XRD) analyses [38,44-46]. The reaction mechanism was explained as follows [47]:

During Li$^+$ insertion:

$$\text{Si (crystalline)} + x\text{Li}^+ + x\text{e}^- \rightarrow \text{Li}_x\text{Si (amorphous)} \tag{2-4}$$

$$+ (3.75 - x)\,\text{Li}^+ + (3.75 - x)\,\text{e}^- \rightarrow \text{Li}_{15}\text{Si}_4 \text{ (crystalline)} \tag{2-5}$$

During Li$^+$ extreaction:
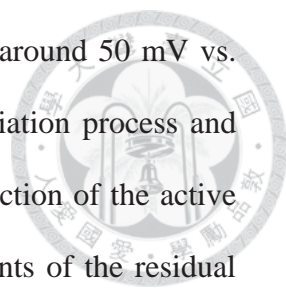
$$\text{Li}_{15}\text{Si}_4 \text{ (crystalline)} \rightarrow \text{Si (amorphous)} + y\text{Li}^+ + y\text{e}^- + \text{Li}_{15}\text{Si}_4 \text{ (residual)} \tag{2-6}$$
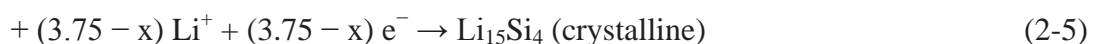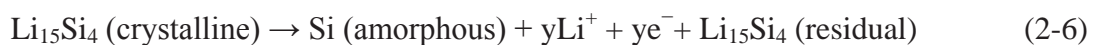
In the two-phase region, crystalline Si becomes an amorphous Li–Si alloy (2-4)

33

and the amorphous phase suddenly crystallizes as a $Li_{15}Si_4$ phase around 50 mV vs. Li/Li^+ (2-5). There is another two-phase region during the de-lithiation process and the final product is amorphous Si (2-6). Due to electrical disconnection of the active material caused by a severe volume change, there are some amounts of the residual $Li_{15}Si_4$ phase after the first de-lithiation, which results in a large irreversible capacity. When Li ions are inserted into the amorphous Si during the second cycle, two sloping voltage plateaus are observed, which indicates single phase regions. After the second cycle, reactions (2-5) and (2-6) shown above are repeated and the reversible capacity fades.

Table 2.4 summaries the data for crystal structure, density, specific capacity and corresponding degree of volumetric expansion of Li-Si phases [6,38].
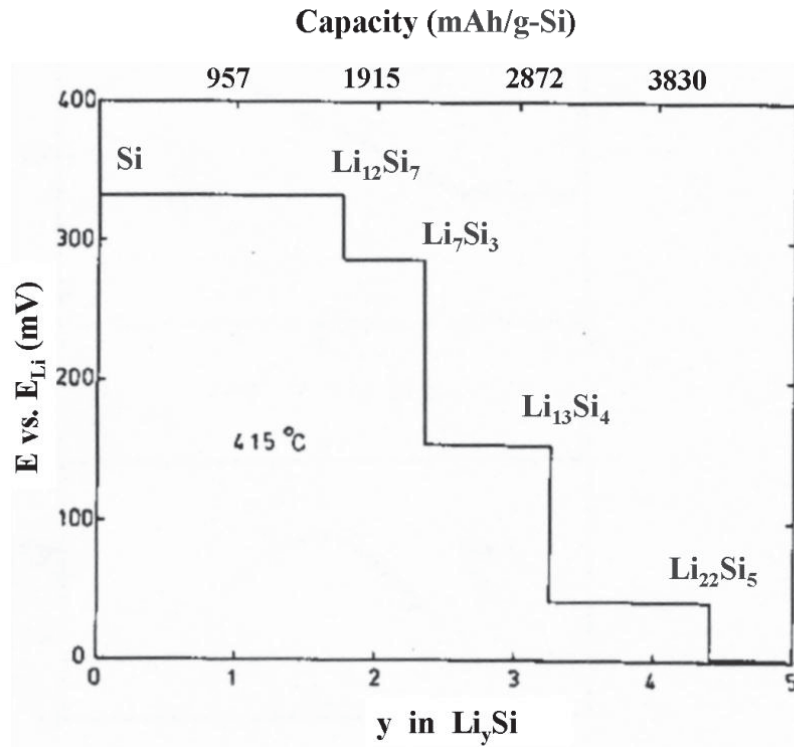
Figure 2.15 Coulometric titration curve for the Li-Si system at 415°C [6].
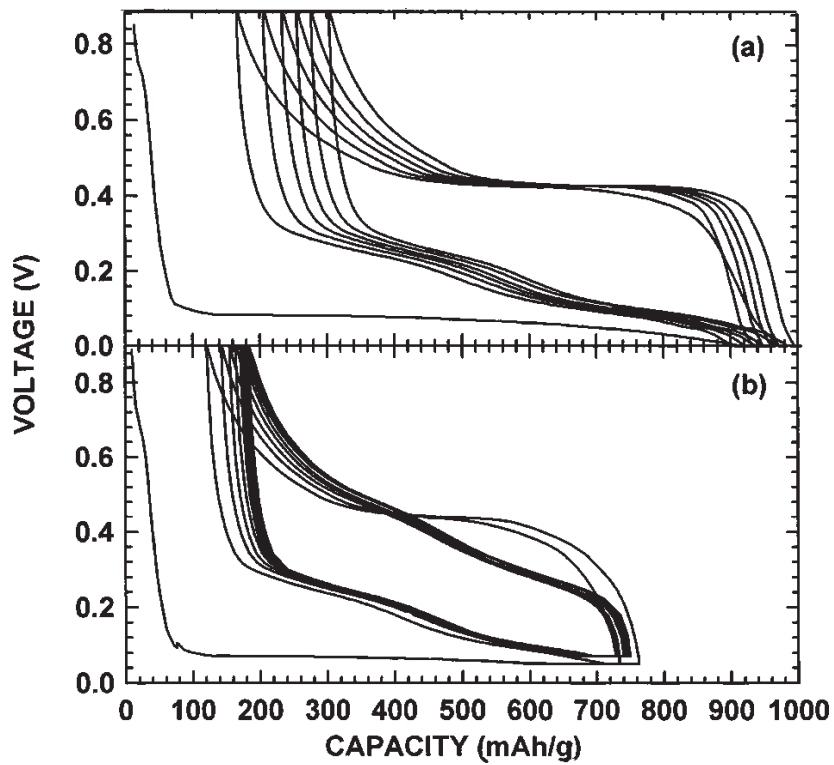
Figure 2.16 (a) Voltage curve of $Ni_{30}Si_{70}$ discharged to 0 V and (b) The voltage curve of $Ni_{30}Si_{70}$ discharged to 50 mV for the first two cycles, then to 70 mV [38].
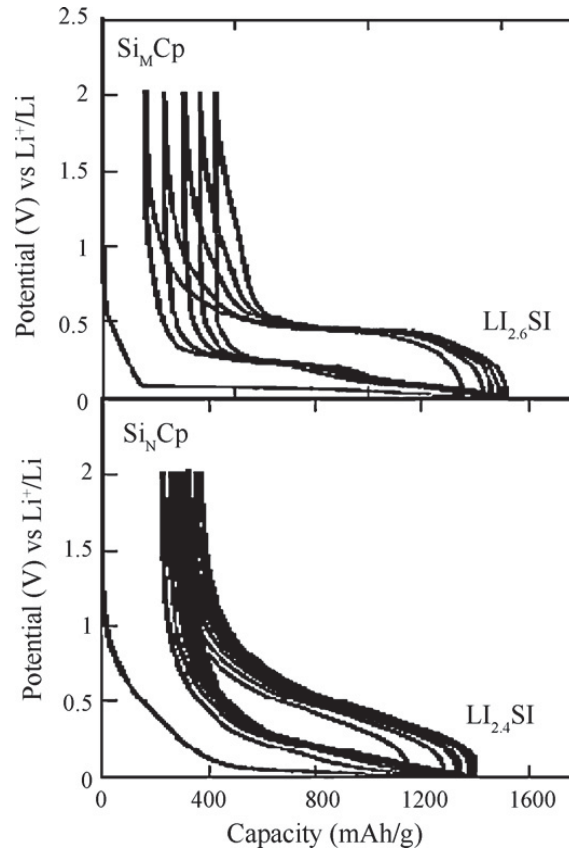
Figure 2.17 Voltage–capacity curves for microsized (Si$_M$: 1-10 μm) and nanosized (Si$_N$: 10-100 nm) Si anodes [39].

Table 2.6 Crystal structure, density, capacity and corresponding volume variation for the Li-Si system [6]
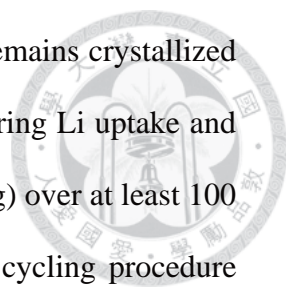
Compound and crystal structure	Density (g/cm^3)	x (Li$_x$Si)	Capacity (mAh/g-Si)	V$_f$/V$_i$× 100%
Si, cubic	2.33	0	0	100
Li$_{12}$Si$_7$, orthorhombic	1.53	1.71	1632	218
Li$_7$Si$_3$, rhombohedral	1.43	2.33	2223	258
Li$_{13}$Si$_4$, orthorhombic	1.25	3.25	3101	337
Li$_{22}$Si$_5$, cubic	1.18	4.4	4198	413
Li$_{15}$Si$_4$, cubic [38]	1.18	3.75	3579	380

2.4.2 Approaches for Improving the Performance of Si Anodes

To understand the reasons for the poor cycling stability of Si negative electrodes, the failure mechanism was investigated [46]. During the Li extraction process, the de-alloying reaction is not completed due to the increased internal resistance that is caused by some loss of the contact area between Si and the electrode architecture. This is caused by volume contraction of the Si particles after expansion in the previous Li-Si alloying process.

One way to improve electronic contact between particles during insertion and extraction is by mixing conductive additives (CA) such as graphite flakes and/or nano-scale carbon black into micro-Si anodes [48]. Increasing CA content dramatically increased the cycle life and irreversible capacity of silicon anodes due to the increased interparticle electronic contact, which gave improved Li de-alloying kinetics and also prevented the agglomeration of Si particles. The buffering action of soft CA particles also suppressed the large Si volume change on some degree, relieving mechanical stresses inside the anode. By using the same idea of electrode processing, dispersing Si particles in a graphite [49,50] or carbon black/binder matrix [51] presents very good electrochemical properties. These promising results can also be seen as originating from either the very good electrical wiring provided by the huge carbon content or the ''space filling'' matrix effect played by carbon [52]. Naturally, the idea of "buffering matrix" can not only apply for electrode processing but also for material design (Fig. 2.18) [53].

A second way to improve Si anode performance is to decrease Li insertion/ extraction levels by narrowing the cycling voltage window [48,54]. Obrovac and Krause [54] demonstrated that a limitation (Constant Current–Constant Voltage, CCCV) in discharge voltage (0.17 V vs. Li/Li$^+$) of a bulk Si$_{crystallized}$/Li cell can be

efficient in limiting the amount of reacted Si. The non-reacted Si remains crystallized while the reacted part turns amorphous and remains amorphous during Li uptake and removal. Excellent cycling efficiency is then observed (~950 mAh/g) over at least 100 cycles, provided that the right binder is used, a pre-conditioning cycling procedure and a voltage limitation applied (Fig. 2.19). This approach can be seen as the in situ creation of a non-reacted substrate (inner crystallized Si) that limits the loss of integrity of the active part (surface reacting layer/film of Si). From a fundamental point of view, this strategy and this CCCV cycling limitation in voltage is elegant, but will be difficult to implement for real applications. Even if the role of the binder is not clearly established in this case, it still shows that very large crystallized Si particles can be nicely cycled [53].

A third and most widely studied method is to reduce the Si particle size [48], especially to nano-scale [55-56]. Initiated by Yang et al. [57-58], the use of small domains has been deeply explored. It turned out that ductile elements such as Sn can be cycled as small reacting dots, provided that a matrix prevents its agglomeration [59,60]. Otherwise, this would result in particle growth leading back to the inability to sustain the stress induced by alloying without loss of point contact. Such an aspect, together with the need for limiting the side reactions with electrolytes at the surface of such small particles (high specific surface of contact), has triggered research on composite materials.

In an attempt to reduce the cyclic capacity fade and the first cycle irreversible capacity of Si anodes, several strategies have been developed to reduce the detrimental effects of large volume changes and to alleviate the side reaction with electrolyte. These approaches can be classified into five categories:

1. Si/M composites (M : active/inactive metal or compound)

2. Si/C composites

3. Porous Si anode materials

4. Nanostructured Si anode materials

5. Si anodes with different binders

This research is to develop a ZrO_2/nano-Si/C composite which should certainly belong to category 1. The concerned research would introduced in next chapter.
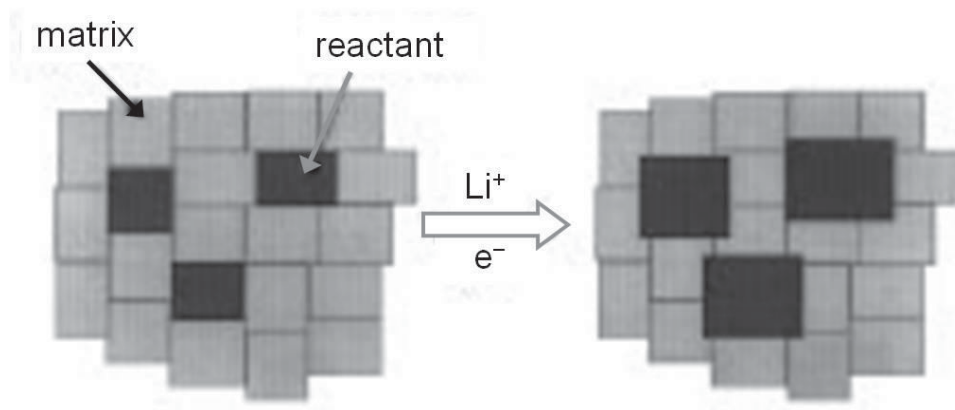
Figure 2.18 Model: strong expansions of the 'reactant' domains due to lithiation can be buffered by the inactive or less active 'matrix' domains, thus keeping the extent of crack formation in the overall multiphase material small [53].
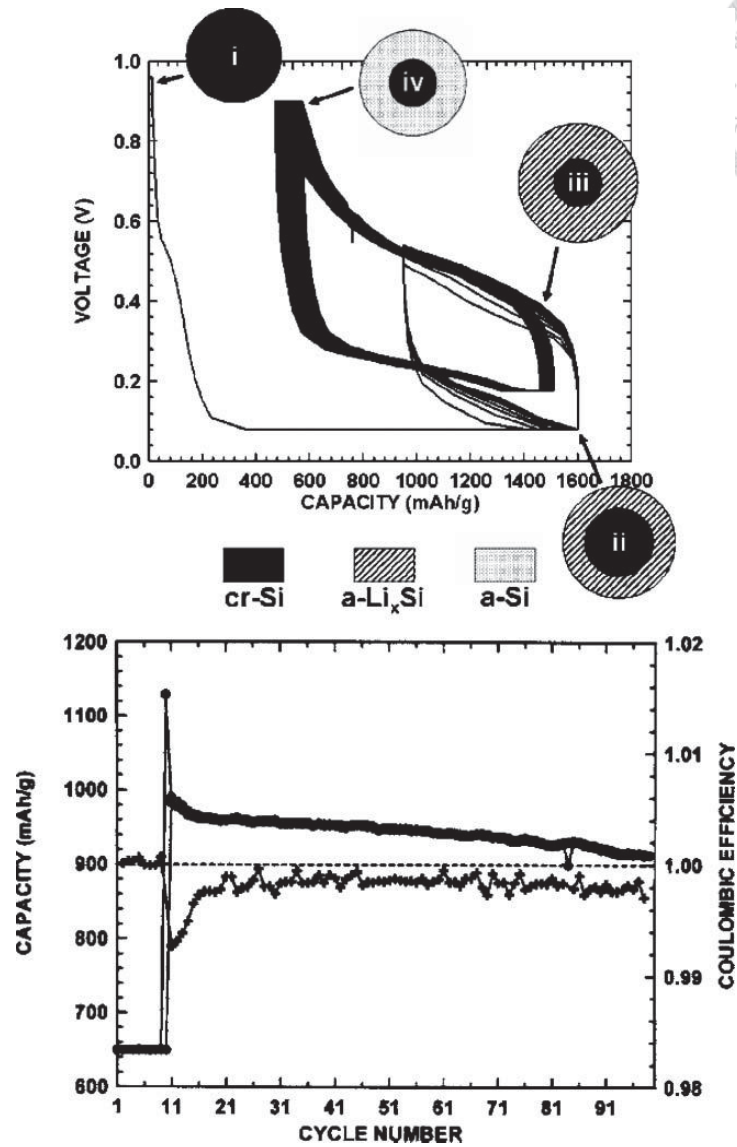
Figure 2.19 Voltage vs. composition plot for a Si/Li cell undergoing preconditioning cycles and CCCV cycling and corresponding capacity (circles)/coulombic efficiency (cross) as a function of the cycle number [54].
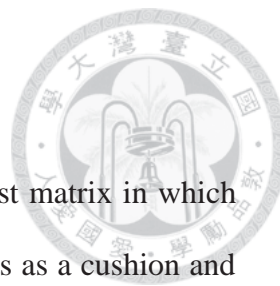
2.4.3 Si-ZrO$_2$ Composites

Si-inactive matrix composite anode consists of an inactive host matrix in which silicon is finely dispersed. An inactive matrix used in the anode acts as a cushion and accommodates the volume change in the Si active material, thereby preventing pulverization of the anode. This inactive matrix must have a high mechanical strength to withstand the volume change of Si on cycling. Ideally, it should also have high electronic conductivity to allow charge transfer reactions to take place [61].

ZrO$_2$ has several properties which could be beneficial for making ZrO$_2$-Si composite as anode material. First, it's electrochemically inactive for lithium ion batteries and has strong mechanical property which can well buffer the expansion of Si [22,62]. Second, it has rather high intrinsic density (ZrO$_2$-m: 5.68 g/cm^3) which can elevate the density of anode material and hence raise the volumetric capacity of electrode. Third, there has been several well-developed sol-gel methods about producing highly porous ZrO$_2$ matrix which has been mentioned in chapter 2.2.2. Thus, using porous ZrO$_2$ as a buffering agent seems to be practicable method to solve the expansion problem of Si during cycling. However, there were still few researches in developing Si-ZrO$_2$ as anode material due to its electric insulation.

Wu et. al. has developed a promising method of coating anode materials with a thin layer of ZrO$_2$ which can strongly improve mechanical strength and thus alleviate their expansion [62]. The process is simple and fast with typical sol-gel method. In addition to layer coating, Tu et. al. adopted another method that taking porous ZrO$_2$ as a buffering matrix rather than a coating layer [63,64]. See Fig. 2.20. Their research indicated that the pore structure can effectively alleviate Si expansion. Furthermore, their latter research also indicate that tuning the ratio of ZrO$_2$/Si component and the average pore diameter can effectively prevent anode from fast pulverization (Fig. 2.21

and Fig. 2.22 [63]). However, there were several issues and problems which were not clearly clarified or solved in the research. First, they used spinning coating method to have ZrO_2/Si gel deposited on Cu foil which could derive very thin film layer. Therefore, the improved capacity retention might partly lead by prevention from aggregation and enhanced mechanical stress with thin-film structure. Second, the adopted current density, 40 mA/g (around 0.02 C for capacity 2000 mAh/g) might be too low for practical application. Third, the porous net-work resulted from using a large amount of different surfactant as structure-directing-agent (i.e. $W_{S.D.A.}$: W_{Si} ~ 10 : 1), which would burn off in calcinations process and it could somehow be an economic issue.

Except for the unclarified issues, the research indeed provides a good knowledge basis for producing ZrO_2/Si matrix. In contrast, our research focuses on producing porous ZrO_2/Si/C composite powders by tuning the typical sol-gel factors instead of adding other additives. The specific experimental procedure and result discussion would be introduced in the following chapters.
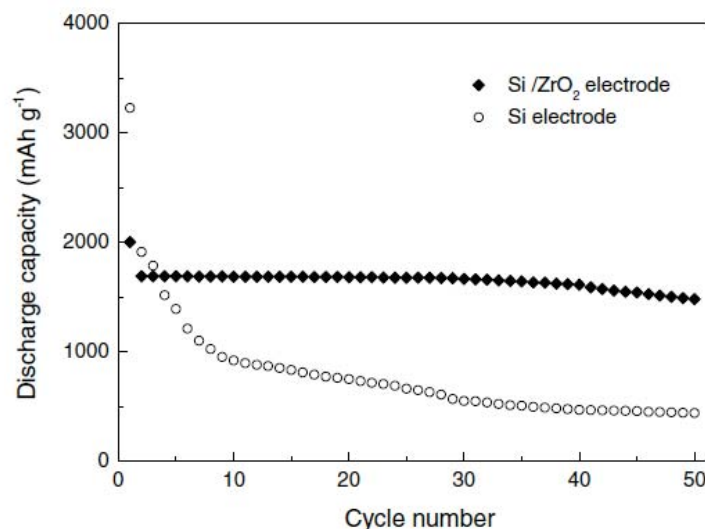
Figure 2.20 Discharge capacity versus cycle number for the mesoporous Si/ZrO_2 nanocomposite and Si nanoparticles. The current density is 40 mA/g which equals to 0.02C for Si/ZrO_2 electrode [64].
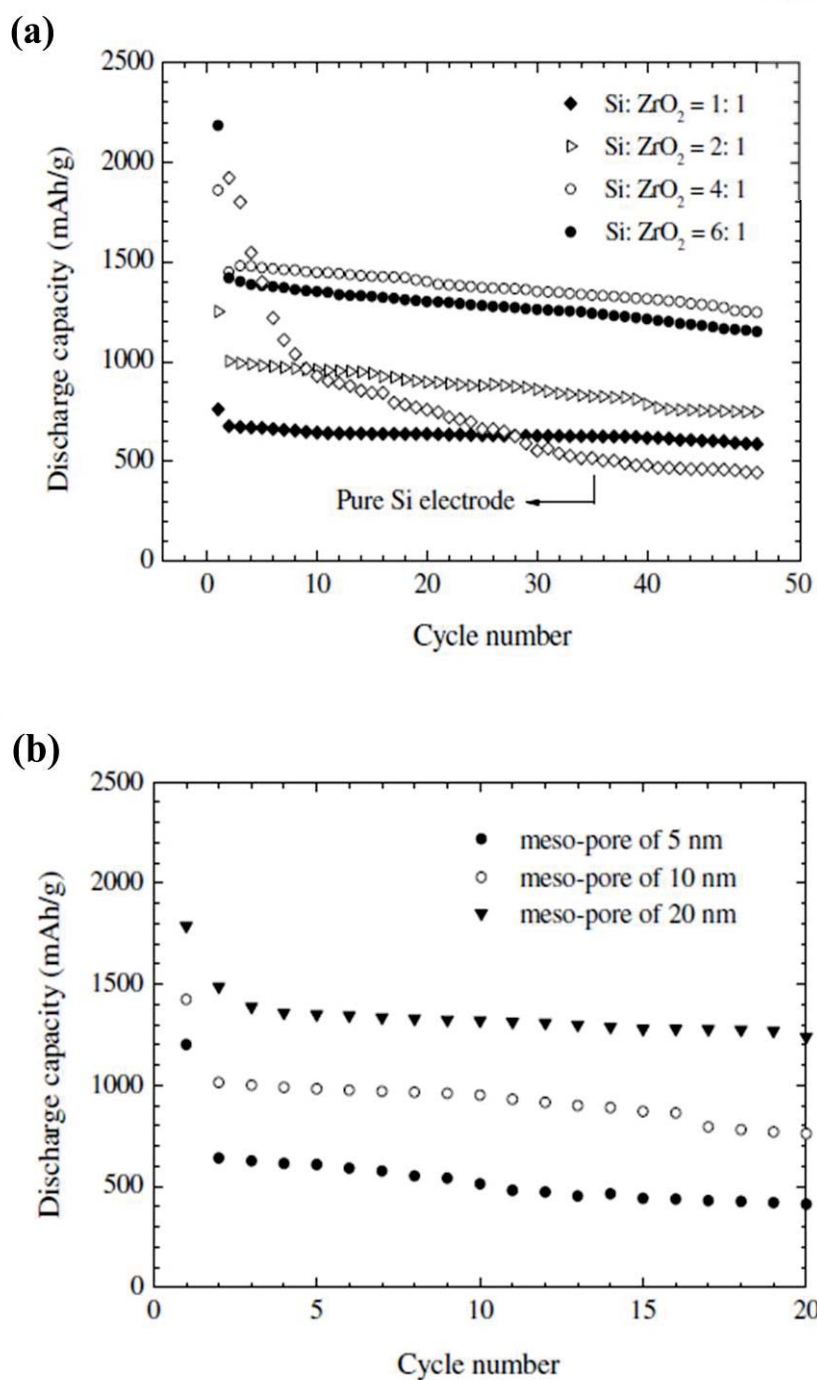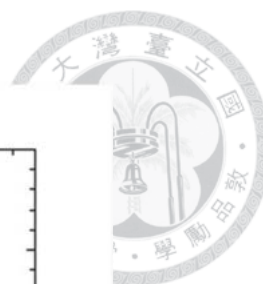
Figure 2.21 (a) Cycling performances of Si/ZrO$_2$ mesoporous composite film electrodes with Si/ZrO$_2$ mole ratios of 1:1, 2:1, 4:1, and 6:1 (b) Cyclability of Si/ZrO$_2$ mesoporous composite film electrodes with different mesopore sizes (mole ratio = 4:1). The current density is 40 mA/g [64].
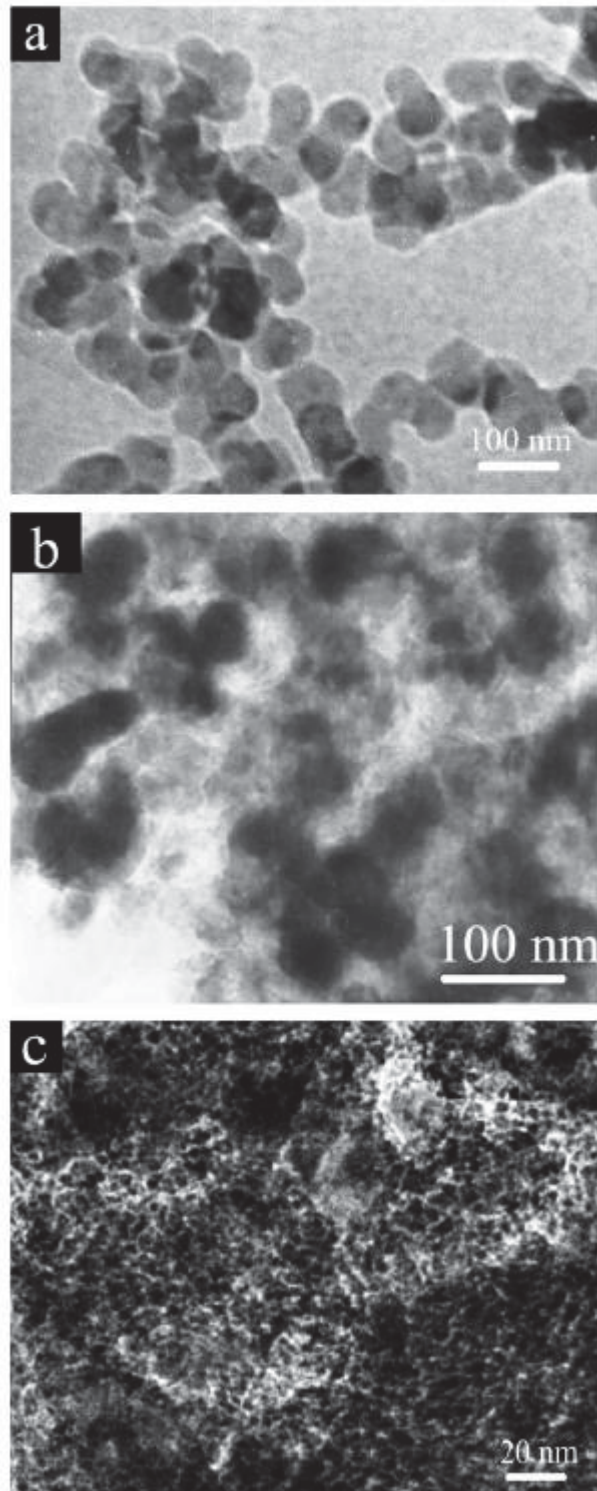
Figure 2.22 TEM image of (a) Si nanoparticle (b) Si nanoparticles surrounded by

ZrO$_2$ (c) Mesoporous ZrO$_2$ film [63].
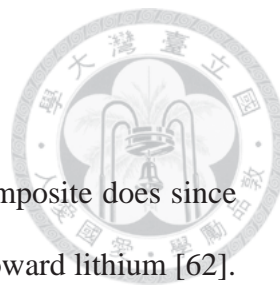
2.4.4 Si-C composites

$ZrO_2/Si/C$ composite presents similar performance as Si/C composite does since it has been already known that ZrO_2 is electrochemically inactive toward lithium [62]. Thus, several previous studies about electrochemical performance of Si/C composite are of the same importance in this research.

For example, Lee et. al used a process involving pyrolysis reaction and combined it with an intervening HEBM (i.e. high energy ball milling) step [65]. With different ball-milling time (i.e. different energy applying on the composite), the composites showed different morphology which might indicate different structural strength. Fig. 2.23 gave cycle life plot with different ball milling time.

On the other hand, another research discussed a novel method to deposit carbon on Si particles by using carbon gel which was prepared from resorcinol (R) and formaldehyde (F) [66,67]. The preparation was by mixing measured amounts of resorcinol and formaldehyde and heating to 85 ^{o}C [66]. When the resulting mixture became viscous, nanocrystalline Si was added. This was heated at 85 ^{o}C for 10 h to form a carbon aerogel, which was sintered at 650 ^{o}C to form Si/C composites. During initial heating at 85 ^{o}C, resorcinol reacted with formaldehyde to form hydroxymethyl resorcinol derivatives, which further reacted with formaldehyde to form a cross-linked three-dimensional network called RF gel (Fig. 2.24). After calcination at 650 ^{o}C, an amorphous carbon structure formed. The XRD results of Si/C composites prepared by this process showed peaks related to Si and amorphous carbon, and TEM images showed that Si was uniformly dispersed in the latter. When cycled between 0.02 and 2.0V, these anodes showed a reversible capacity of 1450 mAh/g and an irreversible capacity of 550 mAh/g. During further cycling, they showed high cycling stability with a reversible capacity of 1400 mAh/g after 50 cycles. Their excellent cycling

performance was due to the nanosized Si and its dispersion in a three-dimensional carbon network.

One way to overcome the problem of large volume expansion is to design three-dimensional porous electrode structures with sufficient porosity to accommodate the volume expansion. High reversible capacities have been reported for hierarchical porous nano-composites synthesized using pyrolysis. A reversible capacity at 1C of 1530 mAh/g after 100 cycles with a per cycle capacity loss just over 0.5% was achieved using a hierarchical silicon/carbon composite synthesized by silicon and subsequent carbon deposition onto an annealed carbon black scaffold to obtain a carbon black/silicon/amorphous carbon structure (Fig. 2.25) [68]. Even after 100 cycles, the capacity was quite stable and the coulombic efficiency was near 100%. This rather impressive performance may be the result of the interesting hierarchical and porous nature of the silicon/carbon composite. The annealed carbon black scaffold, which has only limited electroactivity (100mAh/g), is not expected to fracture due to expansion during lithiation, and the continuous electron current path provided by the scaffold may also reduce ohmic polarization. The second carbon coating process likely serves to protect the electroactive silicon from side reactions by facilitating the formation of a stable SEI layer.
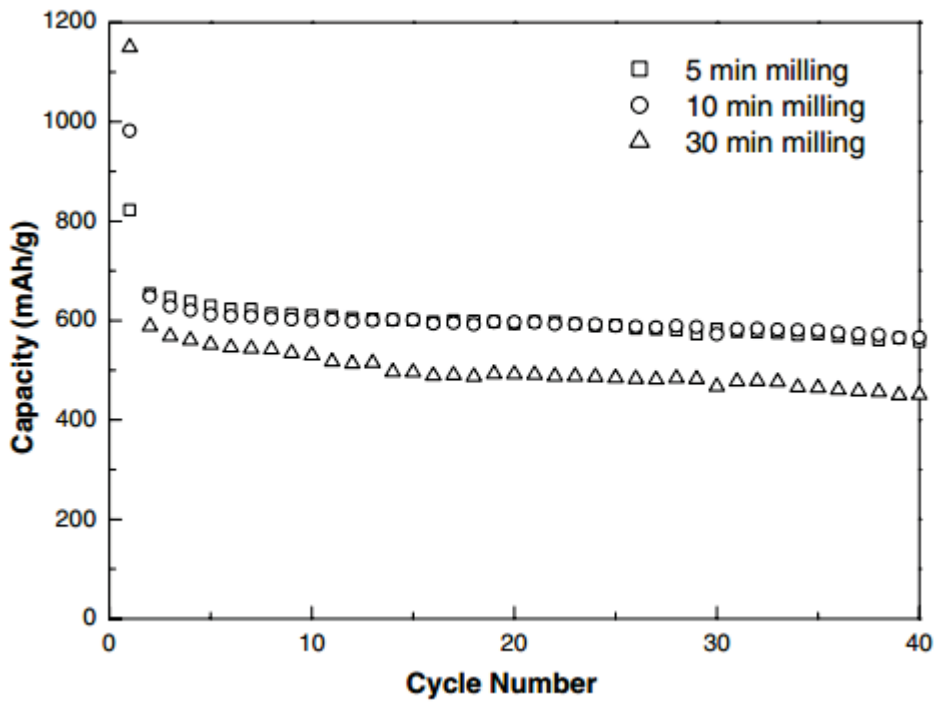
Figure 2.23 Discharge capacity vs. cycle number of nano-Si dispersed Si oxide/graphite composites with milling time [65].
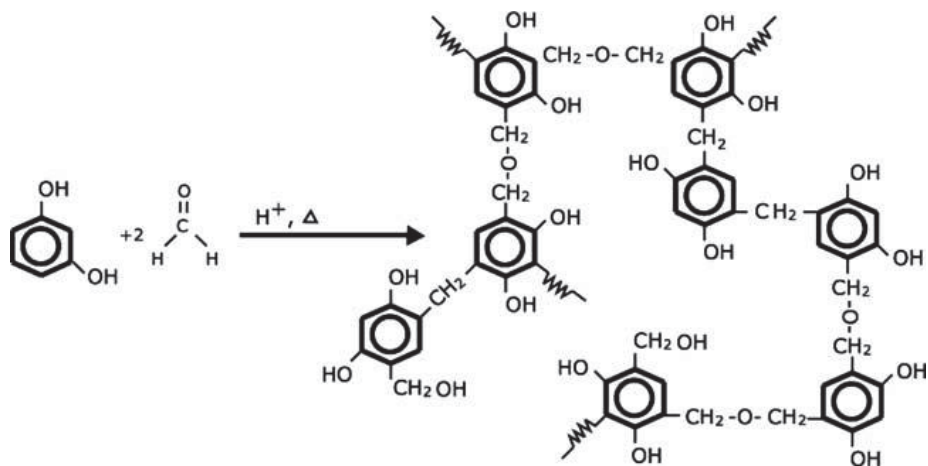
Figure 2.24 A schematic diagram of the R–F gel reaction [66].
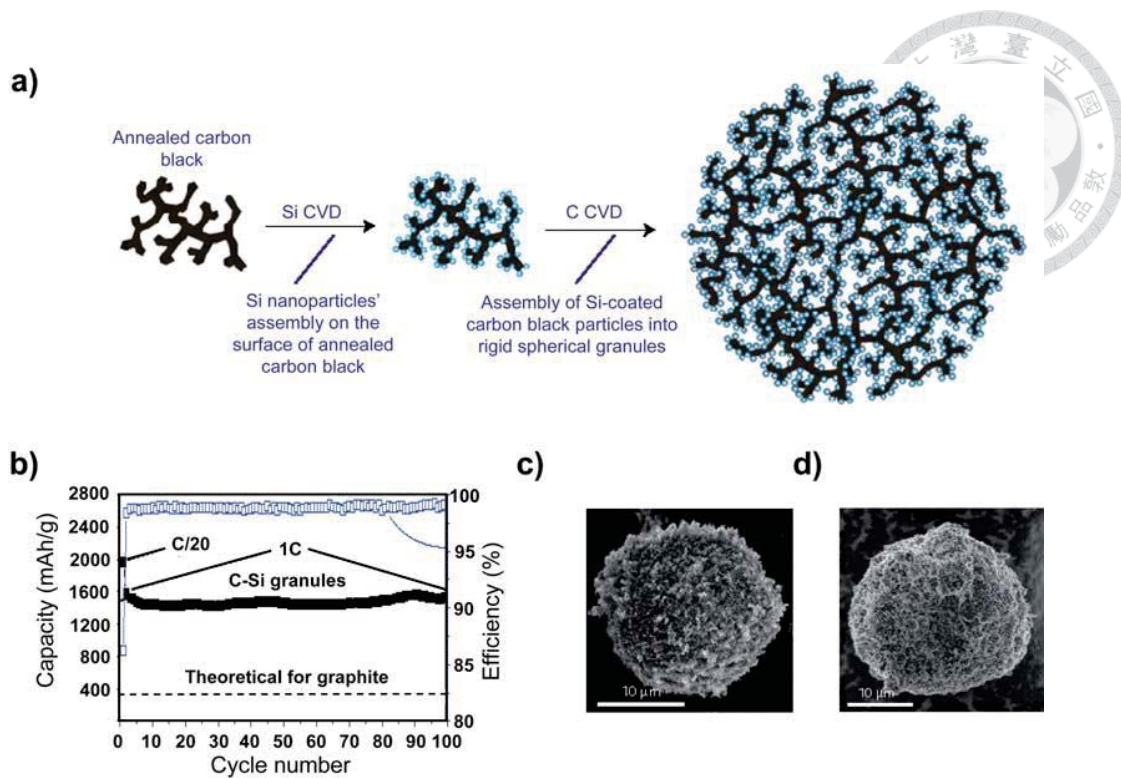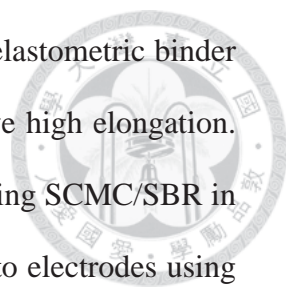
Figure 2.25 (a) Schematic drawing of a hierarchical composite comprised of silicon particles deposited onto an annealed carbon black framework. (b) The specific capacity of the hierarchical silicon/carbon composite. SEM micrograph of a Si/C nanocomposite granule before (c) and after (d) electrochemical cycling [68].

2.4.5 Si with different binders

Poly vinylidene difluoride (PVdF) has been the most frequently used binder in bulk powder electrodes, especially for recent industrial battery manufacturing. However, this thermoplastic binder cannot sustain the elongation that occurs during volumetric expansion, leading to rapid capacity fading. Electrode polarization has been found to increase during cycling when using PVdF, suggesting degrading electrical contact after repeated electrode expansion/contraction [69].

Sodium carboxy-methyl cellulose (SCMC) is a water soluble elastometric binder that can be blended with styrene butadiene rubber (SBR) to achieve high elongation. Wu et al. [69] has shown that Si and carbon-coated Si electrodes using SCMC/SBR in 1:1 weight ratio demonstrated enhance cycling stability compared to electrodes using PVdF. Ding has illustrated the possible esterification between hydroxyl groups on Si surface and carboxyl groups in SCMC which strengthens the connection between Si and the binder (Fig. 2.26 [70]).

Recently, I. Kovalenko proposed a promising binder, alginate as binder and effectively improved cycling fading of nano Si in [71]. To most people's surprises, alginate is cheap as SCMC and commonly used as an additive in food processing. It's hard to imagine the huge improvement for Si-based electrodes. Kovalenko has proposed that the high stability might attribute to its rather stable SEI formation of Si-based electrodes during cycling (Fig. 2.27). Besides, the mechanical strength is strong enough to sustain the volume expansion of Si-based electrode during cycling. As presented in Fig. 2.28, an atomic force microscopy indentation study was conducted to compare the mechanical strength of films made of different binders. In a dry state, films made of alginate or SCMC exhibited around 7 times higher stiffness than that of PVdF. Interestingly, when immersed into the electrolyte solvent, the stiffness of alginate or SCMC did not change appreciably whereas the PVdF films became nearly 50 times softer. Ellipsometry studies showed no detectable swelling of thin (~70nm) alginate films in the electrolyte solvent vapors. In contrast, PVdF films of similar thickness attract substantial amounts of carbonates from the vapor, demonstrating changes in thicknesses of ~20%. The negligibly small swellability of the alginate indicates a low level of polymer/electrolyte interaction. This property may prevent undesirable access of the electrolyte liquid to the binder/Si interface [71].
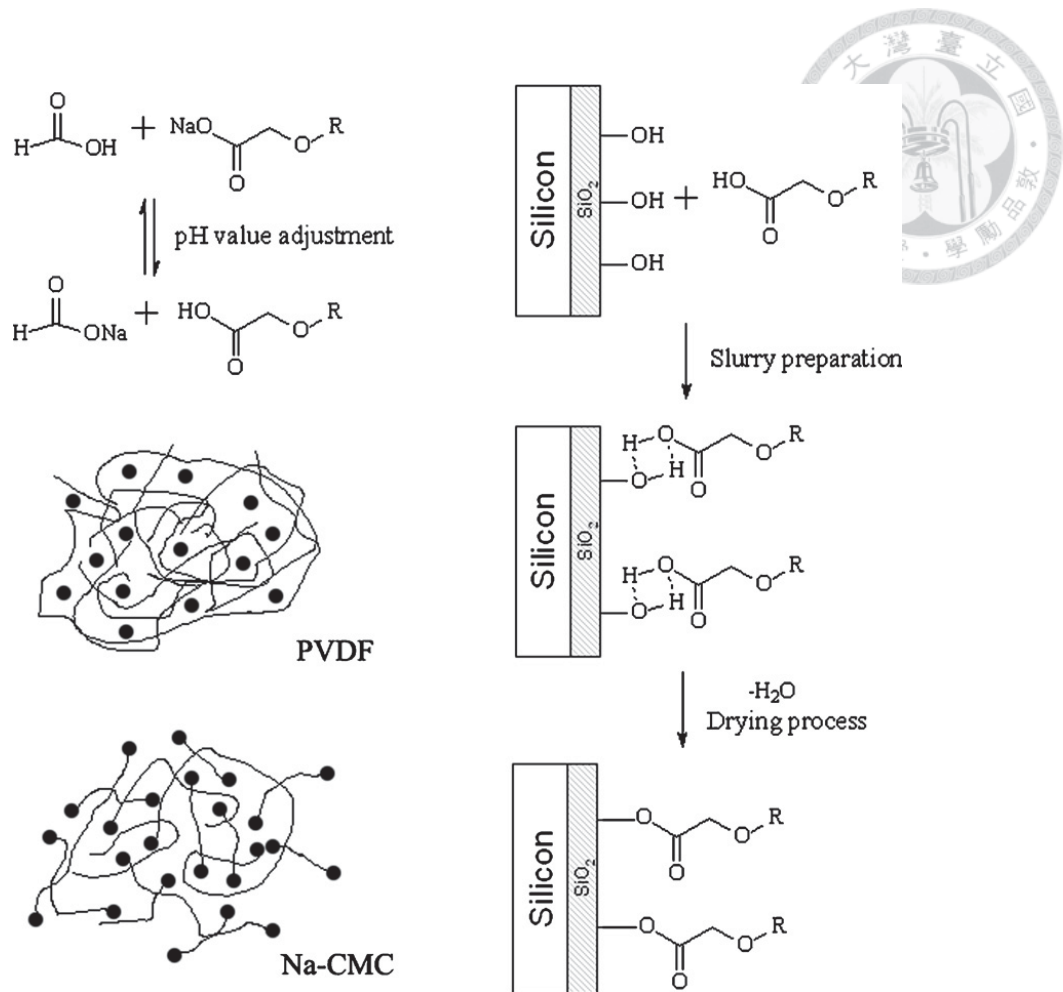
Figure 2.26 Illustration of the esterification between hydroxyl on Si surface and carboxyl in SCMC [70]
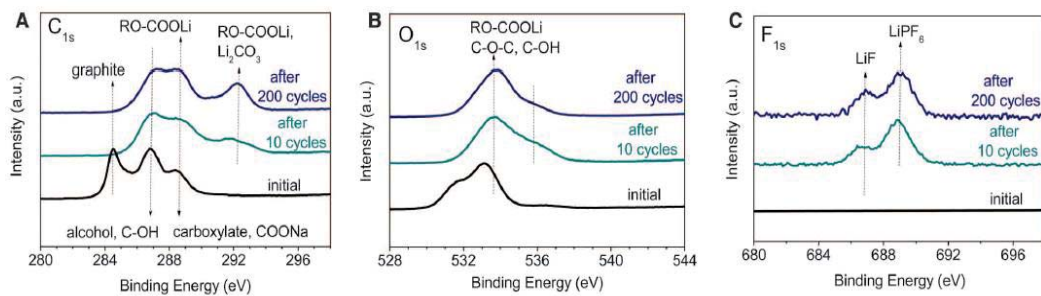
Figure 2.27 Stability of the SEI layer in an alginate-based Si anode. XPS spectra on the anode surface before and after cycling in the potential range 0.01 to 1 V versus Li/LI$^+$. No major changes in the chemistry of the SEI of the anode cycled for 10 or 200 cycles are visible [71].
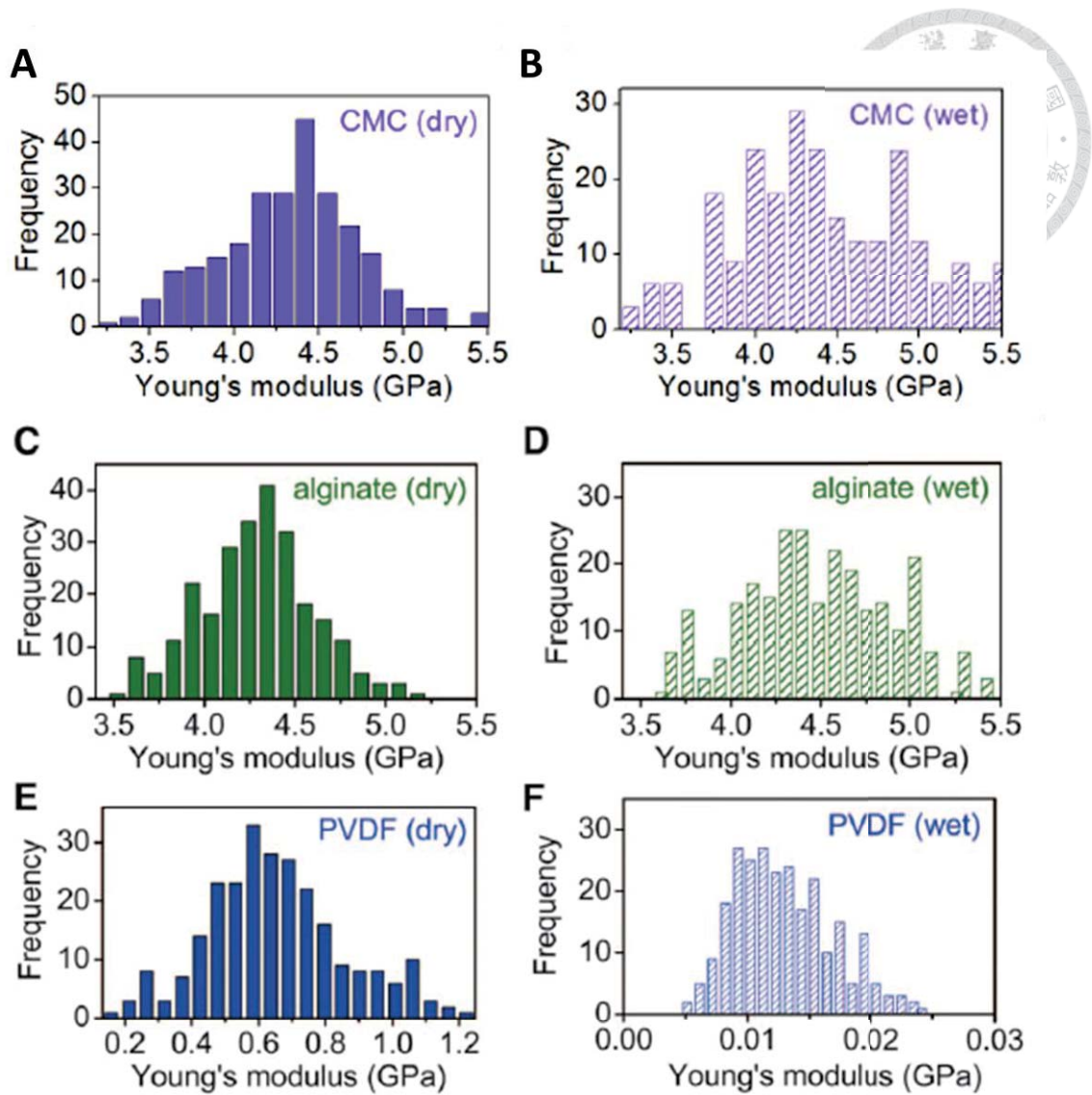
Figure 2.28 Young's modulus of thin films made of different binders. (A), (C), and (E) are in dry states while (B), (D), and (F) are in wet state (impregnated with electrolyte solvent) [71].

Chapter 3 Experimental

3.1 Materials and Chemicals

The materials and chemicals used in this study are listed in Table 3-1. Moreover, all the reagents in this study were of laboratory reagent grade and were used as received without any further purification. The de-ionized water used in all the experiments was purified by a reverse-osmosis system (Purelab Maxima/ELGA), of which the resistivity is 18.2 MΩ-cm.

Table 3.1 Information of materials and chemicals used in this study.

Chemical Reagent	Formula	Assay	Company
100 nm Si	Si	99.0%	Alfa Aesar
40 nm Si	Si	99.9995 %	CREAVIS Gesellschaft for Technologie und Innovation mbH
Zirconium(IV) Propoxide in 1-Propanol	$Zr(OPr)_4$	70.0%	ACROS
Fructose	$C_6H_{12}O_6$	75.0%	豐年果糖
Pitch	C	99.9%	中鋼碳素
Graphite (KS6)	C	99.9%	Timcal
Carbon black (Super P)	C	99.9%	Timcal

Table 3-1. (continued). Information of materials and chemicals used in this study.

Iso-Propanol	C_3H_7OH	99.0%	Nacalai tesque Inc.
Sodium carboxyl methyl cellulose (WS-C)	$-[C_6H_7O_2(OH)_{2.35}(OCH_2COONa)_{0.65}]_n-$	99.0 %	DKS International Inc.
Alginate	$(C_6H_8O_6)_n$	99.0%	Acros
Dimethyl carbonate	$C_3H_6O_3$	99.0 %	Acros
Copper foil (thickness: 14 μm)	Cu foil	99.0 %	Sambo
Lithium hexafluorophosphate in ethyl carbonate/ethyl methyl carbonate 1:2 in vol. with 2 wt% vinylene carbonate	$LiPF_6$ in $C_3H_4O_3/C_4H_8O_3$ 1:2 in vol. with 2 wt% $C_3H_2O_3$	1.0 M	Zhangjiagang Guotai Ronghua (from China)

3.2 Synthesis of ZrO$_2$-Si-C Composite

3.2.1 Synthesize Porous ZrO$_2$ with Sol-Gel Method

The purpose of this research is to develop porous ZrO$_2$ structure as a matrix to buffer expansion of Si during cycling. The preliminary work of constructing a process for making porous ZrO$_2$ is introduced in this chapter.

The sol-gel preparations are carried out in air at ambient temperature. According to the preliminary study, appropriate amount of water is necessary for making porous ZrO$_2$ [14, 15]. Compared to the amount of water added into solution, water adsorbed from ambient atmosphere can be neglected. On the other hand, the concentration of precursor, the drying process and calcinations process are of vital importance in making porous ZrO$_2$ [9].

The experimental procedure of preparing porous ZrO$_2$ by using sol-gel method is demonstrated as follow: First, Zirconium Propoxide ($Zr(OC_3H_7)_4$) is dissolved in 100ml 2-propanol to form 0.01M solution and kept stirring at 400 r.p.m. Second, after stirring for 10 min, proper amount of water (0.56M) is dropped into solution to induce hydrolysis and condensation reaction and kept stirring for 20 min at 400 r.p.m. The basic functions of hydrolysis and condensation are accomplished as follows:

Hydrolysis :

$$Zr(OC_3H_7)_4 + H_2O \longrightarrow Zr(OC_3H_7)_3 - OH + C_3H_7 - OH \qquad (3\text{-}1)$$

Condensation :

$$Zr(OC_3H_7)_3 - OH + Zr(OC_3H_7)_3 - OH \longrightarrow Zr(OC_3H_7)_3 - OZr(OC_3H_7)_3 \qquad (3\text{-}2)$$
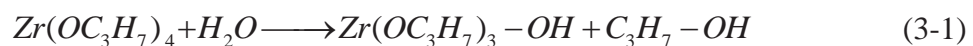
After that, the stirrer is taken off and the solution is dried at 40℃ water bath to remove solvent. As time goes by, the gel shrinks and accompanies with increasing viscosity. After different drying time : 20 hr , 21hr, 23hr, and 29hr, the different states of gel are derived and detailed records are presented in Table 3.2. After drying process, gel is scooped out and treated with calcination. The calcination proceeds at 400℃ under 3% H_2 in N_2 atmosphere for 15 min and cools down naturally. Finally, the powder is collected, ground and sieved with 400 mesh sieve. The flowchart of preparing porous ZrO_2 is illustrated in Fig. 3.1.

454 µl $Zr(OC_3H_7)_{4(l)}$ (0.001 mole)

Dissolve $Zr(OC_3H_7)_{4(l)}$ in 100 ml iso-propanol
Stir at 400 r.p.m. and keep 30℃ water bath for 10 min

1 ml H_2O

0.01 M $Zr(OC_3H_7)_4$ / 0.56 M H_2O
Keep 40℃ water bath for 20 min

Dry for 20 hr, 21 hr, 23 hr and 29 hr and

Scoop out the gel and Calcine it at 400℃ for 15 min under

Grind the powder and sieve it with 400 mesh sieve

Porous ZrO_2 powders
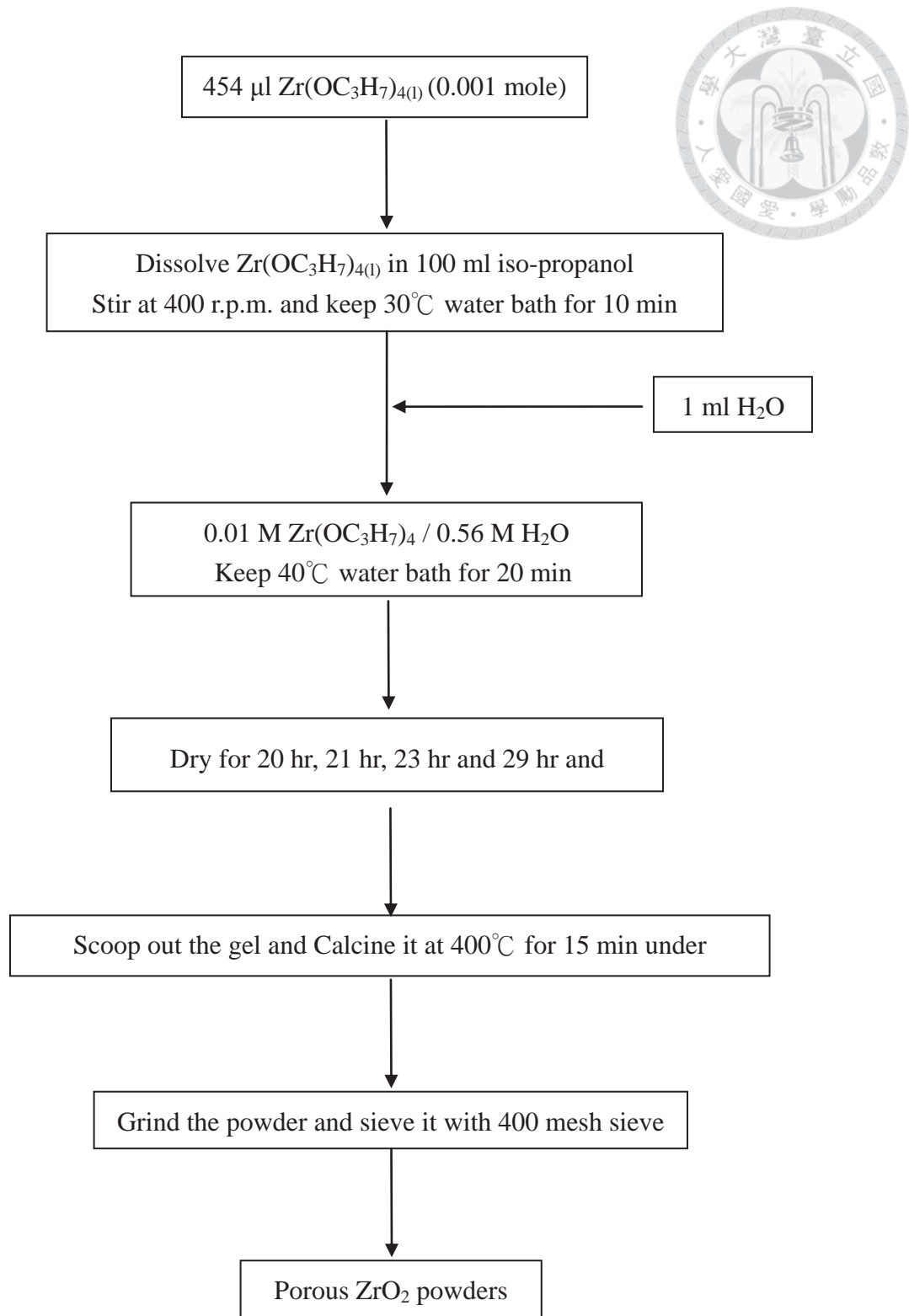
Figure 3.1 Flowchart of synthesizing porous ZrO_2 by sol-gel method with different drying time.

After identifying appropriate state and drying time of gel, the concentration of precursor is also discussed in the following experiments. The different concentration of $Zr(OC_3H_7)_4$: 0.005M , 0.01M, 0.02M, 0.05M and 0.1M proceeds under the same process. The detailed record is presented in Table 3.3 and the relevant digital pictures are listed in Fig. A.1.

Table 3.2 Records of gel with different drying time (0.01M $Zr(OPr)_4$)

Conc. of Precursor	Initial Solution Volume	Drying Time	Final Gel Volume
0.01M	100 ml	20 hr	10.1 ml
0.01M	100 ml	21 hr	9.1 ml
0.01M	100 ml	23 hr	7.6 ml
0.01M	100 ml	29 hr	< 2 ml
0.01M	100 ml	48 hr	< 2 ml

Table 3.3 Records of gel with different concentration of precursor

Conc. of Precursor	Initial Solution Volume	Drying Time	Final Gel Volume
0.005M	200 ml	15 hr	2.5 ml
0.01M	100 ml	23 hr	7.6 ml
0.02M	50 ml	18 hr	7.0 ml
0.05M	20 ml	17 hr	6.2 ml
0.1M	10 ml	10 hr	3.2 ml

3.2.2 Synthesize ZrO_2/Si/C Composite with Sol-Gel Method

Based on the research in chapter 3.2.1, ZrO_2/Si composite with a porous structure is achievable by the similar processing. In addition, adding conductive material into this composite is necessary since ZrO_2 is well-known as insulator and Si is also a poor conductor; therefore, carbon coating is applied to the porous ZrO_2 / Si structure to make ZrO2 / Si / C composite. There are two ways for carbon coating in this experiment, and the physical properties and electrochemical performance would be discussed in chapter 4.

The first carbon-coating method is fructose carbon coating and the process is similar to Fig. 3.1. After the ZrO_2 / Si gel dries to proper state (crack just forms), it is soaked in 20 wt% fructose solution which is prepared previously and treated with high-speed rotation (around 4000 r.p.m) for 5 min in order to mix ZrO_2/Si and fructose solution homogeneously. Then, the container is sealed (for avoiding further drying) for 1 hour in 40℃ water bath and followed by filtration. Finally, gel is collected (See Fig. A-2) and treated with calcination under vacuum to reserve carbon to the maximum content. The vacuum equipment is presented in Fig. 3.2 and detailed process is illustrated in Fig. 3.4.

Pitch is adopted as carbon precursor in the other work. First, ZrO_2 / Si gel is previously calcined to derive porous ZrO_2 / Si powder. At the same time, proper amount of pitch is dissolved in acetone to have a homogeneous solution. Then, ZrO_2 / Si powder is dispersed in the pitch solution and the well-mixed solution would be dried in 40℃ water bath to remove acetone. Afterward, the dried ZrO_2 / Si / Pitch powder is treated with calcination at 900℃ under 3% H_2/N_2 (See Fig. 3.3). Then, the derived ZrO_2 / Si / C powder is collected, ground and sieved with 400 mesh sieve. The complete process is illustrated in Figure 3.5. Note that the heating strategy kept

the same, that temperature raised from R.T. to assigned temperature (500℃ and 900℃) with constant rate of 7℃/min.
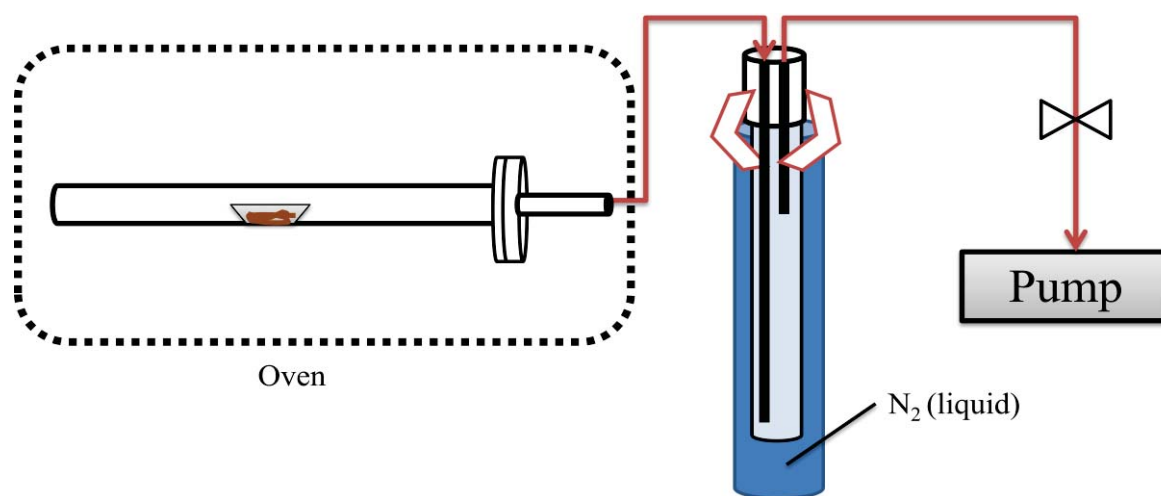
Figure 3.2 The calcination equipment with pump and cooling apparatus for solvent trapping.
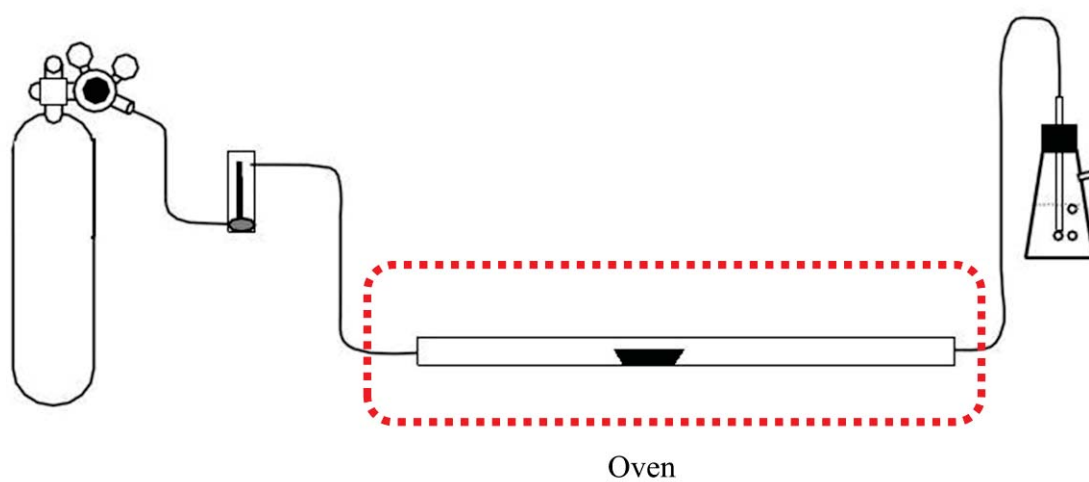
Figure 3.3 The calcinatioin equipment with purging gas, 3% H_2 in N_2.
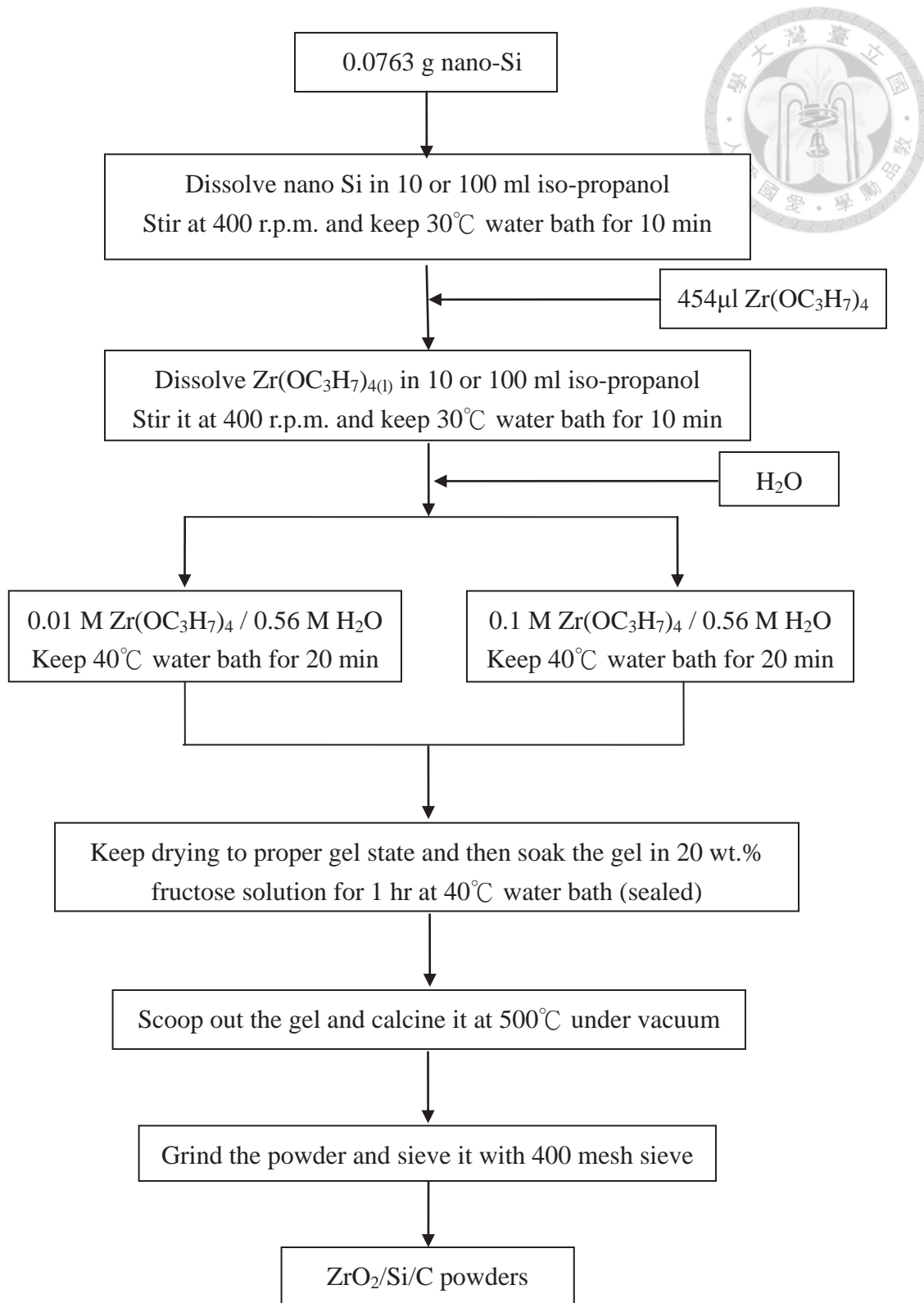
Figure 3.4 Flowchart of synthesizing porous ZrO_2 / Si / C with fructose as carbon source.
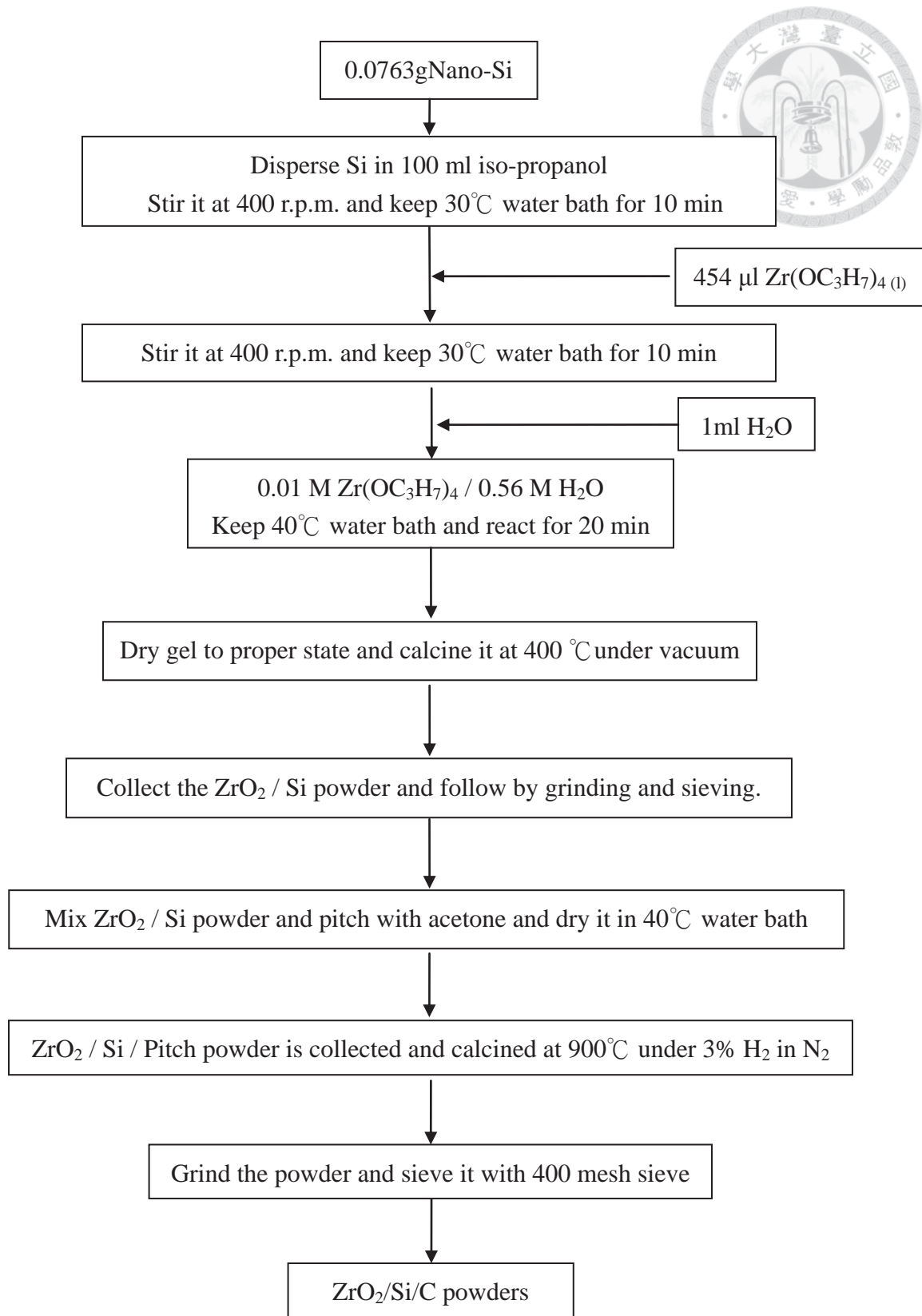
Figure 3.5 Flowchart of synthesizing porous ZrO_2 /Si/C with pitch as carbon source

3.3 Analysis and Characterizations

3.3.1 X-ray Diffraction

Phase identification was predominantly performed by X-ray diffraction (XRD) analysis. Typically, information like phase purity, crystallinity, and size and shape of unit cell can be obtained from a XRD pattern. The x-ray beam generated from the X-ray tube encounters the sample, and the diffracted X-ray beam must obey Bragg's law:

$$n\lambda = 2d\sin\theta \tag{3-3}$$

where n is the order of diffraction, positive integer; λ=wavelength of incident beam; d=distance between corresponding crystal lattice plane; and θ=the incident angle between x-ray beam and atomic layers in the crystal, also called Bragg's angle. Figure 3.6 simply describes the relationship between the incident beam, diffracted beam, d-spacing, and Bragg's angle in Bragg's law [65].

In this study, XRD analysis was carried out with the X-ray diffractometers (MAC Science/MXP and Philips/X'Pert) which use Cu K_α radiation ($\lambda = 1.5418$ Å) as the source of X-ray. The X-ray generator equipped with a graphite monochromator and the applying voltage and current was 40 kV and 30 mA, respectively. The reflection data of powder samples was collected under a continuous-scanned θ-2θ mode at a scan-rate of 10 °/min. The scan-range was operated at the range of 10 to 80°. Figure 3.7 depicts the typical features of XRD experiment [72].

In addition, average crystallite size can be determined based on the Debye-Scherrer equation, adopting the full width at half maximum (FWHM) of the specified reflection in diffraction patterns, described as:

$$d = \frac{0.9\lambda}{\sqrt{B^2 - b^2}\cos\theta_B} \tag{3-4}$$

where d is the average crystallite size, λ is the wavelength of incoming X-ray, B is the revealed FWHM of the specific reflection, b is the line broadening width of instrument, and θ is the Bragg angle. The XRD information of silicon and graphite based on Cu K_α radiation is listed in Table 3.4.
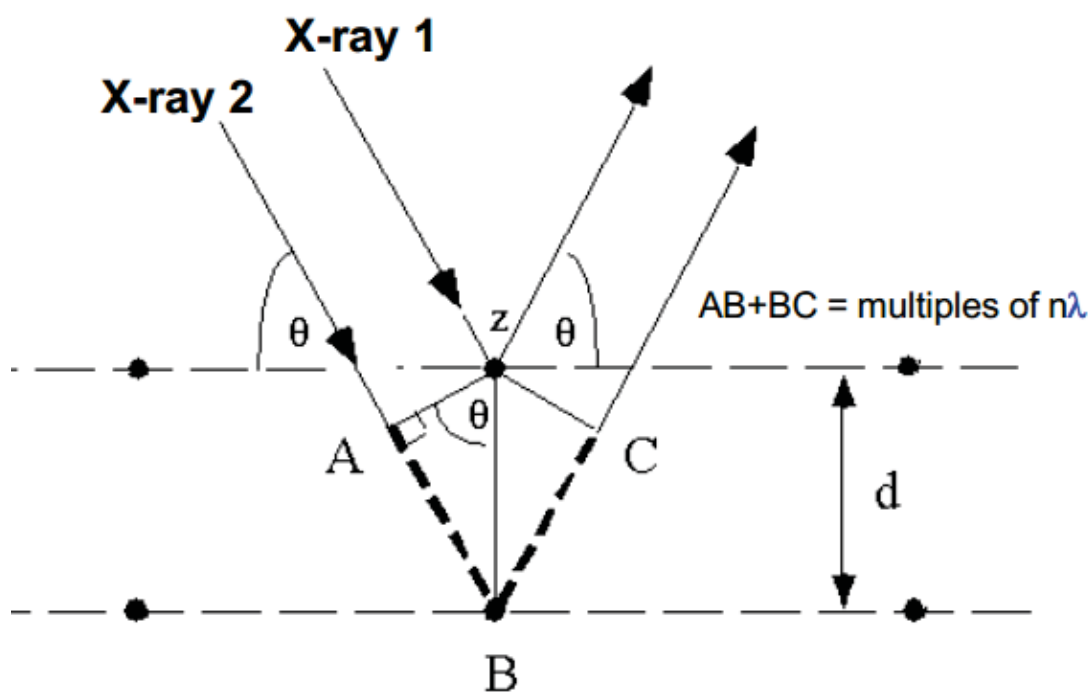
Figure 3.6 2-dimensional schematic representation of the Bragg's law [73].
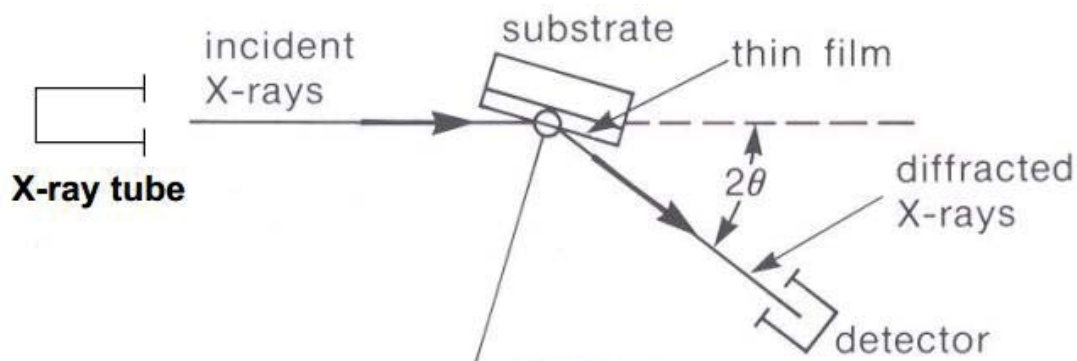
Figure 3.7 Basic features of XRD experiment [72].

Table 3.4 The XRD information of materials involved in this study ($\lambda = 1.5184$ Å)

Si (27-1402)	Plane	*(111)*	*(220)*	*(311)*	*(400)*	*(331)*	*(422)*	*(511)*
	2θ (°)	28.466	47.344	56.171	69.196	76.452	88.118	95.052
	I/I_o	100	55	30	6	11	12	6
$ZrO_2(c)$ (27-0997)	Plane	*(111)*	*(200)*	*(220)*	*(311)*	*(222)*	*(400)*	
	2θ (°)	30.168	35.023	50.375	60.026	62.728	73.997	
	I/I_o	100	24	80	60	10	12	
$ZrO_2(m)$ (37-1484)	Plane	*(331)*	*(422)*	*(511)*	*(640)*	*(822)*	*(771)*	
	2θ (°)	13.097	14.767	15.669	21.736	25.733	30.202	
	I/I_o	20	45	55	20	100	20	
$ZrO_2(t)$ (42-1164)	Plane	*(101)*	*(002)*	*(110)*	*(102)*	*(112)*	*(200)*	*(103)*
	2θ (°)	29.832	34.024	34.855	42.355	49.511	50.112	58.328
	I/I_o	100	39	34	2	34	38	12
C(graphite) (41-1487)	Plane	*(002)*	*(100)*	*(101)*	*(004)*	*(103)*	*(110)*	
	2θ (°)	26.40	42.26	44.43	54.59	59.75	77.32	
	I/I_o	100	2	4	6	1	3	

3.3.2 Scanning Electron Microscopy

Morphology observation on a material can provide some important information in the initial stage before going further investigation, such as approximate particle size distribution, the shape and microstructure of particles, topography, and porosity, etc. The scanning electron microscope (SEM) is a microscope that uses electrons instead of light to form an image. The SEM has advantages over traditional optical microscopes (OM) and has become one of the most heavily used instruments in

research areas today. For instance, the SEM has a large depth of field, which allows more of a specimen to be in focus at one time. The SEM also produces images of high resolution, which means that closely spaced features can be examined at a high magnification. Moreover, preparation of the samples is relatively easy since most SEM only require the sample to be conductive.

The particle morphology was examined by SEM (FEI/Nova230). Before examination, the samples were first pasted on a carbon-tape glued holder, and then coated with platinum or gold by ion sputtering to ensure the conductivity. Energy dispersive x-ray spectroscopy (EDS, Oxford Instrument/model: 6587) were used to analyze the surface compositions of electrodes.

3.3.3 Pore Volume and Pore Size Distribution Analysis

The BET (Brunauer, Emmett, and Teller) surface area and pore size distribution, determined by nitrogen adsorption, of materials was conducted with a surface area analyzer (Micrometrics/ASAP 2010). BET method involves multiple-payer adsorption, of which equation is described as:

$$\frac{P}{V(P_0 - P)} = \frac{1}{V_m C} + \frac{(C-1)P}{V_m C P_0}$$

(3-5)

where V is the volume of adsorbed nitrogen (cm^3/g); P, the pressure of adsorbed gas; P_0, the saturated vapor pressure ; V_m, the volume of mono-layer adsorbed nitrogen; and C is constant. A linear relation of $P/(V(P_0-P))$ and P/P_0 can be obtained, which gives a slope of $(C-1)/V_m C$ and intercept of $1/V_m C$; and thus the specific surface area can be calculated based on the volume of adsorbed nitrogen. BJH (Brunauer, Joyner, and Halendar) scheme for determination of mesopore distribution is based on Kelvin equation and thickness equation, showing the relation between relative pressure and

pore size. In this study, 5-points measurement was utilized for determining BET surface area, in which the relative pressure ranging from 0.06 to 0.20; in the meanwhile, 55-points detection was measured for mesoporous characteristics. The equilibrium interval time was set as 20 s.
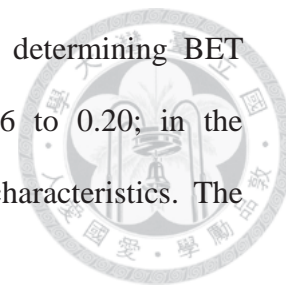
3.3.4 Determination of Carbon Content

It is an important issue to determine the carbon content of the synthesized samples. In this research, ZrO_2-Si is always coated with carbon to improve its intrinsically low electronic conductivity and cushion volume change of Si during Li^+ insertion/extraction. Besides, different microstructures of carbon give various electrochemical properties. Thus, carbon content should be detected to calculate the actual specific charge and discharge capacity of the composite and to estimate its influence not only on cycle stability but also reversibility.

Elemental Analysis (EA) is conducted to measure the carbon content. It is a combustion analysis technique: a carefully-weighted amount is completely burned under oxygen atmosphere. Take carbon and hydrogen analysis of C_xH_y as an example, it can be described in the following equation:

$$C_xH_y + zO_2 \rightarrow \frac{y}{2}H_2O + xCO_2$$

(3-6)
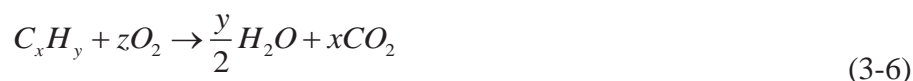
The measurement is processed in presence of excess oxygen atmosphere. As the amounts of H_2O and CO_2 in exhaust gas are measured, the original composition of carbon and hydrogen contained in the compound can be obtained. In this way, the carbon content of carbon can be known by measuring the amount of CO_2. The machine used here is Heraeus VarioEL-III (for CHN).
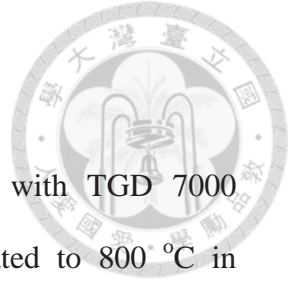
3.3.5 Thermo Gravimetric Analysis

Thermo Gravimetric analysis (TGA) was also performed with TGD 7000 (ULVAC Sinku-Riko, Inc.) thermal analyzer. Samples were heated to 800 ^{o}C in nitrogen at a heating rate of 10°C/min. The weight of testing samples was 30-35 mg and the precision of the method was ± 0.1 mg. In this research, TGA is used to observe the mass variation of gel or pitch with increasing temperature. Therefore, a proper calcination temperature could be determined for making ZrO_2-Si-C composite.

3.3.6 Particle Size Distribution Analysis

The particle size distribution (PSD) was performed by Coulter Counter LS230 (Coulter Corp., USA). Samples were dispersed in appropriate solvent to avoid severe aggregation. The detective range ranges from 0.4 μm to 2000 μm. The detecting method is "Static Light Scattering".   The theorem based on Raleigh Single Slit equation :

$$\sin\theta = \frac{\lambda}{d} \tag{3-7}$$

The scattering angle decrease with increasing detected particle size.

3.4 Electrochemical Characterizations

3.4.1 Preparation of Electrode

The slurry composition is listed in Table 3.5. The ZSC (i.e. ZrO_2/Si/C) electrodes are composed of 80 wt. % active material, 12 wt. % conductive additives and 8 wt. % binder. The conductive additives is a mixture of graphitic flakes (KS6, Timcal) and nano-sized carbon black (Super P, Timcal) at a weight ratio of 2:1 ; the binder is alginate (also called alginic acid or algin, ACROS) or SCMC/SBR.

In order to let particles well dispersed in the slurry, the following steps are required. At first, all powders are weighted and put into a mortar and grind it around 15 minutes by pestle manually. The grinding process is to make sure that particles are well-mixed. Then, add proper amount of DI-water into mortar and grind the mixture around 10 minutes until slurry is in a proper condition (as viscous as toothpaste).

The well-mixing slurry is then uniformly coated on a Cu foil (Sambo, 99.9%) by using a coating machine from All Real Technology Co., Ltd. After drying at 90℃ (hot plate's surface temperature) in air, the coating layer has a final thickness of 30-40μm. In order to obtain better contact between solid contents themselves and copper foil, furthermore enhancing electronic conductivity, the electrode is rolled to 65-70％ of its original thickness. To fabricate the coin cell, the electrodes are cut into disks of 13 mm in diameter for an anode electrode. The electrodes are further dried at 150℃ in vacuum for 6 hours to remove any residual water or solvent before doing cell assembling.

Table 3.5 Slurry composition of anode electrode

Component	wt. %
ZrO_2/Si/C	80
KS6	8
Super P	4
Binder[*]	8
DI-water	400

[*]: 8 % Binder is 8% alginate, or 4% SCMC + 4 % SBR

3.4.2 Cell Assembling and Dismantling

Coin cell (CR2032) is made of stainless steel and has a diameter of 20 mm and a height of 3.2 mm. CR2032 cells are fabricated for half cell evaluation using Li foil as the counter and reference electrode. As shown in Fig. 3.8, the coin cell consists of an anode electrode, a top cap, a bottom cap with polypropylene (PP) ring to make sure coin cell well sealed, polyethylene (PE) separator, a disk on which Li foil is put and serves as a current collector of counter electrode, and a spring.

The electrolyte is 1 M $LiPF_6$ in ethylene carbonate (EC): ethyl methyl carbonate (EMC) 1:2 in vol. % with or without 2% vinylene carbonate (VC) as an additive. All the cell-assembling processes are carried out in a dry room where the dew point maintains at about -60 ~ -40 ^{o}C.

For the investigation on morphology (SEM) and thickness of the electrodes, the cycled cells are carefully dismantled. The cycled electrodes are thoroughly rinsed with dimethyl carbonate (DMC) to remove residual electrolyte and lithium in a glove box. The rinsed electrodes are placed in the glove box and dried for 1 day before

analyses. The electrodes are transferred into the analytic instruments without vacuum protection since the exposure time to air has been reduced as possible.
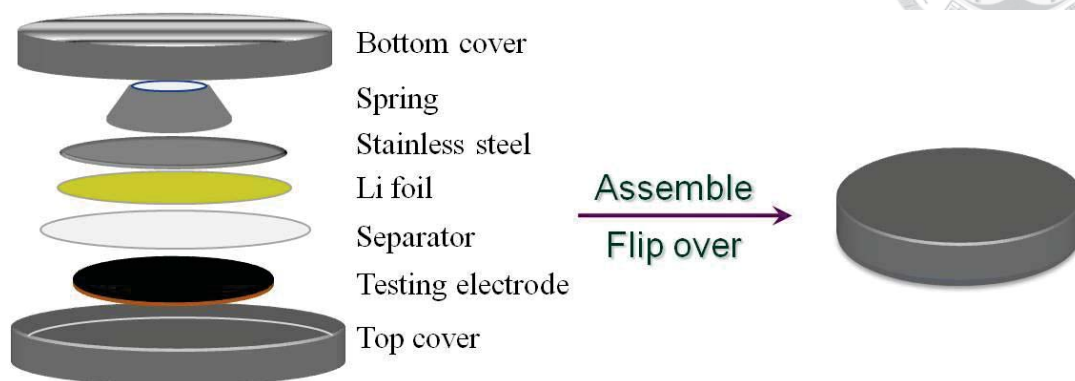
Figure 3.8 Schematic drawing of a coin cell.

3.4.3 Electrochemical Charge/Discharge Tests

Constant current constant potential (CCCP) strategy is adopted to analyze electrochemical performances and it can also meet the demands of real application in lithium ion batteries. This strategy consists of two modes, CC and CP, which contains following steps : (i) discharge at "the certain current" until the 0.005 V was reached and (ii) continuously discharge at a constant potential of 0.005 V until one-to-third "the certain current" is reached, and (iii) charge at a constant current of "the certain current" until the cut-off voltage (1.2V) is reached.

To further determine "the certain current", concept of C-rate is introduced. For example, 0.05C means you can discharge or charge your cell completely in 20 hrs; 0.5 C means you complete this work in 2 hrs; n C means you can complete it in 1/n hrs. Therefore, we have to calculate theoretical capacity of cells in advance. In this research, batteries are cycled at 0.05C at the first two cycles for SEI formation and then tested at 0.20C between 0.005 and 1.2V. The electrochemical experiments were carried out on battery tester, BAT -700 (AcuTech Systems Co., Ltd.).
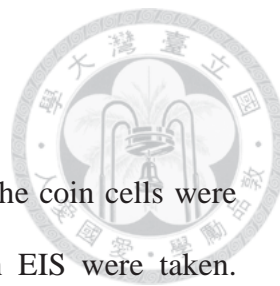
3.4.4 Electrochemical Impedance Spectroscopy

For electrochemical impedance spectroscopy (EIS) analysis, the coin cells were consecutively lithiated / delithiated on assigned cycles at which EIS were taken. Measurements were conducted after open-circuit voltage (OCV) is stabilized at a constant value. An Autolab PGSTAT100 (Metrohm Autolab) frequency response analyzer was employed for obtaining the spectra within frequency range from 10 mHz to 100 kHz. All the analyses described above were carried out on the electrodes in delithiation state.

3.4.5 Raman Spectroscopy

Raman spectroscopy can provide the information of molecular vibrations whose are complementary to that of infrared spectroscopy can give. It is a scattering technique, samples are placed in the laser beam and backscattered signal is collected.

Here, Raman analysis is applied to identify the coordination of coated carbon layer. The sample is in powder form and spread on the holder. *The* spectra were collected on a *Renishaw 2000* micro-Raman Fourier transform spectrometer using an Ar^+ laser at 514 nm as the excitation source. The Raman system was also equipped with a microscope (Olympus/BH2-UMA) which allowed accurate alignment of the laser beam onto the device.

Chapter 4 Microstructrual Characterization of ZrO$_2$/Si/C composite

4.1 Introduction

In the previous studies, ZrO$_2$ coating has been adopted as a coating layer to enhance the mechanical strength of active material for both cathode and anode materials of LIB [62, 74]. Besides, a porous matrix of ZrO$_2$-Si composite deposited on film was also achieved by sol-gel method with structure-directing agent [63, 64]. However, in order to reach industrial application, simplifying the process and instead of ZrO$_2$-Si thin film, deriving a ZrO$_2$-Si powder which can guarantee enough active material loaded on the electrode would be the subject in this research.

4.2 Microstructural Characterization of Porous ZrO$_2$ Structure

4.2.1 Different Drying Time

Experimental details were illustrated in Chapter 3.2.1. The gel was put in the hood and dried in air. The variations of gel state and volume were recorded. Initially, a gel shrank by an amount equaling to the volume of solvent which has evaporated. And this is well-known as "Constant Rate Period" [9]. The reduction of solvent would lead to increasing concentration of the precursor and therefore accelerate the cross-linking rate.

The falling-rate period came after constant rate period and there was no obvious demarcation between two periods. Here the critical point is decided to differentiate these two periods due to its large elevation of stiffness. As the gel dries and shrinks, its more compact structure and associated additional cross-linking lead to increased stiffness. At the critical point, the gel becomes sufficiently stiff to resist further shrinkage as liquid continue to evaporate. At this point, the liquid begins to recede into the porous structure of the gel. Due to its surface tension and the small size of the gel pores, very large pressure are generated across the curved interfaces of the liquid menisci in the pore. And the gel bulk would crack due to this capillary stress.

In this experiment, the Dry-20hr gel sample is decided to be the critical point sample since it's stiff enough to be non-flowing (Fig. A.3). After 1 hr (already dried for 21hr), the gel shrinks a little and it's the Dry-21hr gel sample. However, after 3hr, the crack formed in Dry-23hr sample (See Fig. A.3) and the gel started to shrink very fast. After 9hr, the Dry-29hr sample is derived and its volume almost didn't changed

with further drying. The detailed volume change was recorded in Fig. 4.1.

The densification treatment for gel came right after the drying process. Fig. 4.2 showed TGA analysis of Dry-23hr gel sample. The TGA analysis indicated that the gel continually suffered from weight loss due to its evaporation of solvent and condensation of small molecules in the gel. The weight loss reached a plateau after 400℃ and started to have structural relaxation. Thus, calcination temperature for 400℃ of each gel sample is decided in order to retain its porous structure to the maximum degree and reasonably compare each sample.

The meso-pore distribution of each porous ZrO_2 showed two peaks (Fig. 4.3). The left peak indicates that large amount of small pores (< 10nm) existed in the porous ZrO_2 and the right peak was contributed by large pores (> 10nm). The calcined Dry-23hr sample provided more pore volume which mainly came from more large-pore volume. Thus, the inference is drawn from Fig. 4.3 that the state of gel before calcinations is critical for generating large pore volume. Compared with Dry-20hr and Dry-21hr sample, the Dry-23hr had more large pores which might came from complicated interaction between surface tension and structural relaxation which would not be the main points discussed in this research. Besides, the xerogel presented in Fig. 4.3 is the gel sample without 400℃ calcination (only with 120℃ heat treatment for 8 hr to remove residual solvent). On the other hand, the BET isotherm (Fig. 4.4) indicated that the pore structure is typically cylindrical and thus showed no hysteresis during adsorption and desorption process.

The pore of ZrO_2 is designed to accommodate the expansion of Si during electrochemical charge and discharge cycling. To well buffered the nano-Si (~40nm or ~100nm) needs more large pores. The LPR (i.e. large-pore ratio) is introduced and represents the volume ratio of large pore (i.e. d > 40nm) to overall pore. Fig. 4.5 is made to quantitatively compare BET surface area and illustrate pore volume

distribution. The LPR ratio of each sample ARE as follows : Dry-20hr : 51.0% , Dry-21hr : 53.5% , Dry-23hr : 62.6% , Dry-29hr : 46.8%, xerogel-no calcinations : 10.1%. From both quantitative perspective (pore volume) and qualitative perspective (LPR), the Dry-23hr sample is taken as the optimal drying time for deriving the most pore volume and the largest LPR. To be more precise, the moment when the gel became stiff enough and the crack formed at the very beginning would be the proper state for gel to do calcinations.
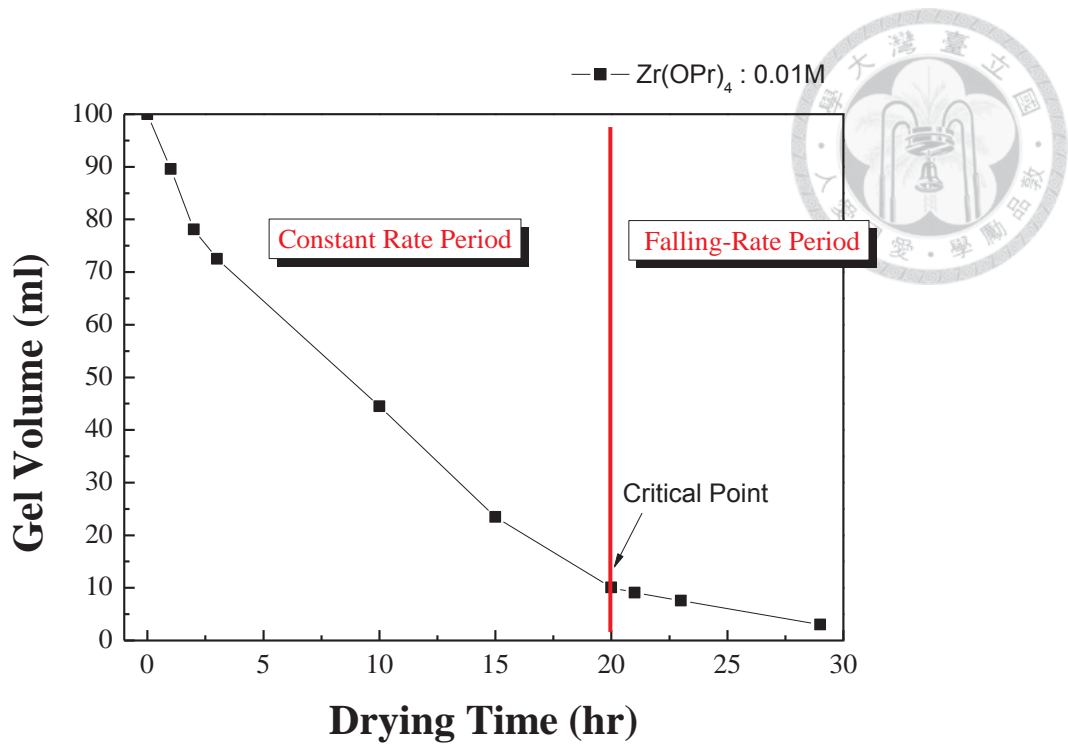
Figure 4.1 Records of decreasing gel volume due to drying process.
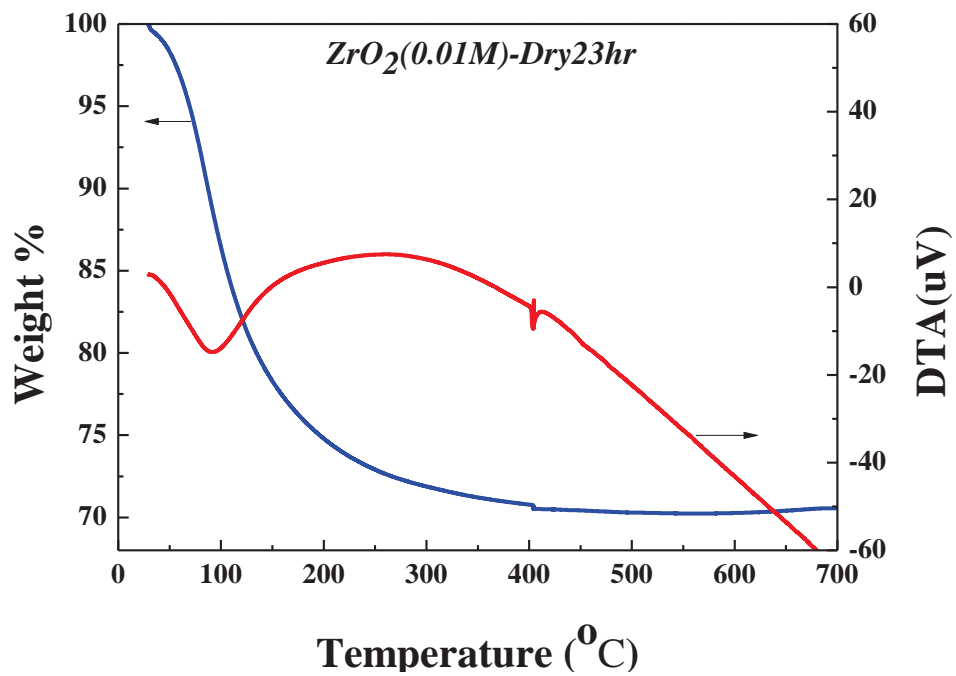
Figure 4.2 The TG-DTA analysis of $ZrO_2(0.01M)$-Dry23hr gel sample with $7{℃}/min$ as heating rate and under nitrogen atmosphere.
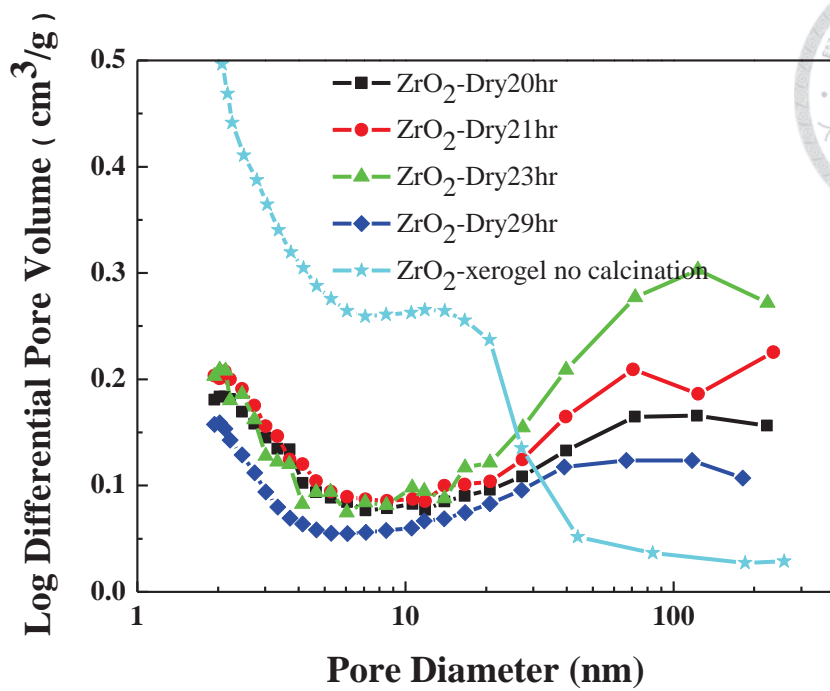
Figure 4.3 The adsorptive meso-pore distribution of different porous ZrO_2 sample.
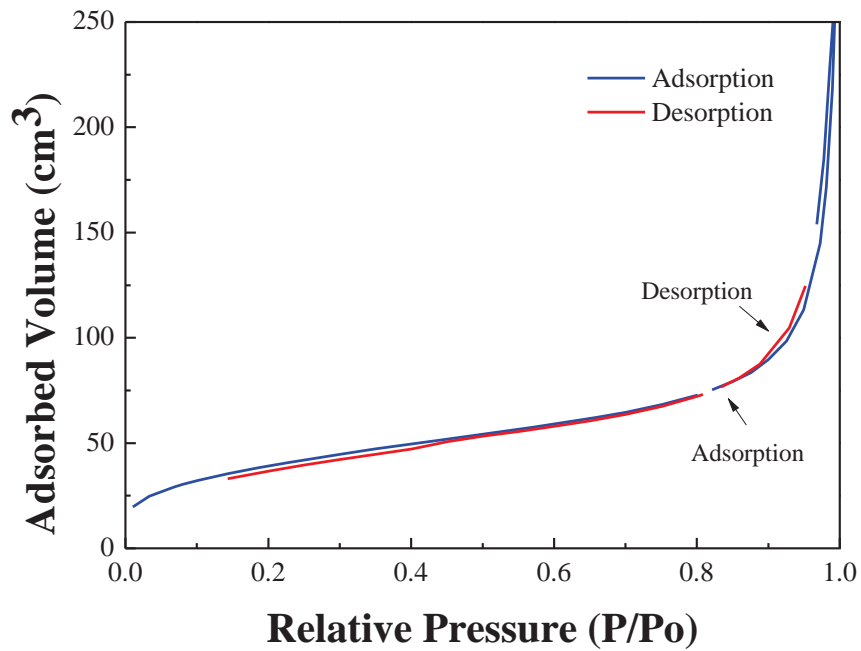
Figure 4. 4 The Langmuir Isotherm of ZrO_2(0.01M)-Dry23hr-400℃ calcination.
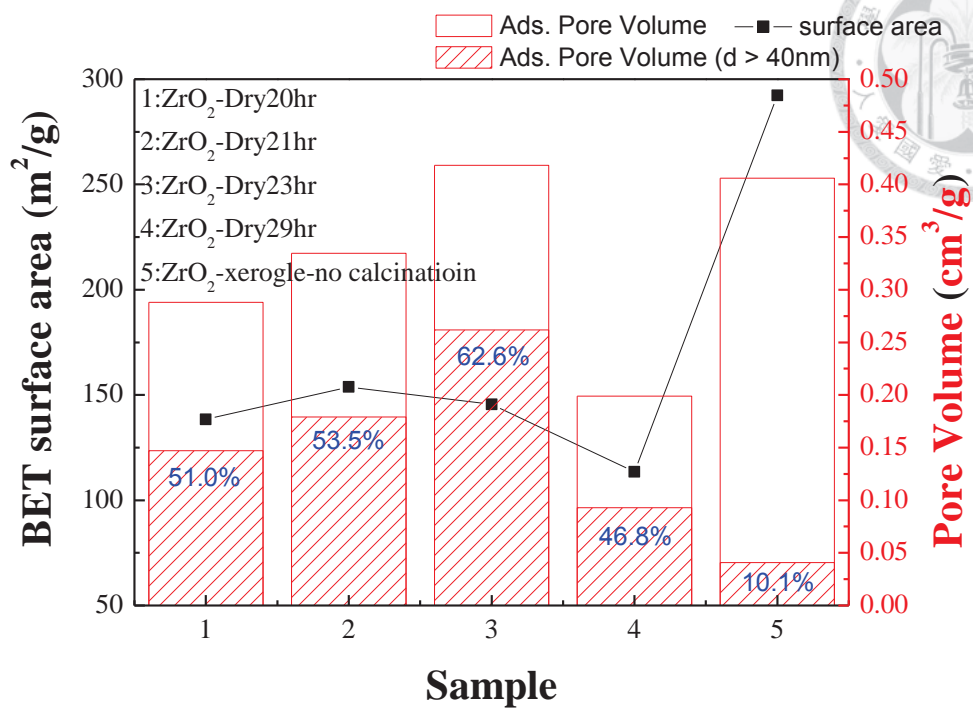
Figure 4.5 The BET surface area and pore volume of different porous ZrO_2 sample.

(The numbers in the columns represent values of LPR.)

4.2.2 Different Concentration of Precursor

The inference that a proper state of gel before calcination plays an important role in making porous ZrO_2 has been drawn in Chapter 4.2.1. In this chapter, the influence of the concentration of precursor on pore distribution would be discussed.

The gel sample: ZrO_2-0.1M, ZrO_2-0.05M, ZrO_2-0.02M, ZrO_2-0.01M, and ZrO_2-0.005M are made by the similar procedure presented in Figure 3.2 but with different concentration of precursor. They were treated with calcination as soon as the crack formed (the optimal state). The digital picture is collected in Fig. A.1. When the crack formed, ZrO_2-0.01M left the most gel volume (See Table 3.3). $ZrO2$-0.0$_2$M and ZrO_2-0.05M had less pore volume and ZrO_2-0.1M has least pore volume of all which might be referred to its less pore structure existed in gel. It seems that the decreasing concentration of precursor might reserve pore structure to the maximum degree. However, once the concentration was drawn down to 0.005M or less, the concentration of precursor was so low that the hydrolysis rate became much higher than condensation rate. The mole ratio of water to alkoxide are large than 100 (0.56M/0.005M=112) which indicate that the hydrolysis should be fast (enough water) and the condensation should be suppressed due to less collision. On the other hand, from Fig. A.1, ZrO_2-0.005M displayed much more transparent and less volume left than others which might be referred to its less pore volume and cross-linking structure.

The meso-pore distribution of each calcined sample was collected (See Fig. 4.6). The large pore (pore size > 40nm) diminished with increasing concentration of precursor. This result could be attributed to the appropriate hydrolysis and condensation rate controlled by concentration of precursor. As depicted by previous study [9], the hydrolysis process occurred as soon as the water was added into the

solution and followed by partial condensation process. And with the evaporation of solvent, the concentration of hydrolyzed monomer increased and accelerated condensation process. Finally, the overall 3D net structure of gel is complete and accompanied with lots of large and small pore. The BET surface area and pore volume of each sample are collected in Fig.4.7. Combined with Table 3.3, the conclusion that the with the same amount of ZrO_2 and under the same gel state (crack formed), the more gel volume might guarantee more porous ZrO2 structure (i.e. more pore volume) after calcination.
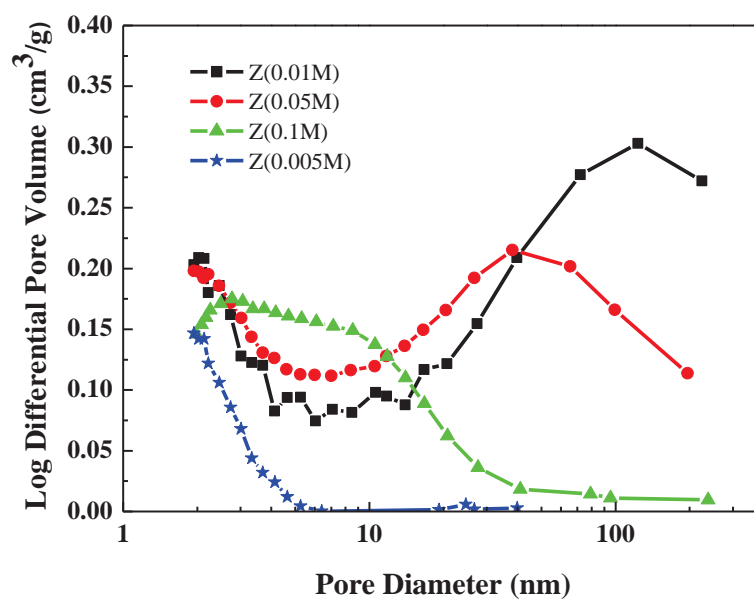
Figure 4.6 The adsorptive mesopore distribution of different porous ZrO_2 sample (ZrO_2-0.01M, ZrO_2-0.05M, ZrO_2-0.1M and ZrO_2-0.005M).
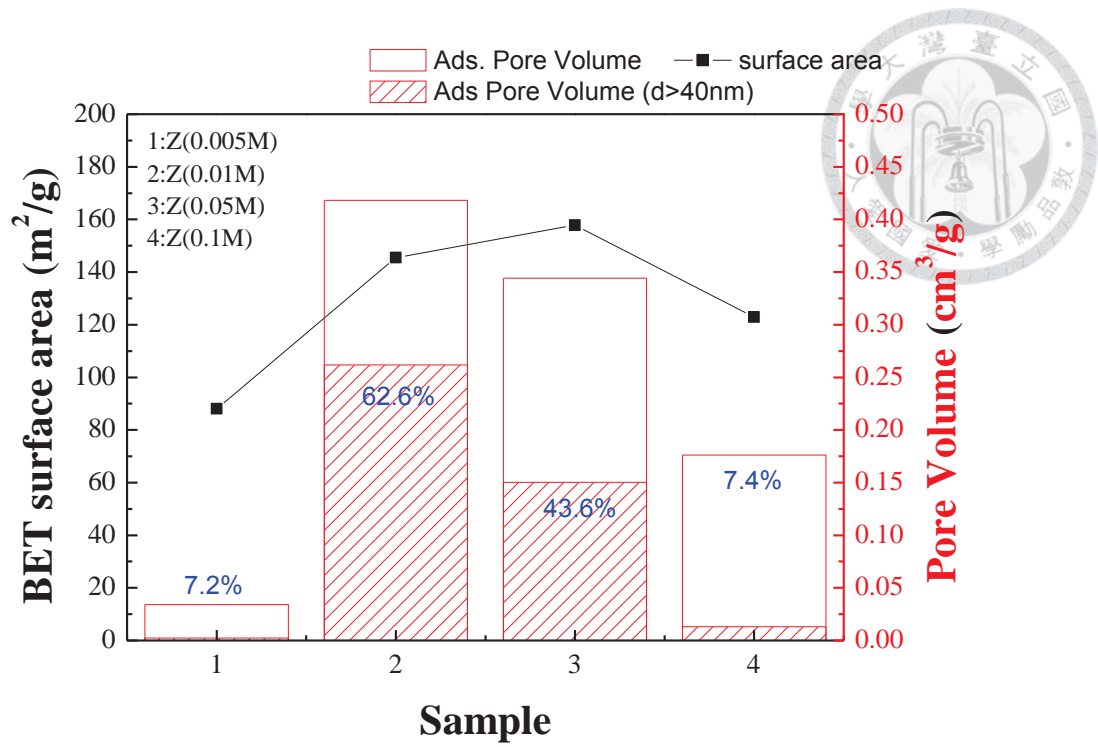
Figure 4.7 The BET surface area and pore volume of different porous ZrO2 sample (ZrO_2-0.01M, ZrO_2-0.05M, ZrO_2-0.1M, ZrO_2-0.005M). The number in percentage represents value of LPR.

4.2.3 Different Temperature and Atmosphere in Calcination

Remember that chapter 4.2 is the preliminary work for making $ZrO_2/Si/C$ in chapter 4.3. In chapter 4.3, high temperature treatment is necessary for deriving better quality carbon from dissociation of pitch or fructose. Therefore, the effect of higher temperature treatment in making porous ZrO_2 has been investigated in this chapter.

The typical stage of densification process can be separated into three stages which were introduced in chapter 2.1.8. At the third stage of calcining silica gels, a sharp increase in shrinkage rate of gel is observed with little or no further weight loss. Similarly, from figure 4.2, there is no obvious weight loss in calcining ZrO_2 gel after 400℃. Therefore, a reasonable conclusion is made that after 400℃, the gel possibly goes through a fierce shrinkage both in volume and surface area which is thermodynamically favored due to its lower surface energy.

In order to flexibly control the pore distribution of calcined ZrO_2 gel, another innovative calcination condition, vacuum, is designed to deal with ZrO_2 gel. The equipment is illustrated in Fig. 3.3. From Fig. 4.8 and Fig. 4.9, the effect of increasing calcinations temperature on pore distribution is separately illustrated. Combined with Fig. 4.10, the quantitative analysis to compare surface area and pore volume, several conclusions were made as follows :

After 400℃, surface area decreases a lot because the large amount of small pore diminishes with increasing temperature. The small pores might merge into large pore or just disappear because of sintering or other reasons.

The major effect of vacuum environment on densification process is its reservation of pore volume and better LPR. Compared with calcination in 3% H_2/N_2, the disappearance of micro-pores occurred in lower temperature (500℃) in vacuum environment. The possible reason is that under vacuum environment, the removal of

organism and condensation process (mentioned in the second stage of densification in chapter 2.1.8), proceed more completely rather than under 3% H_2/N_2. Therefore, a large amount of reserved small pores starts to merge to form larger pores.

Calcination under 3% H_2/N_2 suffered a severe reduction of pore volume which was attributed to its better heat transfer (conduction + convection) and higher possibility of removing surface hydroxyl group of gel which is well-known as passivation treatment. Those two reasons might boost the sintering of porous ZrO_2.

On the other hand, that crystallinity growing with increasing temperature is observed from the XRD analysis (Fig. 4.11). The crystal structure transforms from amorphous to monoclinic (denoted as ZrO_2-m) and cubic (denoted as ZrO_2-c) after 400℃. The crystal size growth also corresponds with the sintering phenomena presented by Fig. 4.8 and Fig. 4.9. In contrast, calcinations under vacuum present quite different crystal structure. See Figure B.1 in appendix B. Compared to calcinations under 3% H_2/N_2, ZrO_2 calcined under vacuum are majorly composed of ZrO_2-c. The vacuum environment makes the phase-transformation temperature decrease and boosts the sintering effect while the calcinations are processing. However, as shown in Fig B.1, increasing temperature from 500℃ to 700 ℃ doesn't change crystallinity obviously which is different from calcinations under 3% H_2/N_2. This might further indicate that even though sintering might be accelerated under vacuum environment, the large intraparticle space reserved from vacuum operation could reserve more pore volume to avoid large particle sintering. The complicated mechanism for reserving large pore volume at high temperature treatment under vacuum is not discussed in detail in this research.
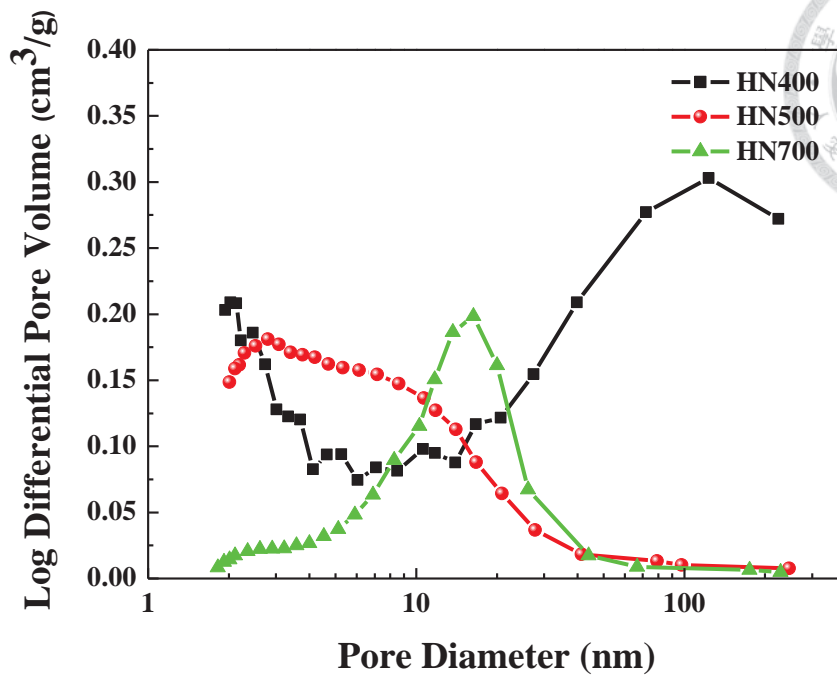
Figure 4.8 The mesopore distribution of ZrO_2(0.01M)-Dry23hr calcined under 3% H_2 in N_2. (400℃, 500℃, and 700℃)
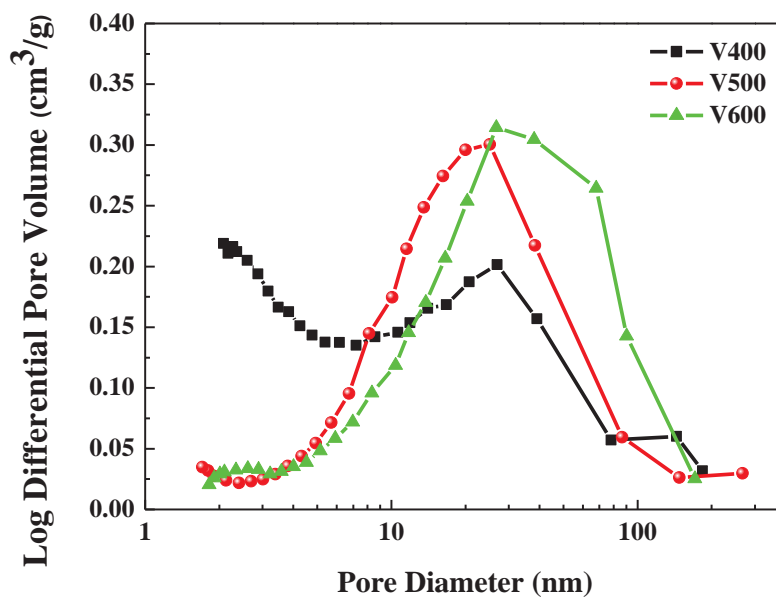
Figure 4.9 The mesopore distribution of ZrO_2(0.01M)-Dry23hr calcined under vacuum. (400℃, 500℃, and 600℃)
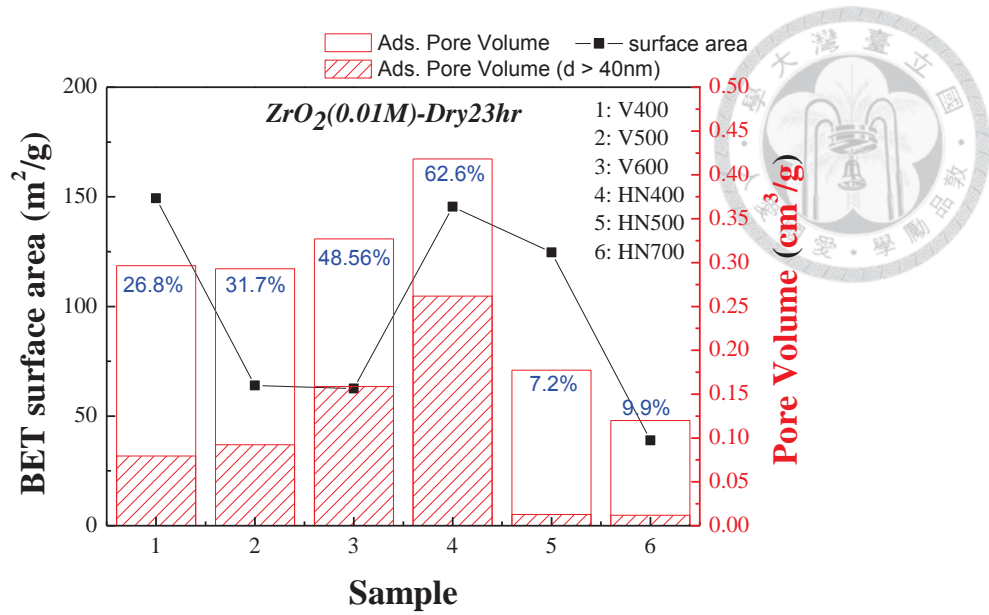
Figure 4.10 The BET surface area and pore volume of ZrO$_2$(0.01M)-Dry23hr sample under different heat treatment (Under vacuum: V400, V500, V600 ; Under 3% H$_2$/N$_2$: HN400, HN500, HN700). The numbers in columns represent values of LPR.
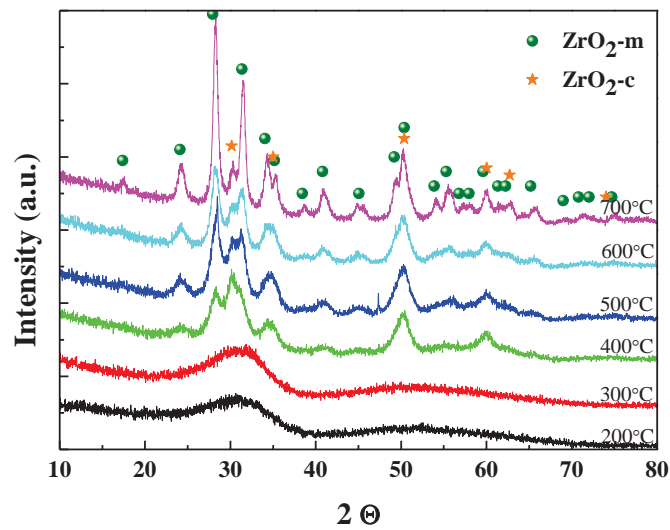
Figure 4.11 XRD figure of ZrO$_2$(0.01M) gel calcinated at different temperature under 3% H$_2$ in N$_2$.

4.3 Structural Characterization of ZrO$_2$/Si/C

4.3.1 Characterization of ZrO$_2$/Si Gel

Even though nano-Si is only physically mixed with ZrO$_2$ gel, it might somehow affect the gel formation. Thus, a detailed comparison between ZrO$_2$ gel and ZrO$_2$/Si gel is discussed in this chapter.

Relevant pictures are collected in Fig. A.4, and as presented by digital pictures, the ZrO$_2$/Si gel seems to have similar gel state and residual volume when crack formed. Thus, a sufficiently porous structure could be expected after calcinations. However, with gel volume vs. drying plot as shown in Fig. 4.12, the drying time of ZrO$_2$/Si gel is actually longer than pure ZrO$_2$ gel. Thus, the 3-D structure formation of ZrO$_2$ monomer may somehow slowed down because of existence of Si particle. Nevertheless, the moment that crack just form still can be taken as the best state of gel for calcinations since the mechanical strength of the structure mainly depends on the network of ZrO$_2$.
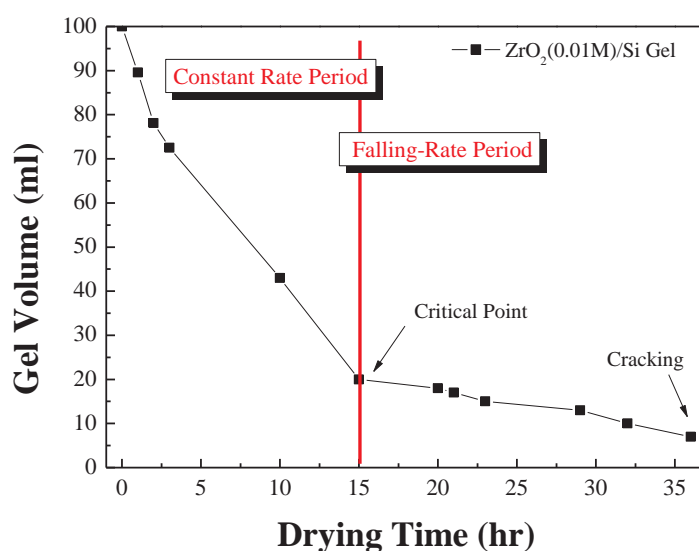
Figure 4.12 Gel volume vs. drying time plot of ZrO$_2$/Si gel. (Zr(OPr)$_4$: 0.01M)

4.3.2 Microstructural Characterization of ZrO_2/40nmSi/C

Table 4.1 lists the sample names of ZrO_2/40nmSi/C and the respective compositions. Z(0.01) indicates that the concentration of alkoxide is 0.01M; S(40) means 40nm-Si; C(F) indicates that the ZrO_2/Si dipped in 20% fructose for 1hr. C(P__%) indicates that the carbon content from pitch carbon coating after calcinations is __ %. V500 means calcination at 500℃ under vacuum. HN900 means calcinatoin in 900℃ under 3% H_2/N_2. The following S(40) would be abbreviated as S in this chapter.

XRD patterns of Z(0.01)SC(F)V500, Z(0.01)SC(F)V900, Z(0.01)SV400, and Z(0.01)SC(P15%)HN900 were presented in Fig. 4.13. The 40 nm Si encapsulated in ZSC matrix has cubic and highly crystallized structure. The existence of the coated carbon can't be obtained from the XRD pattern because of their disorder and amorphous nature. However, compared with Fig. 4.11, ZSC with carbon dissociated from fructose or pitch both show good inhibition of crystal growth of ZrO_2 which might indicate the homogeneous distribution of carbon in ZSC matrix.

The surface morphology of ZSC composites is illustrated in Fig. 4.14. From Fig. 4.14-(a) and (b), Si particles are clearly encapsulated into a ZrO_2 matrix with lots of pore which came from its porous nature or interspace between aggregated Si particles. Those pore volume was expected to buffer the expansion of Si particle during cycling test. However, the existence of carbon can't be distinguished simply by SEM image. The EDS mapping of Z(0.01)SC(F)V900 is displayed in Figure 4.15, the well-dispersed red dots and green dot in Fig. 4.15-(b) and Fig. 4.15-(c) indicated that Si and ZrO_2 were homogeneously distributed in ZSC matrix.

Fig. 4.14-(c) and Fig. 4.14-(d) show the difference before and after pitch coating for Z(0.01)SV400 sample. The fuzzy image in 4.14-(c) reflects the poor conductivity

and amorphous structure of ZrO_2 matrix. Fig. 4.14-(d) gives a structure similar to Fig.4.14-(a) and (b), but probably with less pore which can be further examined by mesopore distribution. Compared between Fig. 4.14- (c) and Fig. 4.14-(d), it's clearly that with pitch coating and higher temperature treatment, the conductivity of ZSC matrix was improved and ZrO_2 shrank to form a compact structure with many Si particle stuck with each other.

The mesopore distribution (Fig. 4.16) reflects the variation of pore structure under different operations. From Fig. 4.16-(a), the fact that pore volume didn't reduce reflects the nature of ZrO_2 as a heat-resistant material and some small pores merged into large pores. On the other hand, pitch coating for Z(0.01)SV400 sufficiently reduce the pore volume with increasing pitch and this also indicate the dissociated carbon not only deposited on the surface but also filled the pore to form a compact structure.

Another important analysis for quality of dissociated carbon is Raman spectroscopy (See Fig. B.2). The fitting model is Gaussian distribution with 2 peaks fitting and the ratio of area usually accounts for carbon quality. The peaks locate in wave number around 1600 cm^{-1} usually represent content of ordered carbon while the peaks locate in around 1350-1400 cm^{-1} represent content of disordered carbon. The former one is denoted as G band (for graphite bonding) while the latter one is denoted as D band (for disordered carbon bonding). From Fig. B.2-(a) for ZSC(F)V500, Raman spectroscopy analysis exhibits ~ 33.9% G band and ~66.1% s D band. In contrast, from Fig. B.2-(b) for ZSC(F)V900, the G band increases to ~41.5% which indicates that higher temperature treatment could effectively increase the ordered carbon content. Fig. B.2-(c), ZSC(P15%)HN900, exhibits ~ 35.7% G band which is lower in ZSC(F)V900. However, the pitch carbon coating should have better carbon coverage than ZSC(F)V900 which is not revealed in Raman Spectroscopy.
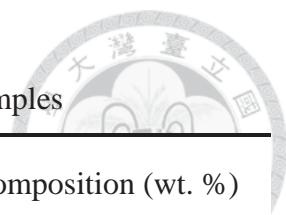
Table 4.1 Compositions of the ZS(40)C composite samples

Sample No.	Sample name	Approximate composition (wt. %)		
		Si	ZrO$_2$	Carbon
4-1	Z(0.01)S(40)C(F13%)V500	34.8	52.2	13.0
4-2	Z(0.1)S(40)C(F12%)V500	35.2	52.8	12.0
4-3	Z(0.01)S(40)C(F13%)V900	34.8	52.2	13.0
4-4	Z(0.01)S(40)C(P5%)HN900	38.0	57.0	5.0
4-5	Z(0.01)S(40)C(P10%)HN900	36.0	54.0	10.0
4-6	Z(0.01)S(40)C(P15%)HN900	34.0	51.0	15.0
4-7	Z(0.01)S(40)C(P20%)HN900	32.0	48.0	20.0
4-8	Z(0.01)S(40)C(FP18%)HN900	32.8	49.2	18.0
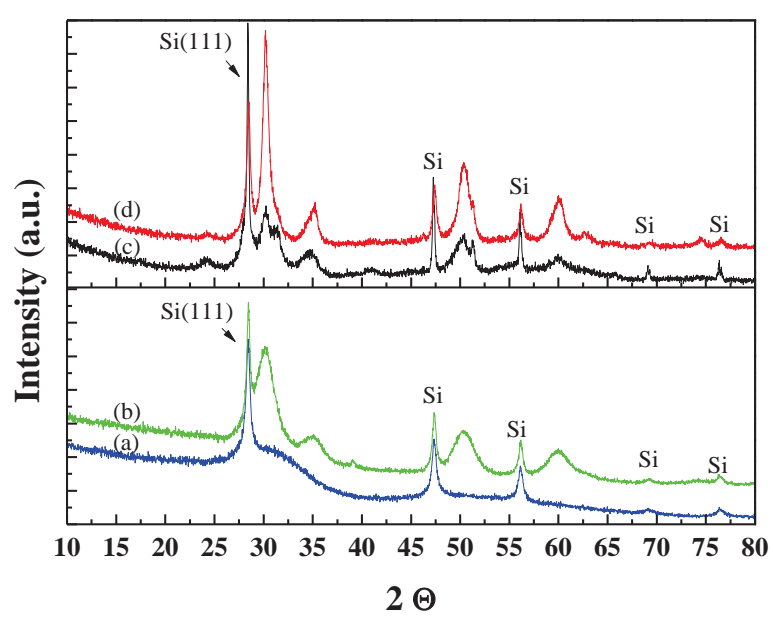
Figure 4.13 XRD patterns of (a) ZSC(F)V500, (b) ZSC(F)V900, (c) ZSV400 and (d) ZSC(P10%)HN900. (Z: 0.01M, S: 40nm)

89
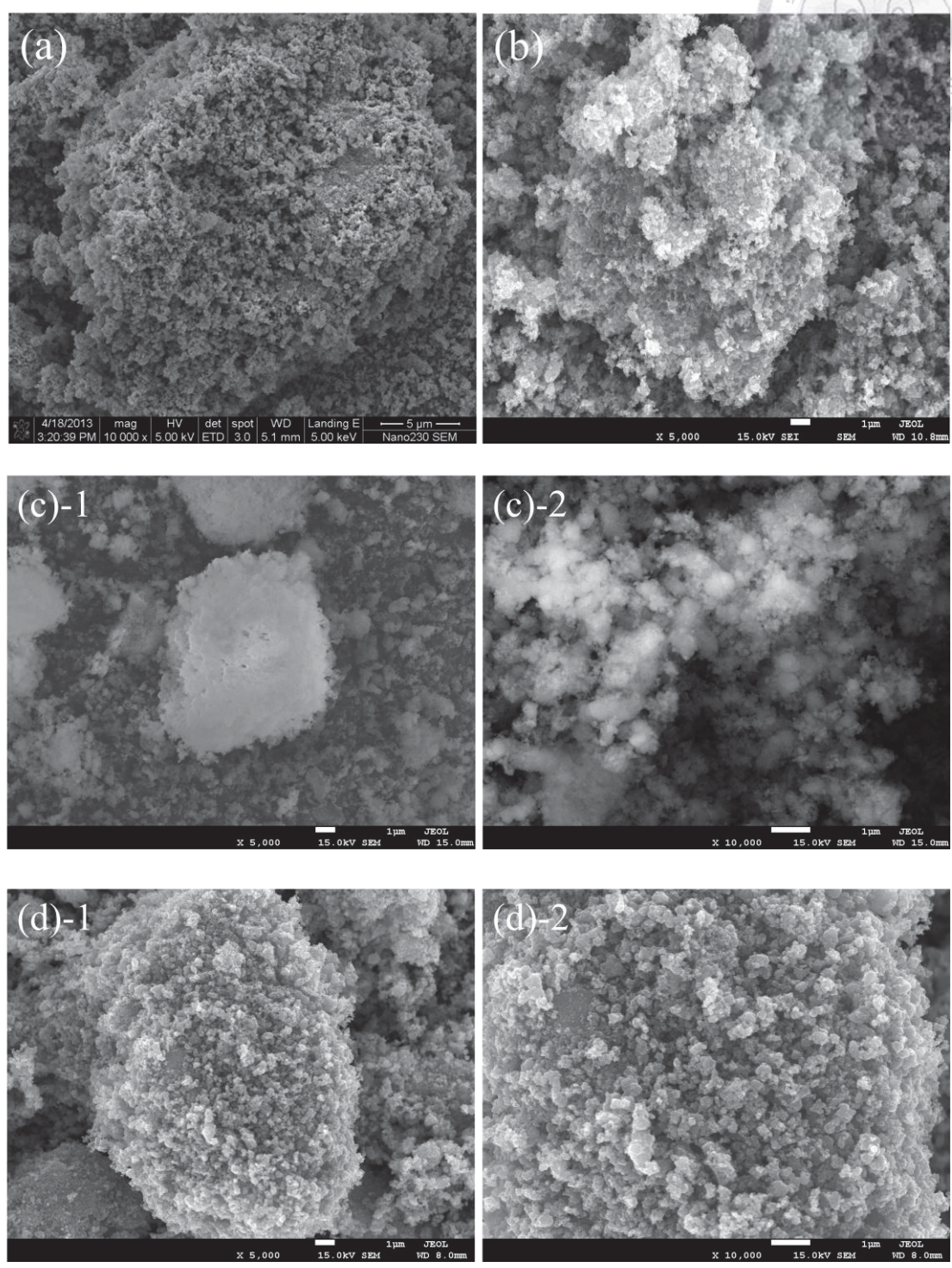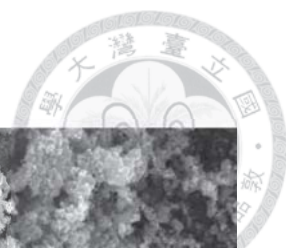
Figure 4.14 SEM image of (a) ZSC(F)V500, (b) ZSC(F)V900 (c) ZSV400, and (d) ZSC(P15%)HN900. (Z:0.01M, S:40nm)
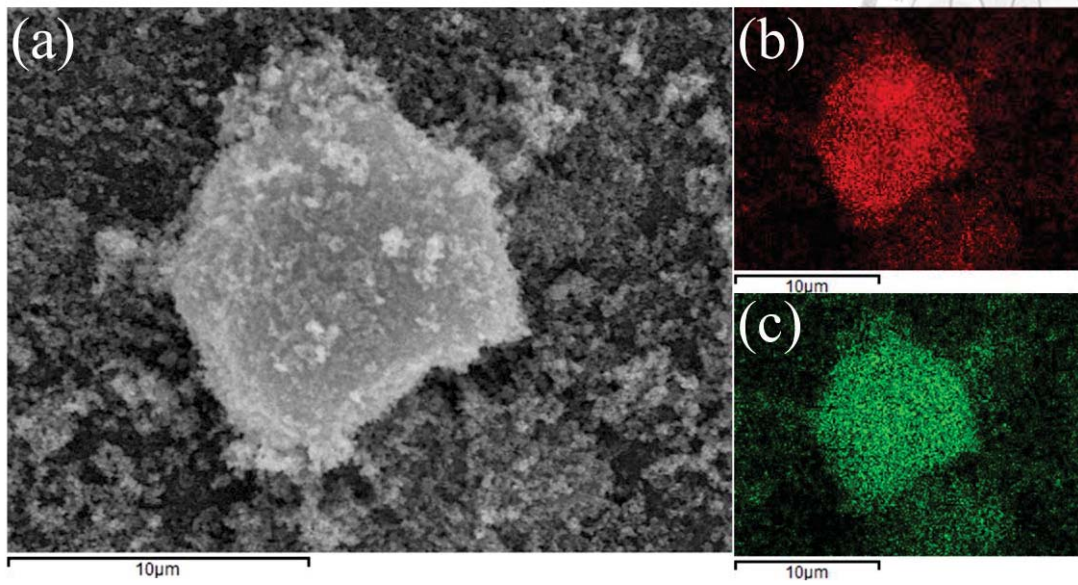
Figure 4.15 The EDS mapping of Z(0.01)S(40)C(F)V900 (a) typical image (b) red dots : Si (c) green dots : Zr.
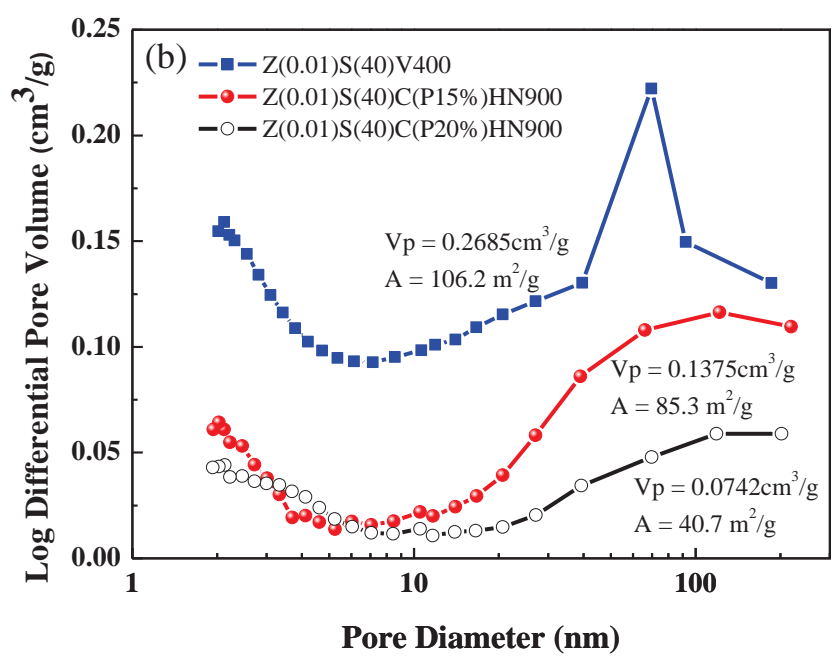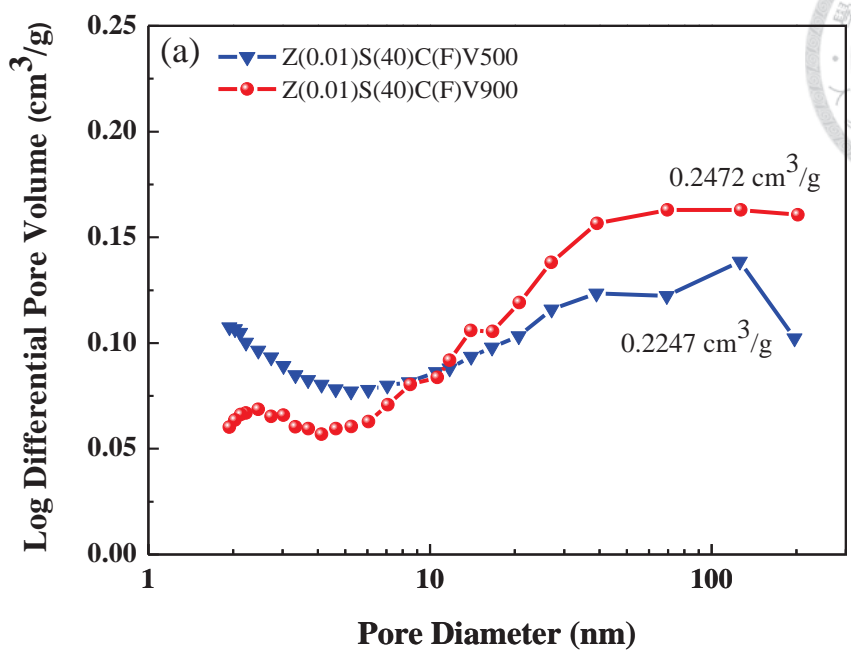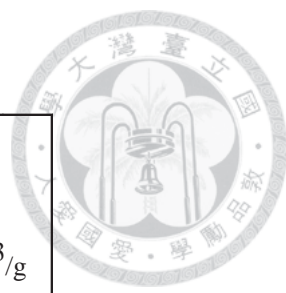
Figure 4.16 The mesopore distribution of (a) ZSC(F) with different calcination temperature 500℃ and 600℃ under vacuum (b) ZSV400 : before coating pitch ; ZSC(P15%)HN900 and ZSC(P20%)HN900 : after coating with different amount of pitch. (Z:0.01M, S:40nm)

4.4 Summary

The factors for deriving porous ZrO_2 consists of low concentration of precursor, appropriate gel condition controlled by drying time, and proper calcination strategy (i.e. temperature and atmosphere). Especially a novel idea, calcining in vacuum was proved that can effectively retains the pore volume of zircornia powder even under higher temperature calcinations. Based on these preliminary works, inducing ZrO_2 gel formation in a well-dispersed Si solution to distribute Si in the gel homogeneously can leave sufficient pore volume which is expected to be the buffer volume for Si during cycling.

The effect of carbon coating or heat treatment for deriving ZSC composite was discussed in this chapter. For ZS(40)C(F) matrix, higher temperature (from 500 to 900℃) treatment showed less effect on pore volume variation by some small pores merging to form large pores. The pitch carbon coating by wet-mixing method (with acetone) successfully let pitch fulfill the pore volume and reduced the surface area, too. The further electrochemical performance of different amount of pitch carbon coating would be presented in next chapter.

Besides, the tap densities of different composites were illustrated in Fig. 4.17. The result has shown that compared to 40 nm Si ($0.079cm^3$/g), the Z(0.01)SC(F)V500 ($0.431cm^3$/g) composite has 4 times large tap density which can be a fantastic property for increasing volume-based capacity of Si-based electrode. The overall electrode density would depend on the compression ratio, solid to water ratio of slurry, binder property and tap density of active materials. However, the tap density of Z(0.01)SC(F) is larger than Z(0.1)SC(F) which opposite our common sense that more porous matrix should have lower density. The issue has been clarified by particle size analysis by LS230 which has shown that the average particle size of Z(0.01)SC(F) is

smaller and through this fact can the power pack with each other more compactly. (See Fig. 4.18)
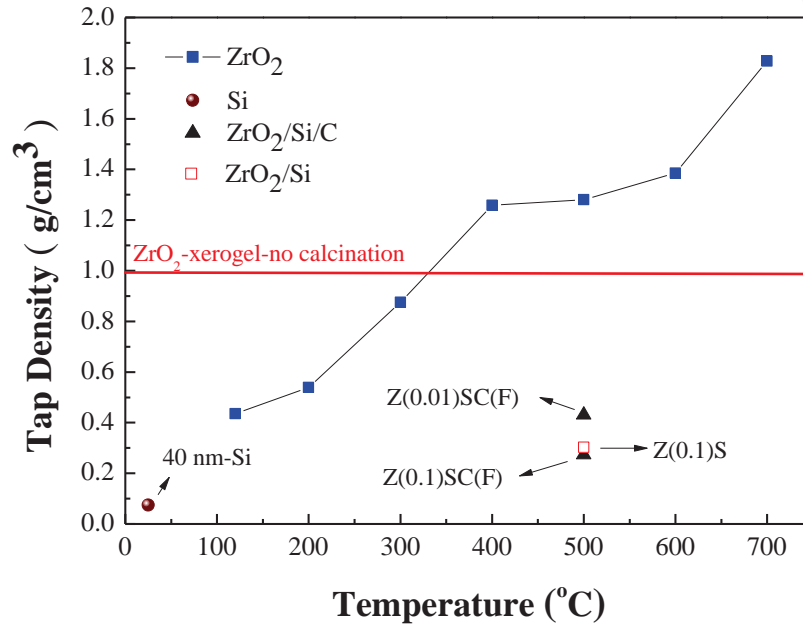
Figure 4.17 The tap density of each sample with different temperature treatment.
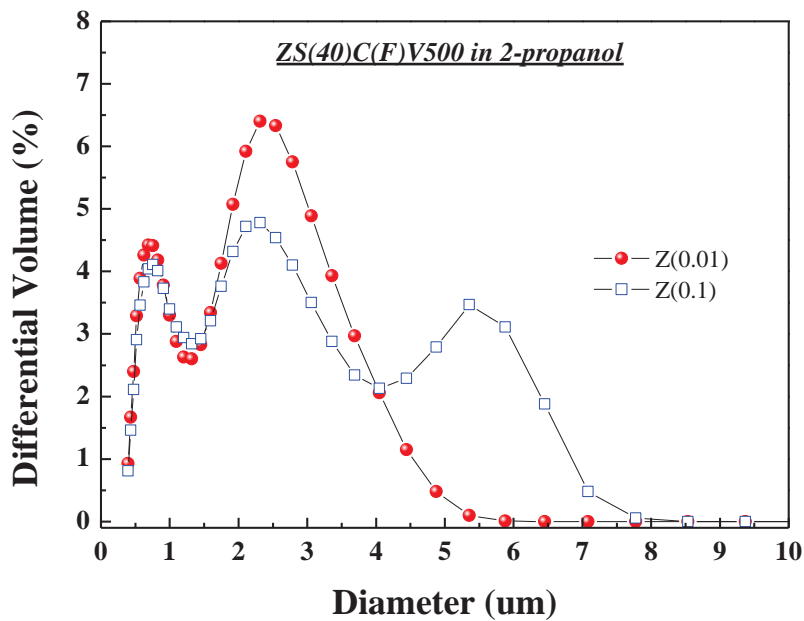
Figure 4.18 Pore size distribution of ZS(40)C(F)V500 in 2-propanol analyzed by LS230. (The particle was firstly ground and sieved with 400-mesh sieve)

94

Chapter 5 Electrochemical Characterization of

ZrO_2/Si/C

5.1 Introduction

ZrO_2/Si/C composite should have similar performance as Si/C did since it's been already known that ZrO_2 is electrochemically inactive toward lithium [62]. Therefore, several previous studies about electrochemical performance of Si/C composite are of the same importance, too [65-68].

Chapter 5.2 will present the electrochemical performance of different nano Si with alginate or SCMC/SBR as binders. The original motive of using different Si (i.e. 40nm Si and 100nm Si) as the silicon source is for discussing the relation between particle size and buffering space. However, results in chapter 5.2 would give different electrochemical performance of 40nm Si and 100nm Si, which should not only attribute to its size effect but also depends a lot on its intrinsic property, for example, different thickness of outer oxide layer. Thus, ZrO_2/40nmSi/C and ZrO_2/100nmSi/C would be discussed separately in chapter 5.3 and chapter 5.4, and the final comparison would be delivered in chapter 6.

5.2 Comparison of Different nano Si

40nm Si means its APS (i.e. average particle size) is around 40 nm. However, the nano-sized particle usually suffers from a serious aggregation problem due to its loss of exposed surface area which is thermodynamically favored. The aggregation problem is unavoidable but can somehow be controlled to certain degree by dispersing in different solvent. For example, Fig. 5.1 indicated that compared to dispersing in ethanol, the aggregation problem of nano Si is less severe in 2-pranol (The particle size was detected by LS230 with static scattering method). That's also an important factor for using 2-propanol as the solvent in this sol-gel process rather than other solvent. The complementary image is shown in Fig. A.4.

From Fig. 5.2, obviously the 40 nm Si gave better cycling performance than 100nm Si did (electrode composition are both the same as ZSC electrodes). The 1st discharge capacity of 100nm Si is only 3063 mAh/g which is ~650 mAh/g less than 40nm Si, 3721mAh/g. The capacity difference should be attributed to its high impedance which is shown in Fig. 5.3. The high impedance might result from its different oxide layer thickness and cystallinity which might impose a huge resistance of charge transfer or a limitation on Li diffusion. However, the purity of two kinds are undoubtedly almost the same since they finally gave around 400 mAh/g which was attributed by amorphous silicon structure [54].

The 1st cycle coulombic efficiency of 100nm is only 64.2% which is much less than 80.3%, thus, the 100nm Si performed less capacity in the first few cycles. For better comparison of electrochemical performance, the "normalized" charge/discharge performance plots are presented in Fig. 5.4. In the 1st cycle (Fig.5.4-(a)), they gave a relatively flat plateau during discharging and it indicates the possible two-phase

reaction [54]. During 1st cycle charge, 40nm Si electrode actually gave several plateaus, 0.28, 0.37, and 0.51V which correspond with our previous studies [38]. However, the corresponding reaction plateaus are not similar in 100nm Si, even for the 2nd cycle in Fig.5.4-(b). But the interesting point is that at the 3rd cycle, both two electrodes suffered from increasing density (i.e. increased from 0.05C to 0.20C, and the C-rate is calculated from the 1st cycle charge capacity) and they gave similar profile. Combined with fact that the profiles of 100nm Si for the first 3 cycles are almost the same, and 40nm Si performed similar profile while it suffered higher current density, we can make a conclusion that 100nm Si indeed have a higher resistance which might affect the depth of lithiation process.

Electrochemical impedance spectroscopy (EIS) analyses in Fig. 5.3 show more instinct comparison. In general, this Nyquist plot can be separated into three parts which indicate different impedance composition. First, the x-intercept of each plot usually indicates the ohmic resistance of the overall cell. Then, the middle semi-sphere might refer to charge transfer from different sources. Based on previous studies [48,54,73], the semicircle located on high-f range corresponds to impedance caused by SEI formation and the semi-circle located on medium-f range corresponds to charge transfer of the electrode. The inclined line which is located in low-f range usually represents the diffusion-controlled resistivity, but it is seldom discussed in lithium ion batteries. From Fig. 5.3, the 40nm Si presents a much smaller semicircle than 100nm Si in high-f range. In addition, the charge transfer parts of impedance which should perform in medium-f can be hardly observed for 40nm while 100nm performed a huge semicircle which might indicate a huge resistance of Li^+ charge transfer. Fig. 5.5 gives the cross-sectional figures of electrodes at fresh state and after 2 cycles. The expansion of electrodes reflects the huge expansion of Si particles and SEI formation.
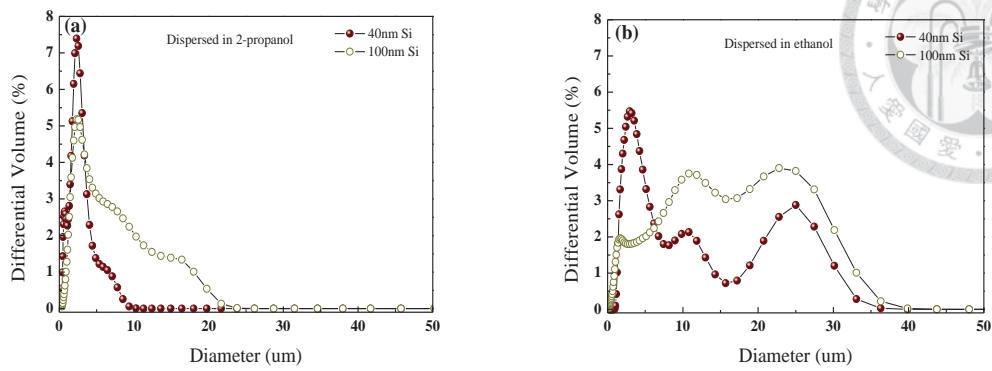
Figure 5.1 The particle size distribution of nano Si (a) Nano Si dispersed in 2-propanol

(b) Nano Si dispersed in ethanol (Analyzed by LS230).
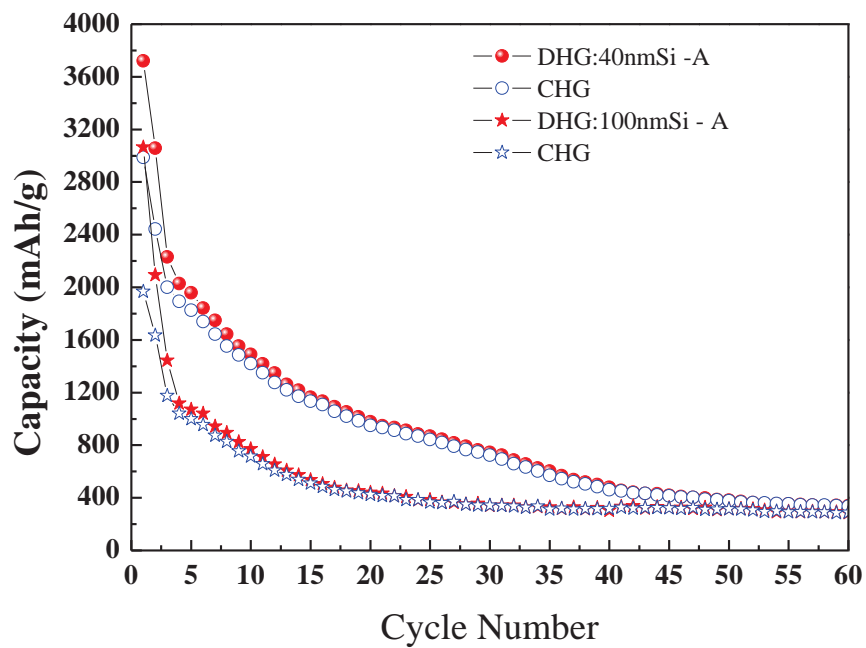
Figure 5.2 Capacity vs. cycle number plots of 40nm and 100nm Si (A: alginate).
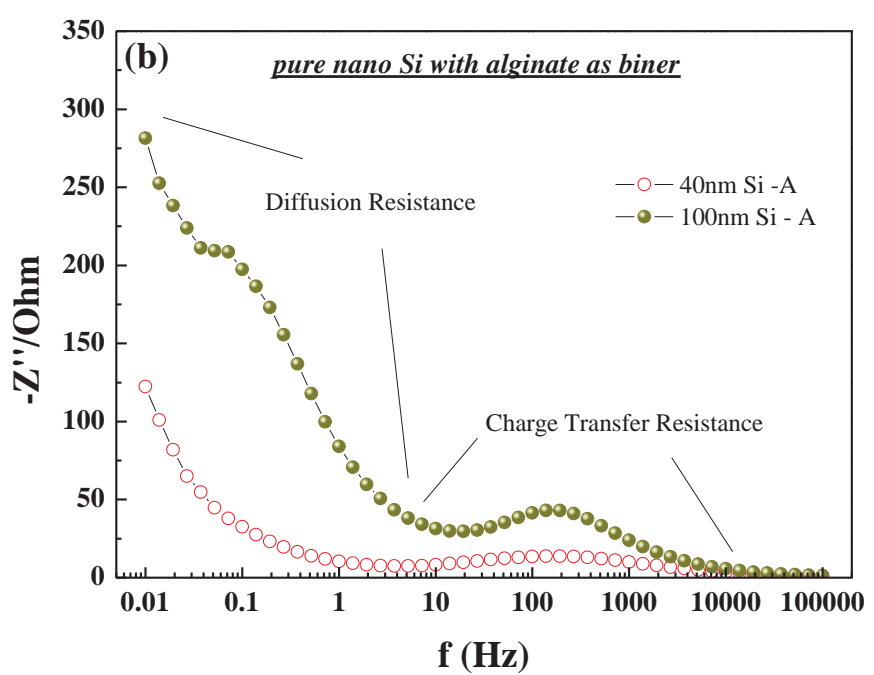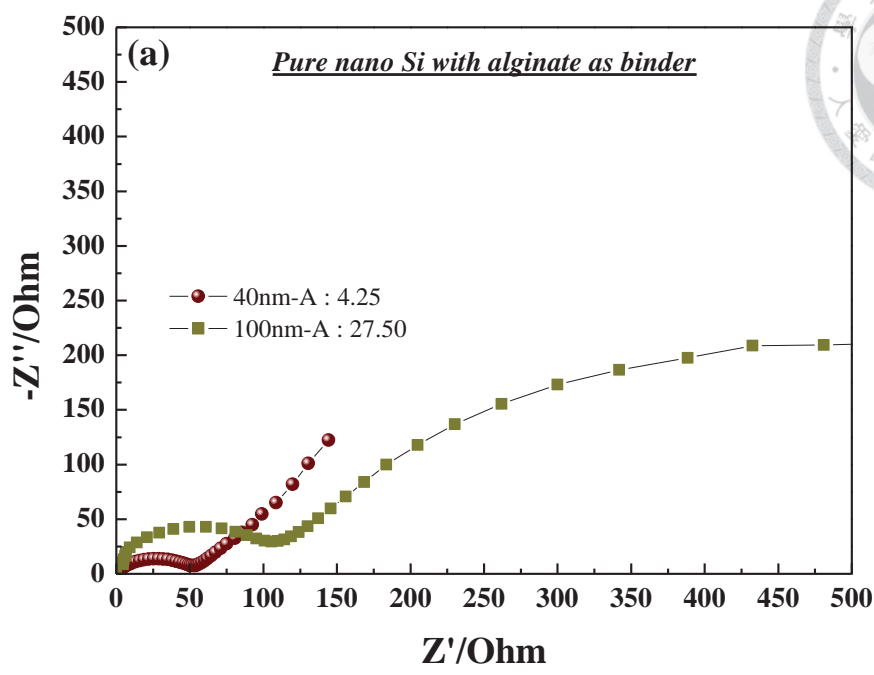
Figure 5.3 EIS spectra of 40nm and 100nm Si after 2 cycles (A: alginate). (a) Nyquist

Plot and the number in the legend indicates original x-axis intercept before shifting

figure to x=0 (b) Bode Plot with frequency between 0.01 Hz to 100,000 Hz.
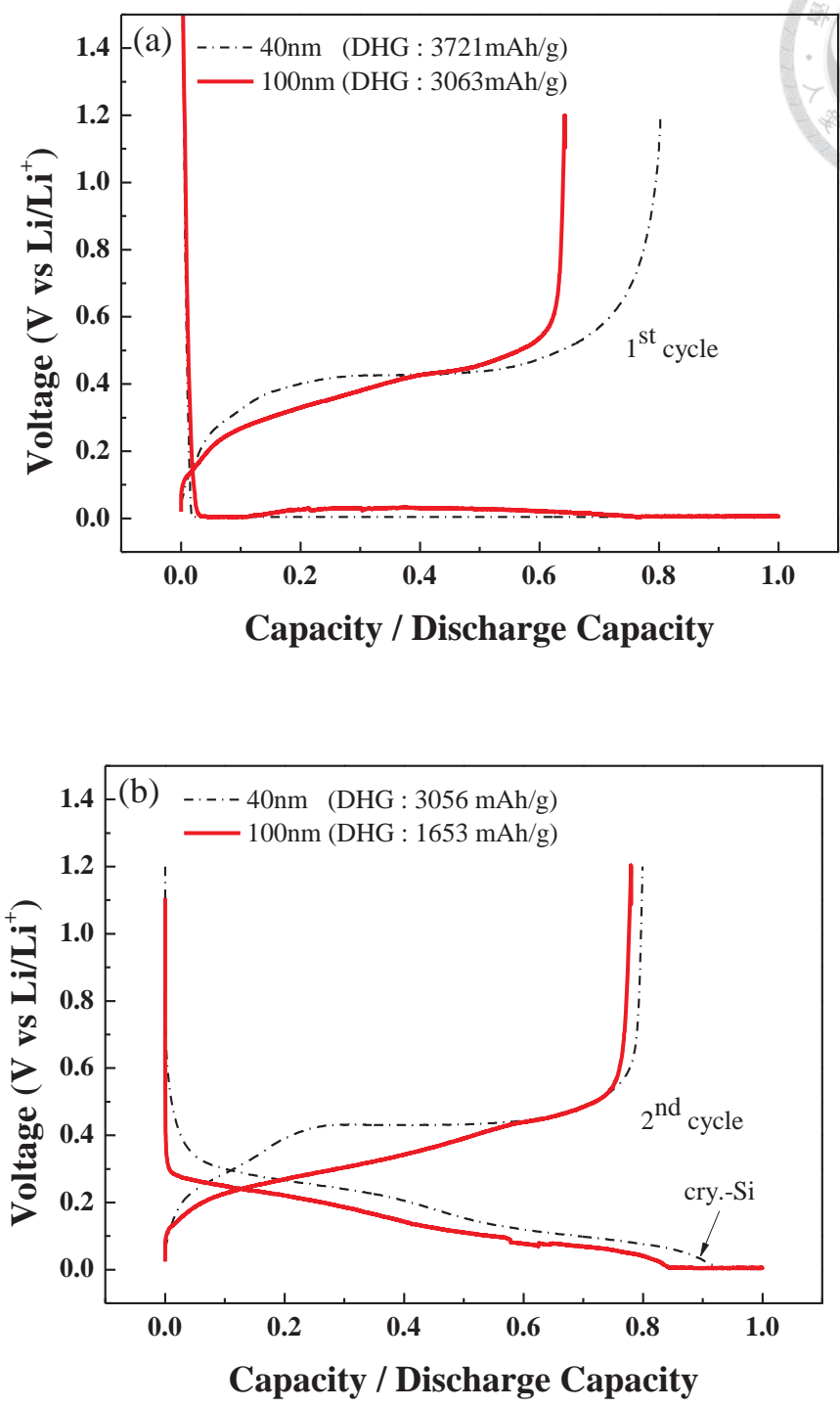
Figure 5.4 The voltage vs. normalized capacity plots of 40nm-Alginate and 100nm-Alginate: (a) The 1st cycle (b) The 2nd cycle (c) The 3rd cycle
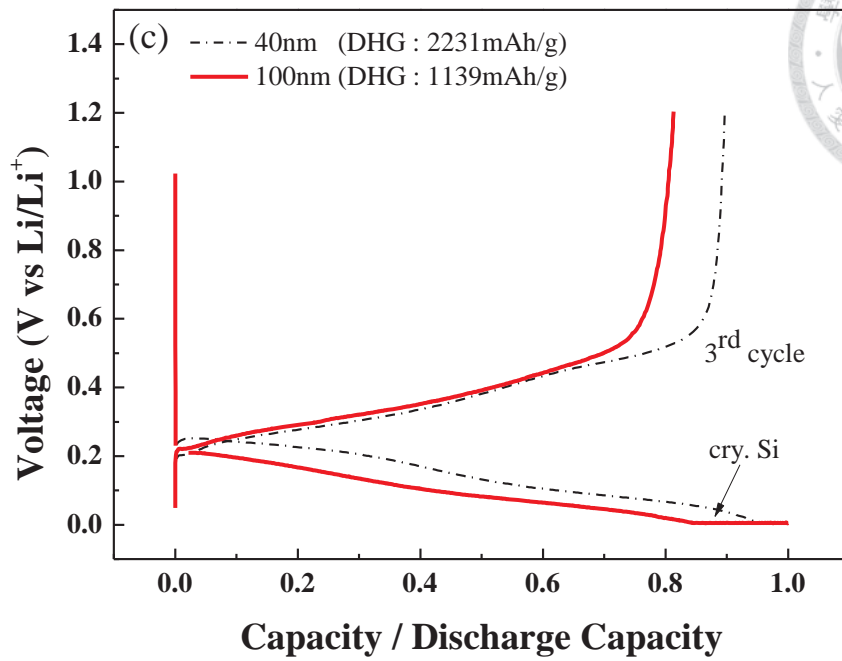
Figure 5.4-continued The voltage vs. normalized capacity plots of 40nm-Alginate and 100nm-Alginate: (c) The 3rd cycle.
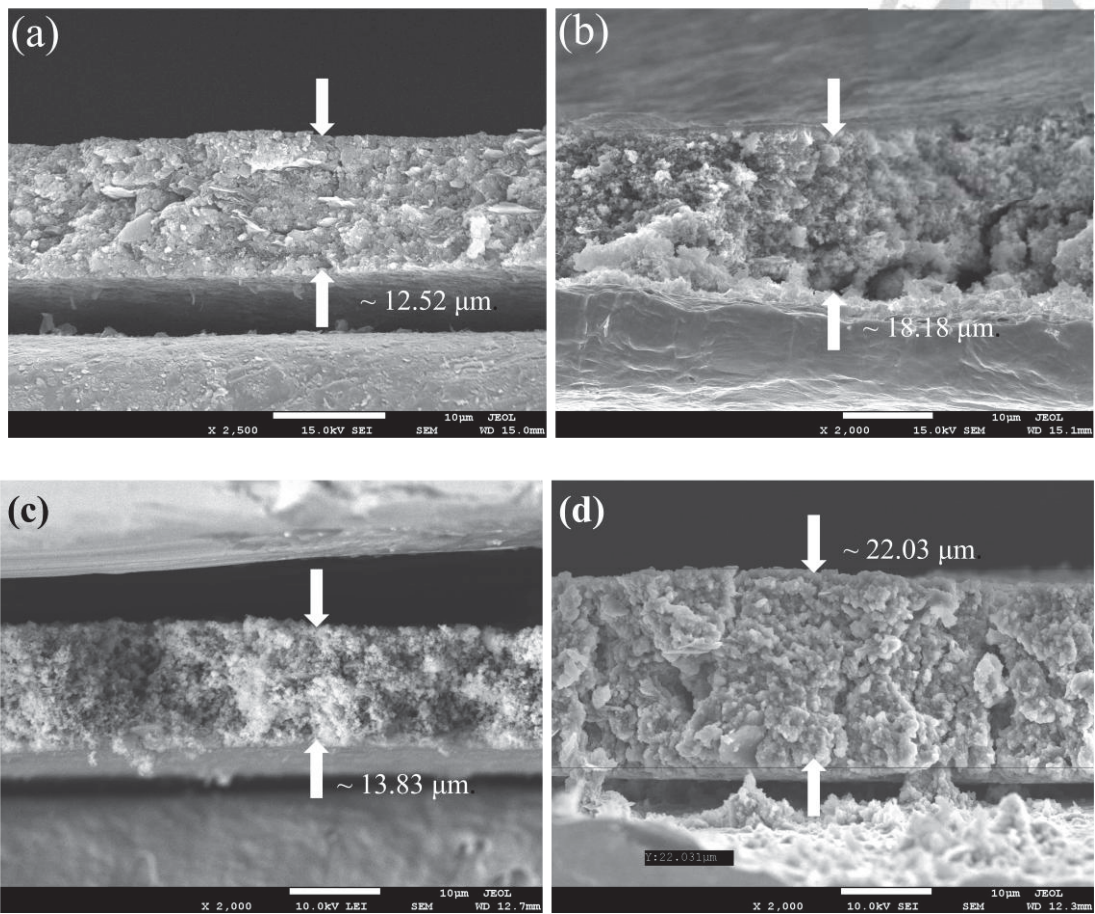
Figure 5.5 Cross-section SEM image of (a) 40nmSi-S fresh, (b) 40nmSi-S 2cycles, (c) 40nmSi-A fresh, and (d) 40nm 2cycles. (S: SCMC/SBR, A: alginate)

5.3 Electrochemical Characterization of ZrO$_2$/40nmSi/C

This chapter delivers electrochemical performances of ZrO$_2$/40nmSi/C composites. The experiments were separated into different topics to optimize the electrochemical performance step by step. First, the effect of binder on ZrO$_2$/40nmSi/C is discussed in chapter 5.3.1. Second, the importance of porosity of ZrO$_2$/40nmSi/C matrix is discussed in chapter 5.3.2. Third, the different calcination temperature is discussed in chapter 5.3.3. These three topics focus on ZrO$_2$/40nmSi/C(F) which used fructose as carbon sources. However, in order to resolve the over-lithiation problem that resulted from high surface area, pitch coating is conducted as illustrated in Fig. 3.5. The effect of different amount of pitch coating is discussed in chapter 5.3.4. Finally, in chapter 5.3.5, combination of fructose and pitch coating is introduced and compares with the former samples.

5.3.1 Different Binder : Alginate vs. SCMC/SBR

As introduced in previous literature review [50, 51], binder plays an important role in electrochemical performance for lithium ion batteries. A brand-new binder, alginate, drew lots of attention due to its fascinating improvement on the cycle life of silicon materials. Therefore, SCMC+SBR (weight ratio 1:1) and Alginate were adopted as binders in this chapter for ZSC(F)V500 to see the differences. ZSC-A denotes Z(0.01)S(40)C(F)V500 with alginate and ZSC-S denotes Z(0.01)S(40)C(F)V500 with SCMC/SBR.

From Fig. 5.6 where capacity vs. cycle number plot is presented, obviously ZSC-A shows better capacity retention than ZSC-S. Besides, based on Fig. 5.2, 40nm Si can provide around 3720mAh/g capacity at the 1st lithiation process and thus, our ZSC should provide 3720×34.8%=1310 mAh/g (34.8% from Table 5.1). The 1st cycle discharge capacities of ZSC-S, 1492 mAh/g and ZSC-A, 1442mAh/g, are both larger than theoretical capacity calculation which can reflect the core-shell reaction mechanism of Si anode [54] and SEI formation. The better capacity retention of ZSC-A might come from several reasons and one of them is that for ZSC composite, there should still be parts of nano-Si without proper coverage of ZrO_2 matrix and alginate as binder can appropriately enhance its electrochemical performance.

A comparison of the first three cycle profiles of ZSC-A and ZSC-S samples is shown in Fig. 5.7 to further discuss their differences in electrochemical performance. The potential curves for the both ZSC electrodes displays a similar 1st cycle curve which includes a low and slightly-sloping plateau around 0.1 V in the initial lithiation process corresponding to a two-phase region and lithiated amorphous Si is formed in this region [38, 42]. There is a big shoulder occurring between 0.1V and 0.8V which is mainly caused by SEI formation. From Fig. 5.7-(a), the 1st cycle irreversible

capacity contributed by SEI formation are 275mAh/g for ZSC-S and 325 mAh/g for ZSC-A which show no obvious difference. During delithiation, the voltage curves follow a sloping plateau, indicative of single phase region [54]. Compared with Fig. 5.7-(c), the 3rd cycle of ZSC composite remains distinct plateau even though the current density increased from 0.05C to 0.20C.

Fig. 5.8-(a) and Fig. 5.8-(b) show the Nyquist and Bode plots of ZSA electrode respectively. In general, the Nyquist plots of ZSC exhibit a semicircle and followed by an inclined line. The –Z'' (imaginary component of the impedance) vs. f (frequency) plot (i.e. Bode plot) of ZSC shows a peak within the f-range associated with the semicircle. Previous study [73] has demonstrated that the charge-transfer impedance for Li^+ intercalation into either graphitic or disordered C has the characteristic frequency in the range of 1-50 Hz. And anaologues to lithiation of graphite, the impedance toward the high-f end (100-100,000 Hz) may be attributed to the SEI thin film on the Si surface, while the impedance within the intermediate f region (10-10,000Hz) is due to the charge transfer (CT). Therefore, Fig. 5.8 indicates that the main impedance of ZSC came from CT, or in other words, the impedance from SEI film is rather small compared to the impedance from CT. Fig. 5.9 gives the top-view SEM image of ZSC-A and ZSC-S electrode after 2 cycles. The grown SEI displayed quite-different morphology. The grown SEI of ZSC-S (From Fig. 5.9-(a) to Fig.5.9-(b)) seems thicker than ZSC-A. The top-view of ZSC-S after 2 cycles can hardly find the original surface morphology but ZSC-A after 2 cycles can still remain the rough surface morphology. Therefore, a simple inference is drawn based on the SEM image that the grown SEI layer on SCMC/SBR and Alginate are different and the former one gave much dense and even thicker SEI structure. From the cross-section SEM image (Fig. 5.10), the ZSC electrodes after 2 cycles both show an increase in thickness due to the expansion of Si and SEI formation.
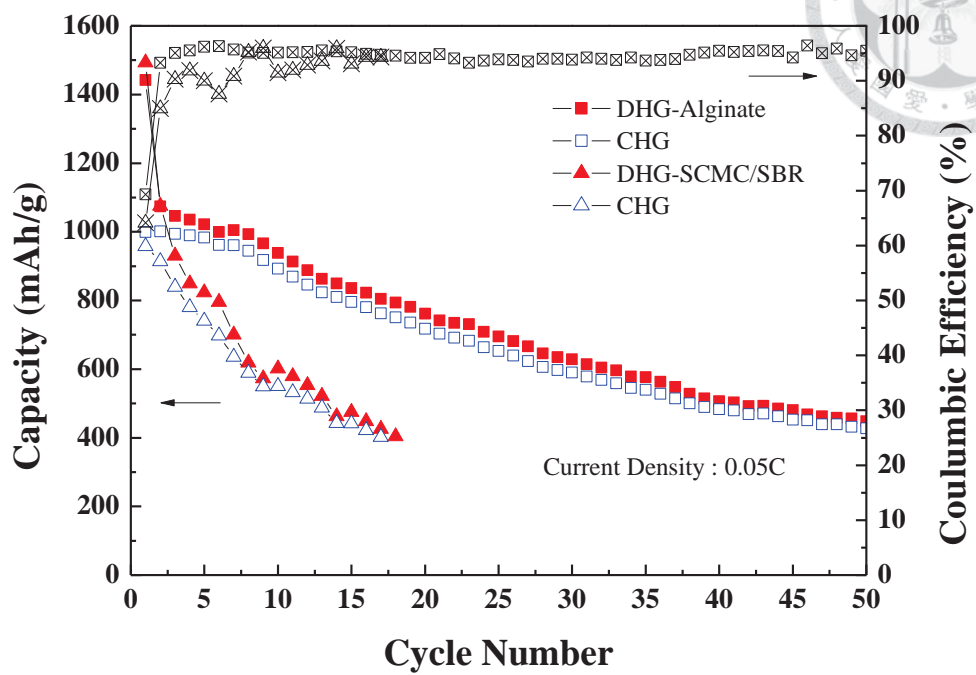
Figure 5.6 Capacity vs. cycle number plot of Z(0.01)S(40)C(F)V500 with different binders, Alginate and SCMC/SBR.
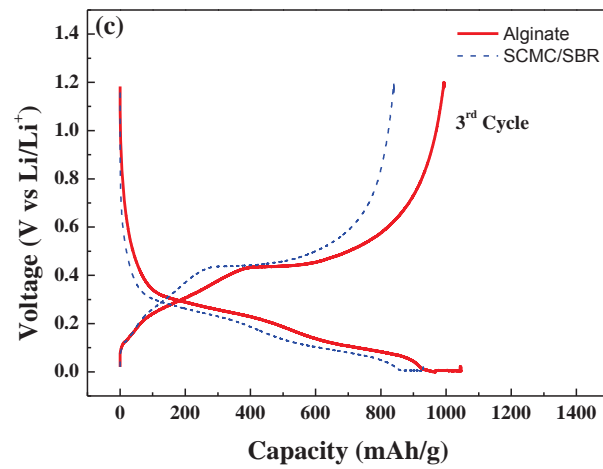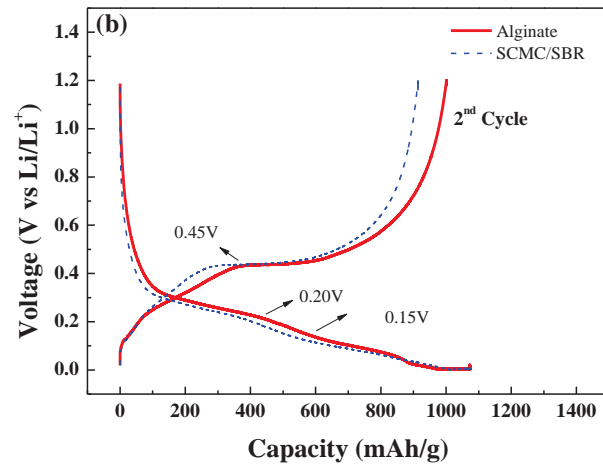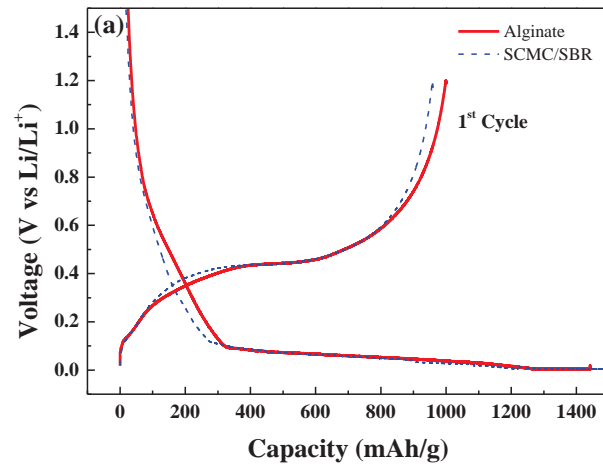
Figure 5.7 Voltage-capacity curves for Z(0.01)S(40)C(F)V500 with different binders, alginate and SCMC/SBR. (a) The 1st cycle (b) The 2nd cycle (c) The 3rd cycle
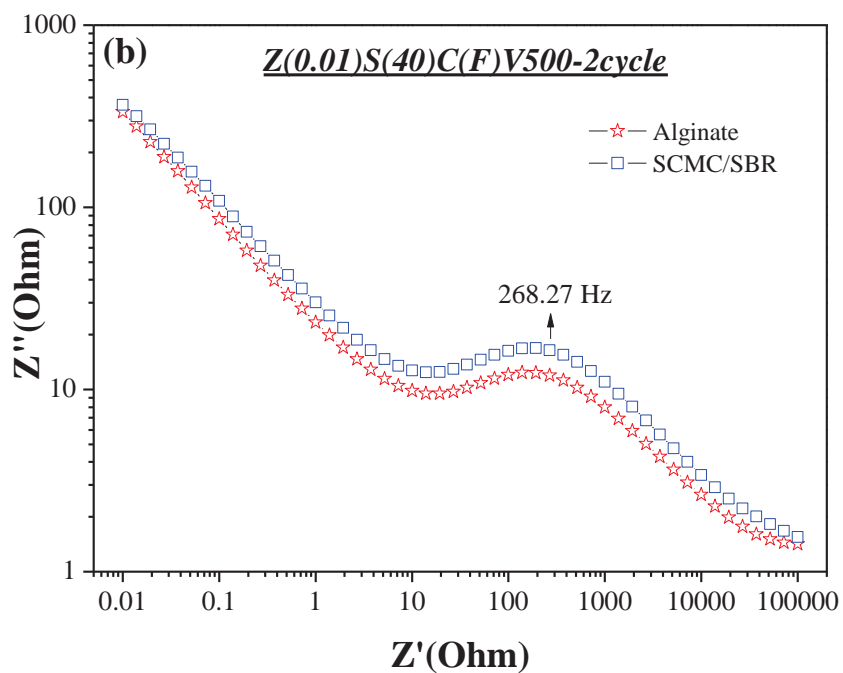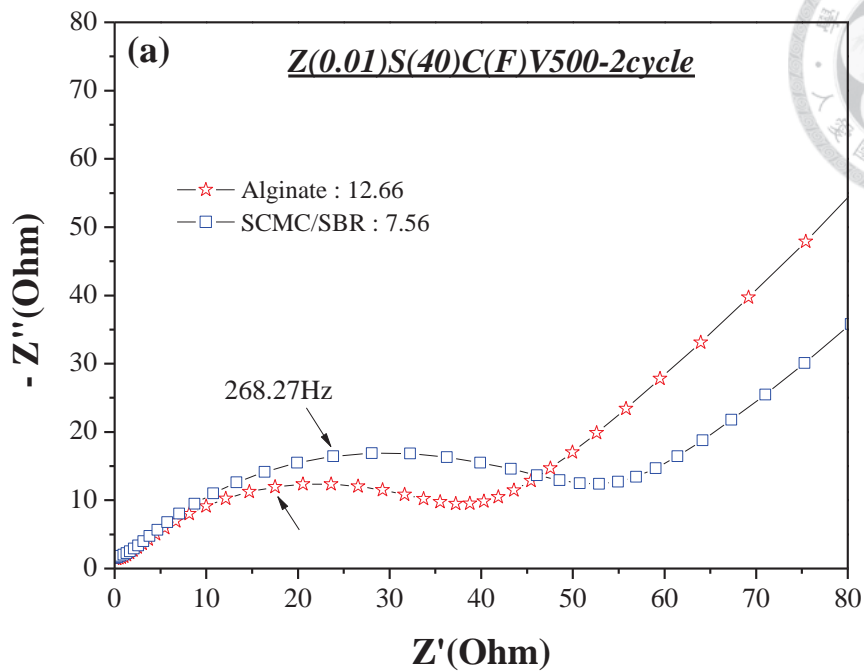
Figure 5.8 EIS spectra of Z(0.01)S(40)C(F)V500 with different binders after 2 cycles.

(a) Nyquist Plot and the number in the legend indicates original x-axis intercept before

shifting figure to x=0 (b) Bode Plot with frequency between 0.01 Hz to 100,000 Hz.
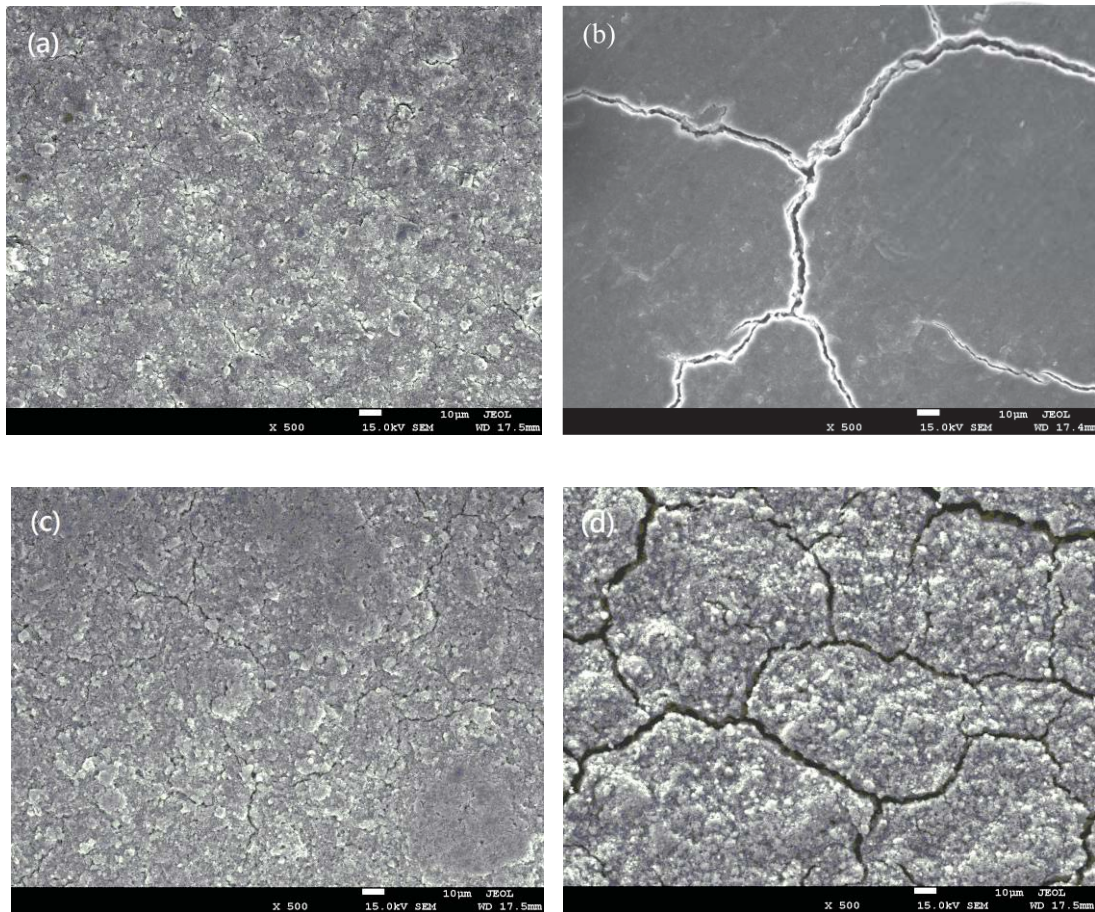
Figure 5.9 SEM image of Z(0.01)S(40)C(F)V500 with different binders from top-view.

(a) ZSC-S electrode at fresh state (b) ZSC-S electrode after 2 cycle (c) ZSC-A electrode

at fresh state (d) ZSC-A electrode after 2 cycle
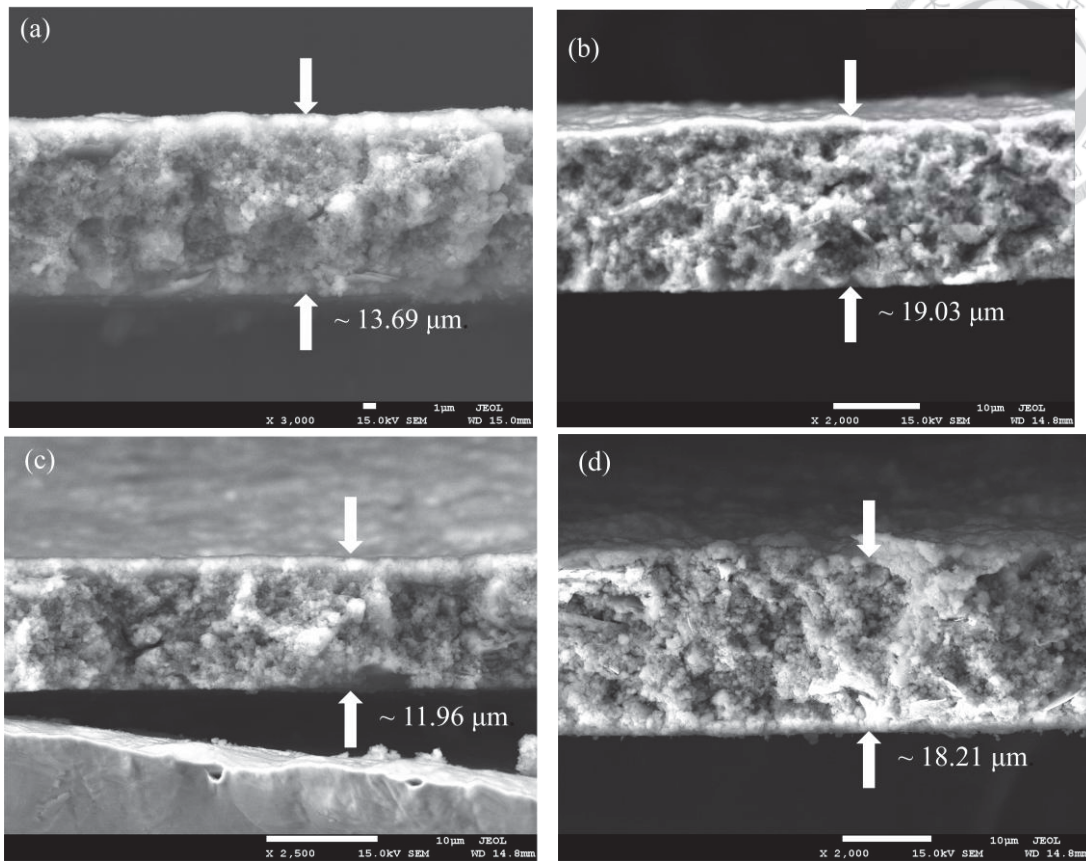
Figure 5.10 SEM image of Z(0.01)S(40)C(F)V500 with different binders from side-view. (a) ZSC-S electrode at fresh state (b) ZSC-S electrode after 2 cycle (c) ZSC-A electrode at fresh state (d) ZSC-A electrode after 2 cycle
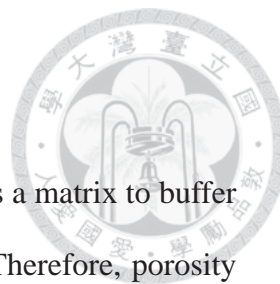
5.3.2 Effect of Porosity on ZrO$_2$/Si/C Matrix

The main purpose of this research is to produce porous ZrO$_2$ as a matrix to buffer the expansion of silicon during alloying and de-alloying process. Therefore, porosity of ZrO$_2$ is the most important factor in ZSC composite. Porosity of ZSC was controlled by different concentration of precursor in this chapter and we have derived a clear conclusion which indicate that Z(0.01)SC has rather high porosity than Z(0.1)SC in Fig. 4.16.

Cycle life comparisons are presented in Fig. 5.11-(a) and gives the absolute charge capacity vs. cycle number plot of ZS(40)C(F) samples. In order to quantify the improvement for each sample, Fig. 5.11-(b) is made to see the capacity retention ratio of each sample. A well-known fact of pure Si is that it suffers a fast capacity fading from the first few cycles which reflects the fierce irreversible expansion (See Fig. 5.2). For example, for 40nmSi-A, the 2nd cycle retention ratio left only 82% and the 3rd cycle gave only 67% when the current density increased. Therefore, buffering expansion of Si in the first few cycles is critical for improving Si materials. In Fig. 5.11-(b) Z(0.01)SC(F)-0.05C sample, which only ran under 0.05C to the end, show almost 100% retention at the 2nd cycle due to successful buffering effect and of course, suffered no obvious capacity drop at the 3rd cycle without increasing current density. However, the electrode still went into fading after the 8th cycle due to its structural collapse.

To apply to industrial application, current density for other samples is adjusted to 0.20C after 2 cycle formation of SEI. Under this charge/discharge strategy, Z(0.01)SC gave a better charge capacity retention than Z(0.1)SC not only at the 2nd cycle but also at the 3rd cycle when current density increased. The enhancement of cyclability is referred to the much more porous structure of Z(0.01)SC since other factors are

almost equal. For examples, the carbon quantity is close (from Table 5.1) and the carbon quality should also be similar because of the same calcination condition. Besides, the similar content of ZrO_2 and Si shows that the improvement of cycle life resulted from not just a simple dilution of Si but the effective buffering structure. On the other hand, a highly porous matrix can offer sufficient pore volume to accommodate the expansion of Si and even more, prevent nano size Si from severe aggregation which also guarantees its better cycle life performance.

One interesting discover for capacity retention ratio vs. cycle number plots of each Si sample is that they presented similar falling performance. From Fig. 5.11-(b), each plot can be vertically moved to overlap except for the first few cycles and this fact also indicates that the idea of providing porous structure as buffering matrix can effectively improve cycle life but without changing its electrochemical performance. The further improvement is discussed at next chapter.

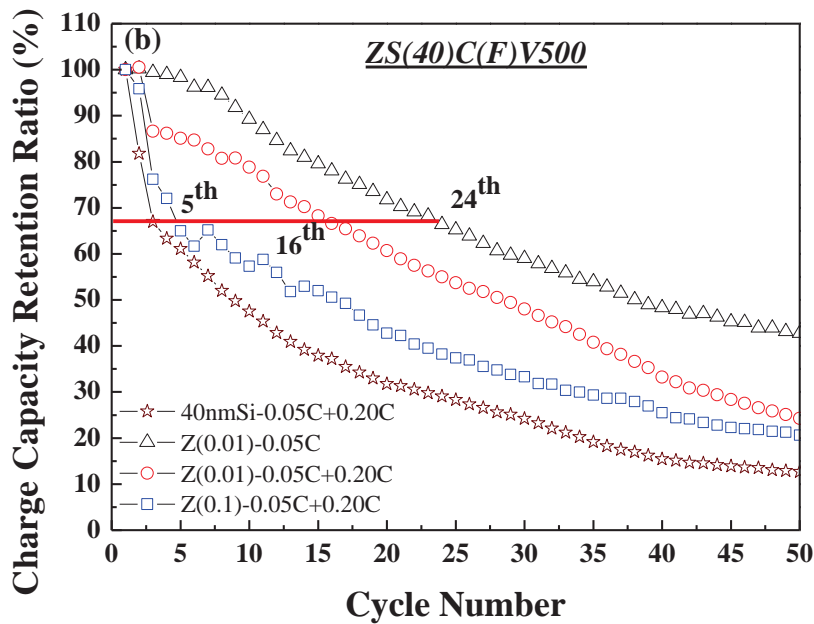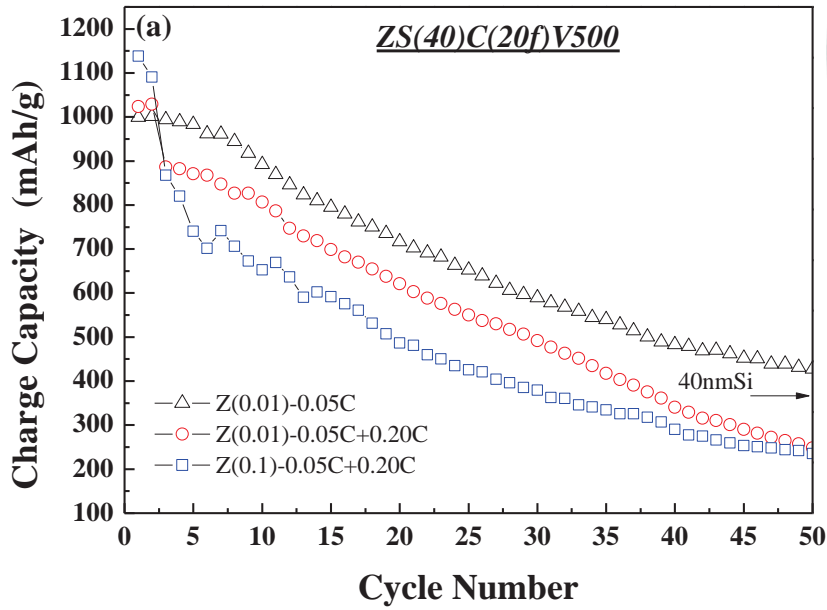**Figure 5.11** The cycle life plot – (a) Charge capacity of Z(0.01)SC(F)V500 and Z(0.1)SC(F)V500 (b) Charge capacity retention ratio of 40nmSi-A, Z(0.01)SC(F)V500 and Z(0.1)SC(F)V500. (0.05C represents that the cell ran to the end with 0.05C current density, 0.05C+0.20C represents ran for first 2 cycles with 0.05C and ran with 0.20C for the following cycles ; the arrow indicates the 50th charge capacity of 40nm Si)

5.3.3 Different Calcination Temperature for ZrO2/Si/C(Fructose)

As presented in chapter 4.3, the higher temperature treatment was conducted to improve the electrochemical performance of Z(0.01)S(40)C(F). The motive came from the fact that higher temperature gives better quality of dissociated carbon. However, the possible trade-off of high-quality carbon is the reduction of pore volume due to high-temperature treatment. To our surprises, Fig. 4.16-(a), shows that higher temperature treatment for ZSC matrix would make small pores merge into large pore and hardly change overall pore volume. Thus, the buffering effect of ZSC may remain the same or even better due to larger LPR.

From Fig. 5.12-(a), a voltage vs. lithation capacity plot is drawn to illustrate the actual state of Si corresponding to the amount of Li^+ which has lithiated into Si. An ideal electrode should have a close loop, representing no irreversible capacity in that cycle. Therefore, with increasing cycle, the lithiation capacity of each loop should not excess the theoretical capacity; otherwise, the excess amount of capacity would be taken as the SEI formation and structural defect of the active material which would trap the inserted lithium. For example, the disordered carbon and its left oxygen-containing groups might result in irreversible capacity [48, 49]. Note that the cycle number from left to right is 1, 2, 3, 4, 5, 10, 15, 20, 25, 30, 35, 40, 45, and 50 in sequence.

Fig. 5.12-(c) and (d) give the normalized charge/discharge curves at assigned cycles. Apparently, ZSC-V900 presents better plateau retention which reveals better cyclability by losing active material slower. Fig 5.13-(a) gives capacity and columbic efficiency of each cycle and Fig. 5.13-(b) gives capacity retention ratio which can clearly observe the enhancement of cyclability.

Based on Fig. 5.12 and 5.13, several inferences can be drawn as follows. First,

ZSC-V900 showed better cyclability due to its improved columbic efficiency with more than 1% for each cycle. Second, the overlithiation (i.e: excess accumulated irreversible capacity) should came from SEI formation on the surface area instead of carbon defect, since they have equal overlithiation amount after 50 cycles (~1700mAh/g). However, the reversible capacity of ZSC-V900 still remains 500mAh/g which is much higher than ZSC-V500 does (250mAh/g). A conclusion is made that higher temperature treatment can effectively improve the conductivity of ZSC matrix and with better conductivity, the stability of Si during cycling is enhanced.
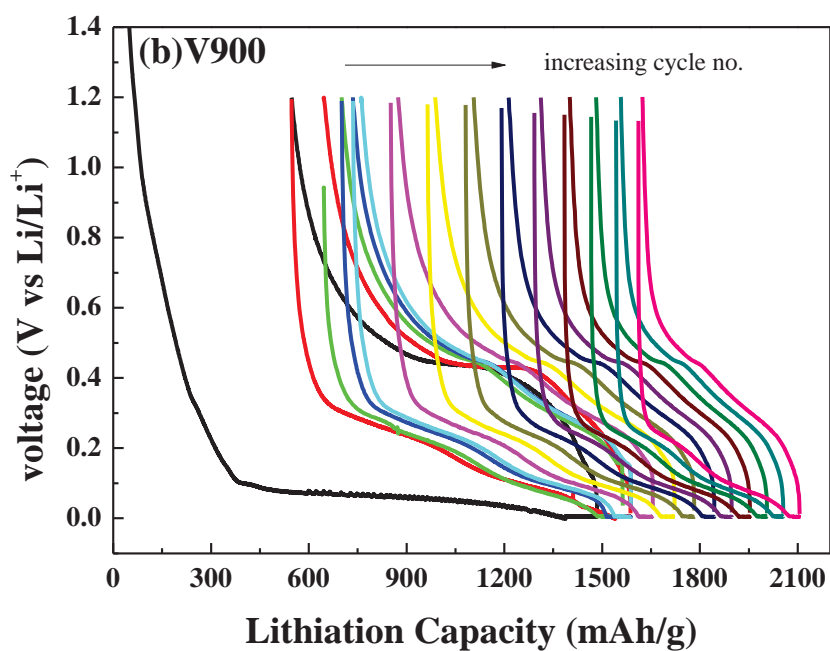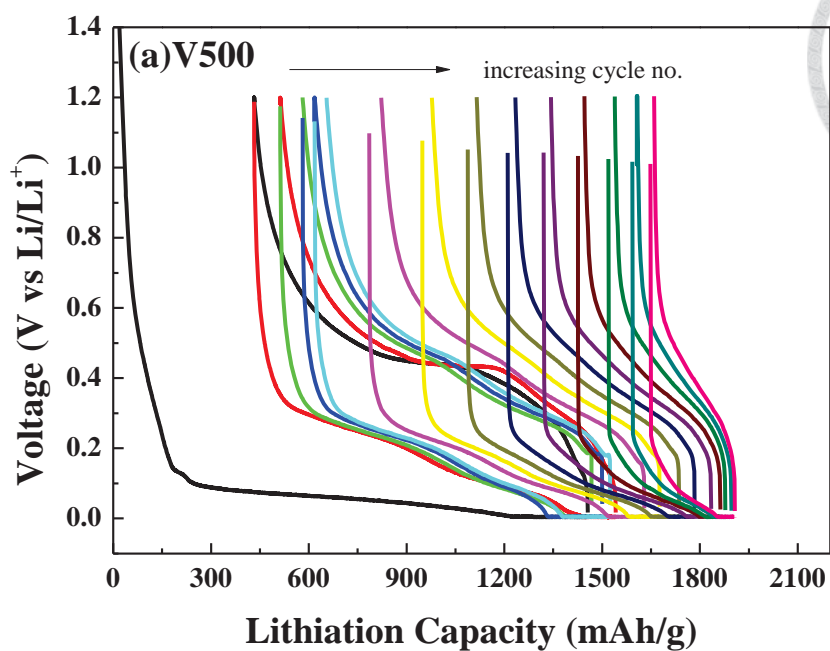
Figure 5.12 (a) The voltage vs. lithiation capacity plot of ZSC-V500 (b) The voltage vs.

lithiation capacity plot of ZSC-V900. (Z:0.01M , S:40nm, C:F)
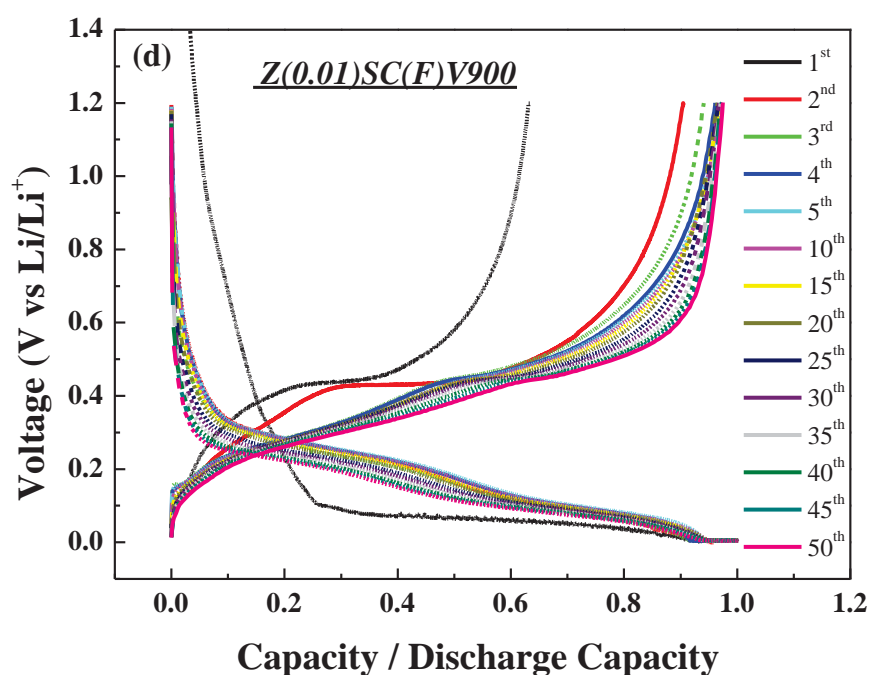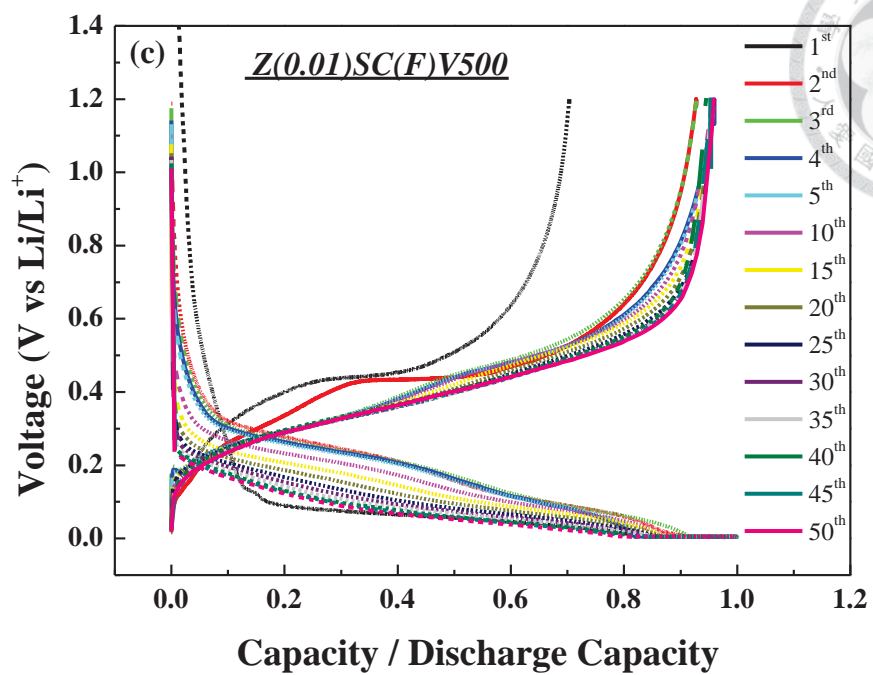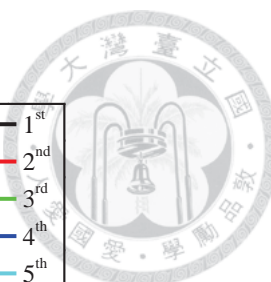
Figure 5.13-continued (c) The normalized charge/discharge curves of ZSC-V500 at assigned numbers (d) The normalized charge/discharge curves of ZSC-V500 at assigned numbers. (Z:0.01M , S:40nm, C:F)
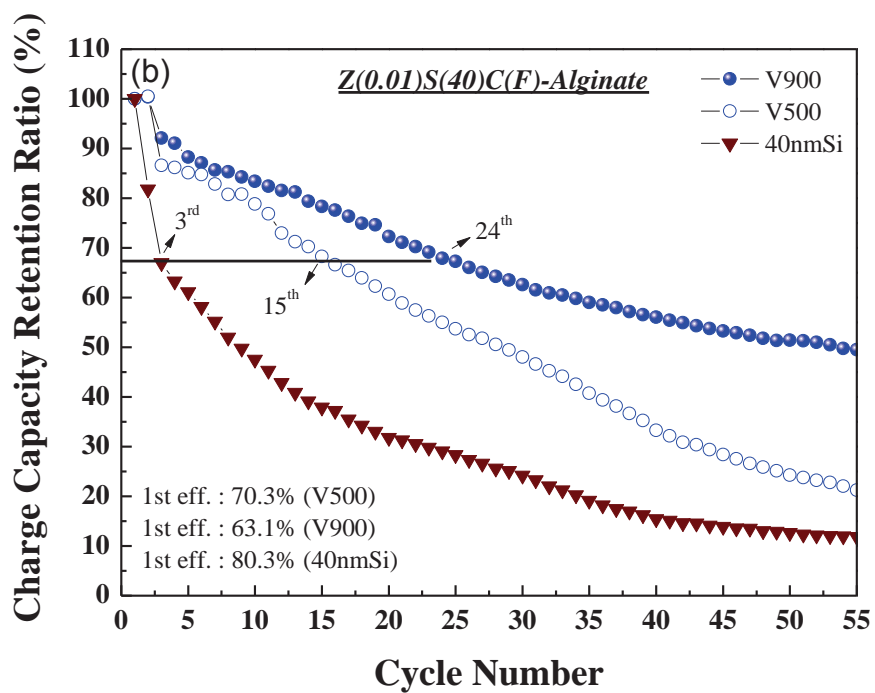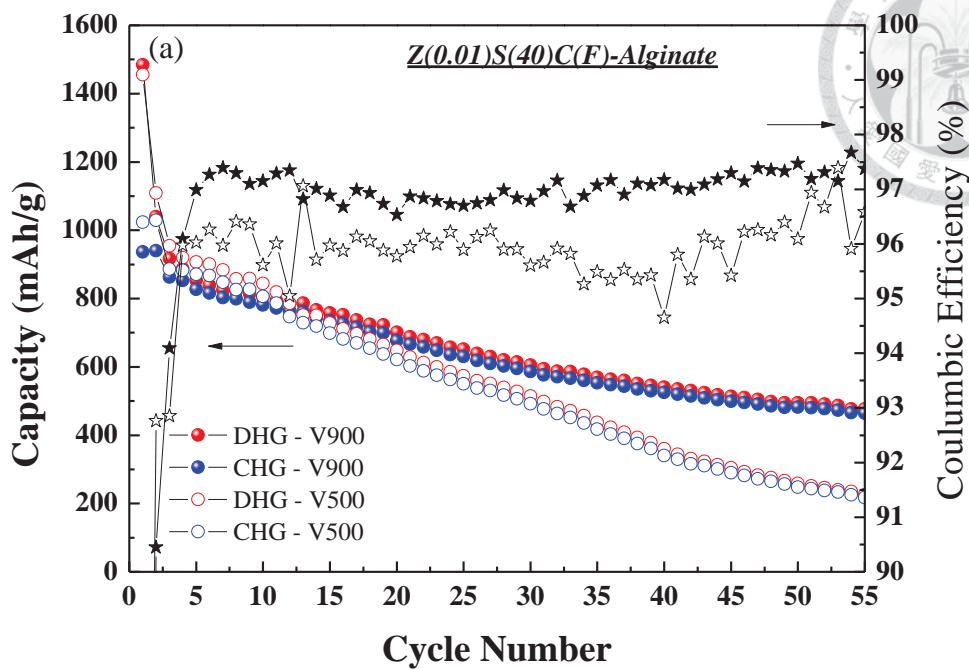
Figure 5.14 The cycle life plots. (a) Capacity and columbic efficiency of Z(0.01)S(40)C(F) calcined under vacuum with different temperature, 500℃ and 900℃ (b) Charge capacity retention ratio vs. cycle number.

5.3.4 Different carbon amount for ZrO$_2$/Si/C(Pitch)

In chapter 5.3.4, a different carbon coating method is conducted. As mentioned before, ZSC(Fructose) has ZS gel soak in fructose solution which can guarantee the a homogeneous distribution of carbon in ZSC matrix. However, a highly-porous matrix with large surface area might lead in too much overlithiation from SEI formation as presented in Fig. 5.12-(a). In order to solve the overlithiation problem, a carbon coating method with two-step calcinations was researched.

The detailed process of deriving ZSC(Pitch) is illustrated in Fig. 3.6 and the characterization shown in Fig. 4.16-(b). Apparently, pitch coating indeed reduces the pore volume of ZSC matrix by fulfilling carbon into the pores. From Fig. 5.14-(a) and (b), pitch coating amount draws a huge effect on the electrochemical performance of ZSC matrix. Instinctively, without sufficient carbon distribution, the ZSC matrix should perform poor conductivity (See Fig. 5.15) and this leads to poor cycling performance. Fig. 5.14-(c), (d) and (e) present charge/discharge curves of ZSC(F13%)V900 and ZSC(P13%)HN900 for the first three cycles. The ZSC(P15%) gives less 1st cycle discharge capacity which should attributes to its less SEI formation at potential higher than 0.1 V. Therefore, the 1st cycle coulombic efficiency of ZSC(P15%), 73.2%, is much higher than that of ZSC(F13%), 63.1%. Based on this improvement, an important inference can be drawn that reducing surface area by pitch carbon coating can effectively reducing 1st cycle irreversible capacity because of less SEI formation.

The 2nd and 3rd cycle give similar charge/discharge performance and reflect the fact that ZSC(F13%) and ZSC(P15%) has similar composition (i.e. Si and C content).
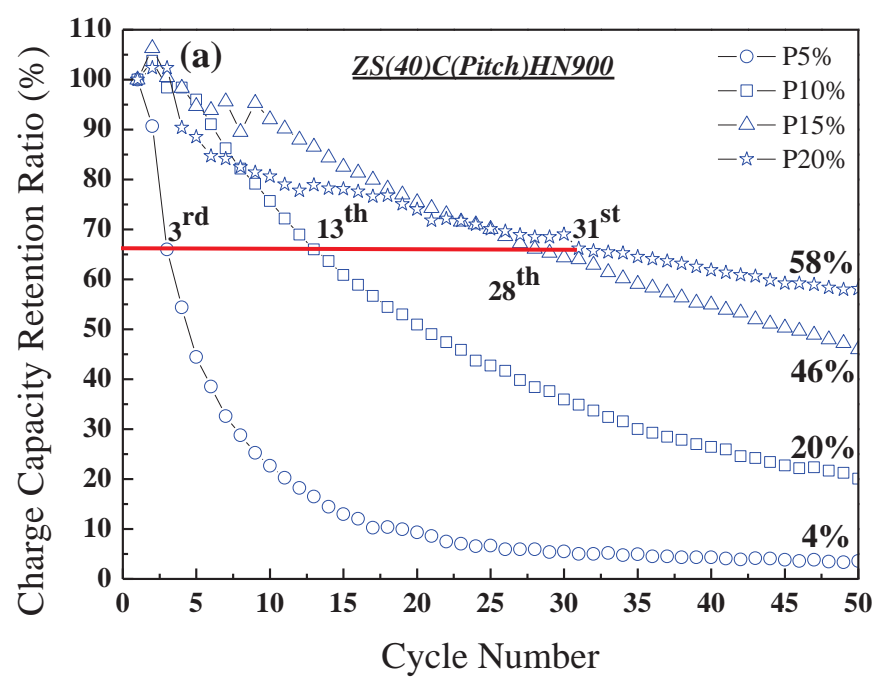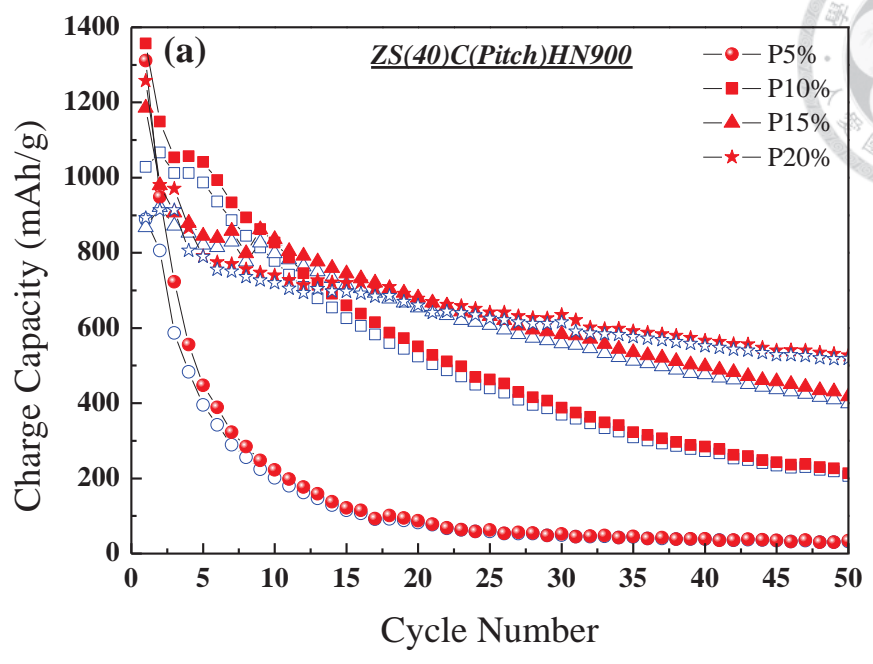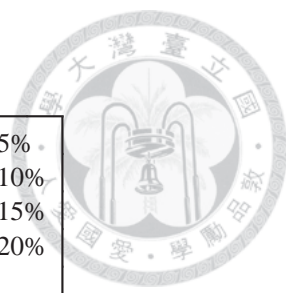
Figure 5.15 (a) Cycle life – capacity vs. cycle number plot of ZSC(Pitch) (b) Cycle life – charge capacity retention ratio vs. cycle number of ZSC(Pitch)
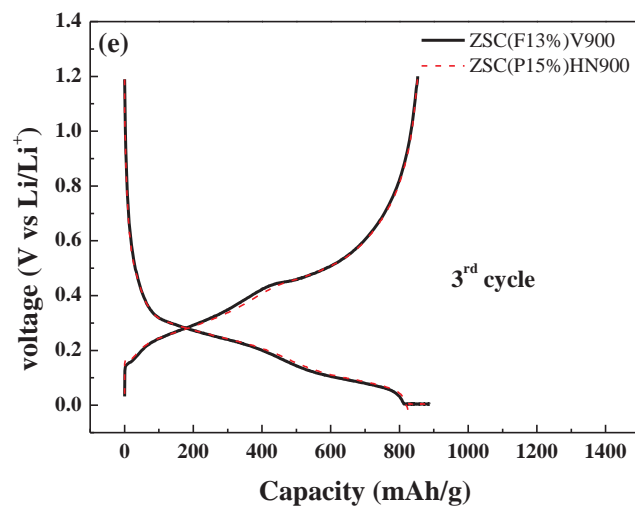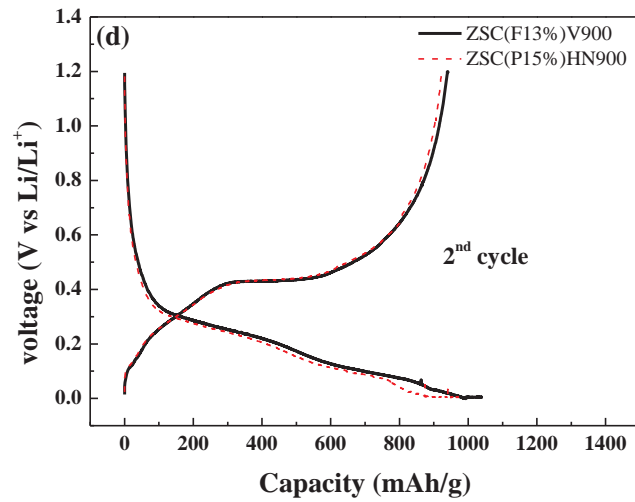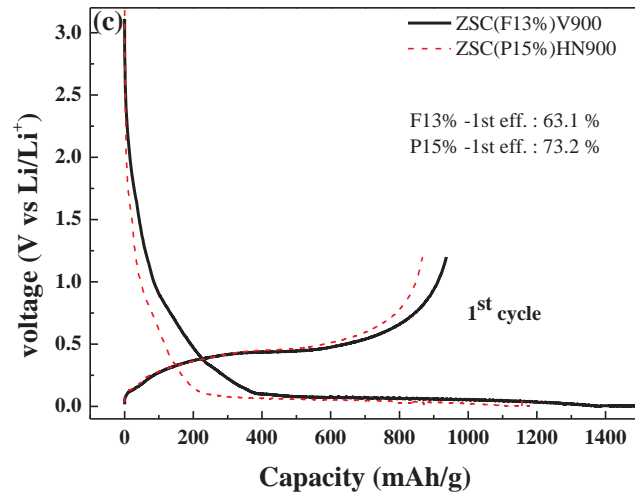
Figure 5.14-continued The (c) 1st (d) 2nd (e) 3rd charge/discharge curves of ZSC(F13%)V900 and ZSC(P15%)HN900.
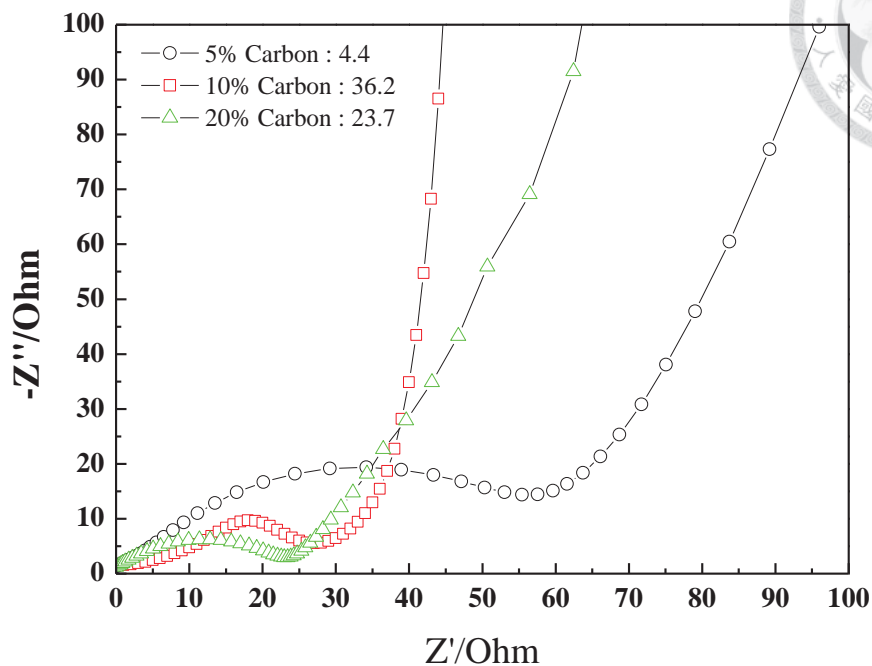
Figure 5.16 EIS spectra of ZSC(Pitch) with different content of carbon dissociated from pitch.

5.3.5 Combination of Fructose and Pitch as Carbon Source

The last part would be the combination of fructose and pitch as carbon sources. Fructose came from soaking gel with fructose solution which can make better carbon distribution in ZSC matrix and a better coverage on Si. Pitch coating is utilized to reduce the SEI formation due to large surface area. ZSC(Fructose+Pitch), denoted as ZSC(FP), is synthesized by pitch coating on ZSC(F)V500, (i.e. Z:0.01, S:40),and the calcination condition is 900℃ which is exactly the same as ZSC(Pitch) The overall carbon content is around 18 %.

From Fig. 5.16, the average coulombic efficiency is around 97% which is similar to ZSC(F)V900 and this also reflects the better carbon quality caused by high temperature treatment. The capacity retention ratio remains 70% at the 23rd cycle and

53% at the 50th cycle.

On the other hand, Fig. 5.17 has indicated that the overlithiation problem is sufficiently improved compared to ZSC(F)V900 shown in Fig. 5.12-(b). The 1st cycle charge capacity of ZSC(F)V900 is 937 mAh/g while that of ZSC(FP)HN900 is 850 mAh/g which just reflect the less Si content. However, the accumulated irreversible capacity (AIC) of ZSC(F)V900 is 1600 mAh/g while that of ZSC(FP)HN900 is just 1400 mAh/g. Note that AIC should consist of overlithiation by SEI formation and irreversible lithiation of amorphous silicon. The full lithitaion capacity of ZSC(F)V900 is ~ 2080 mAh/g and that of ZSC(FP)HN900 is 1870 mAh/g. The difference should relate to not only the more amorphous Si content but also more SEI formation in ZSC(F)V900. Therefore, pitch carbon coating is effective for solving overlithiation problem.

Figure 5.17 The capacity and coulombic efficiency vs. cycle number plot of ZS(40)C(FP).

Figure 5.18 The voltage vs. lithiation capacity plot of ZS(40)C(FP), including the 1st , 2nd , 3rd , 4th , 5th , 10th , 15th , 20th , 25th , 30th , 35th , 40th , 45th , and 50th cycle.

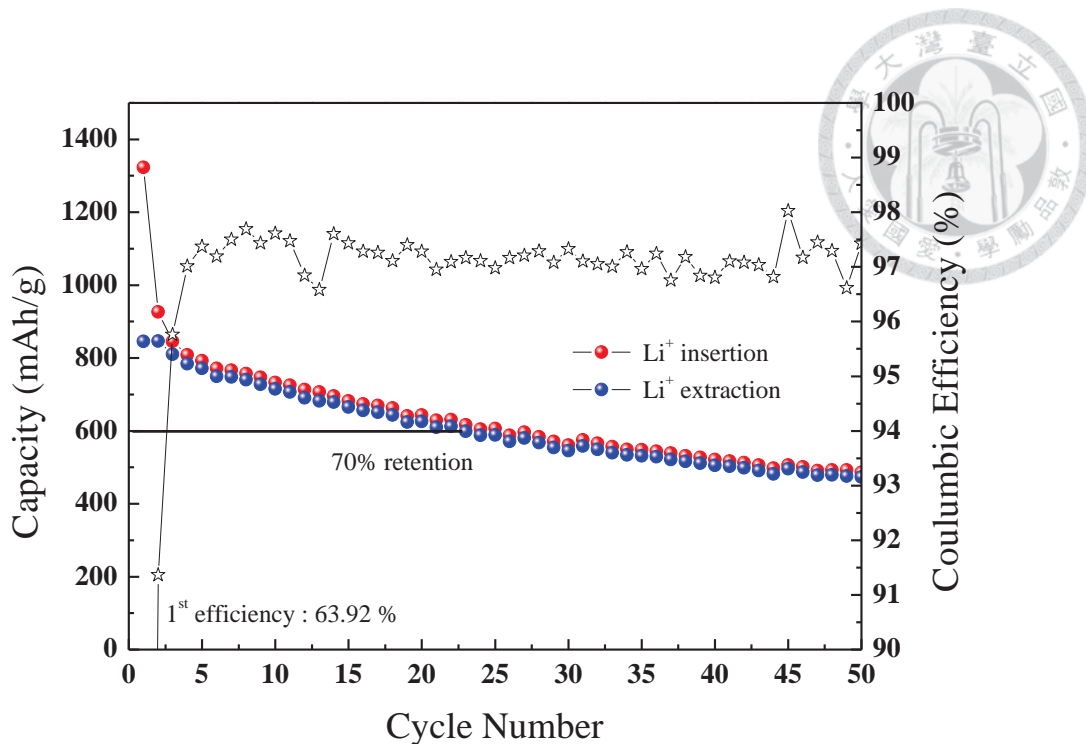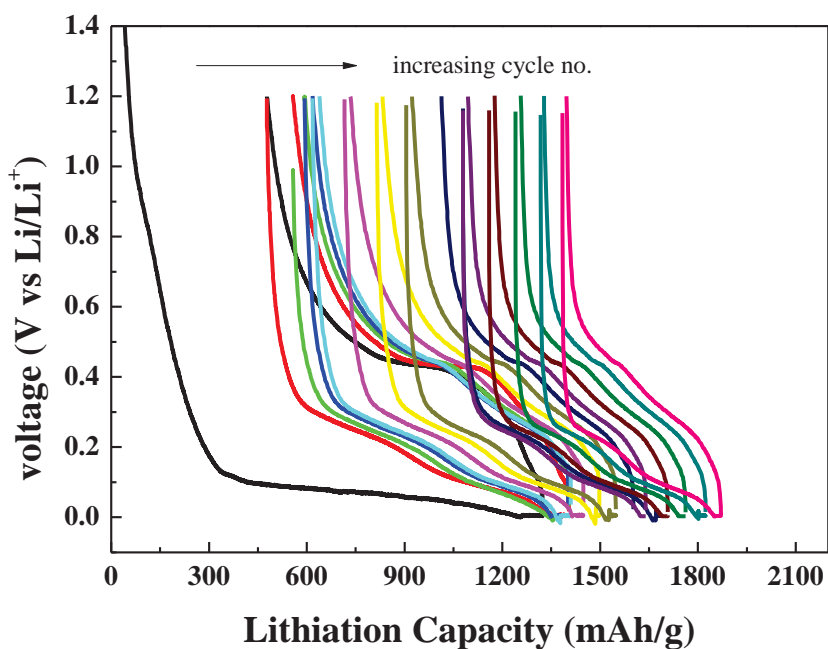## 5.4 Electrochemical Characterization of ZrO$_2$/100nmSi/C
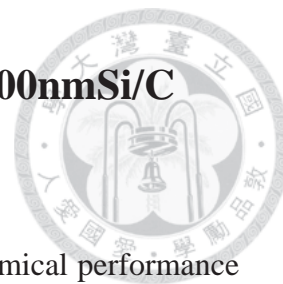
Since 40 nm Si and 100 nm Si performed different electrochemical performance (See chapter 5.2), ZrO$_2$/40nmSi/C and ZrO$_2$/100nmSi/C composites are separately discussed. From the previous experiments, porosity plays an important role in remaining good cycling performance and the fact should also be applicable to ZS(100)C matrix. Therefore, the concentration of precursor, Zr(OPr)$_4$, is 0.01M for ZSC samples in this chapter. Besides, the different carbon coating method with best operating condition (i.e. carbon content or heat treatment temperature) were conducted to see the effect on ZS(100)C matrix.

The capacity vs. cycle number plots of ZS(100)C(P15%)HN900, ZS(100)C(F)V900, and ZS(100)C(FP)HN900 were presented in Fig. 5.18, Fig. 5.19 and Fig. 5.20 in sequence. The 1st cycle coulombic efficiency conformed to our expectation that the one with pitch carbon coating gives less SEI formation due to less surface area. However, the coulombic efficiency performed afterward was not good enough compared to the other samples. The possible inference is that it needs more carbon contact immediately to improve its poor conductivity of 100 nm Si which we have known in chapter 5.2 (Fig. 5.3). Therefore, the other two samples with fructose carbon coating show better cyclic performance and presented around 97~98% coulumbic efficiency in the following cycles.

It's noteworthy that capacity retention for ZS(100)C is much better than ZS(40)C. For example, at the 50th cycle, ZS(100)C(FP)HN900 still remains 70% of the 1st cycle charge capacity which is higher than ZS(40)C(FP)HN900 which only remains 53% of the 1st cycle charge capacity. The huge improvement might attribute to its relatively large improvement on impedance, the comparative EIS analysis would be presented in

chapter 5.6. Although the capacity 100nm Si gives less capacity than 40nm does, it's still applicable for both economic and efficiency consideration (less) . Fig. 5.21 shows voltage vs. lithiation capacity plot of ZS(100)C(FP) which is similar to ZS(40)C(FP) in Fig. 5.17. The fact that overlithiation capacity of ZS(100)C(FP) is larger than ZS(40)C(FP) might be attributed to less stable SEI formation caused by thicker oxide layer of 100 nm Si
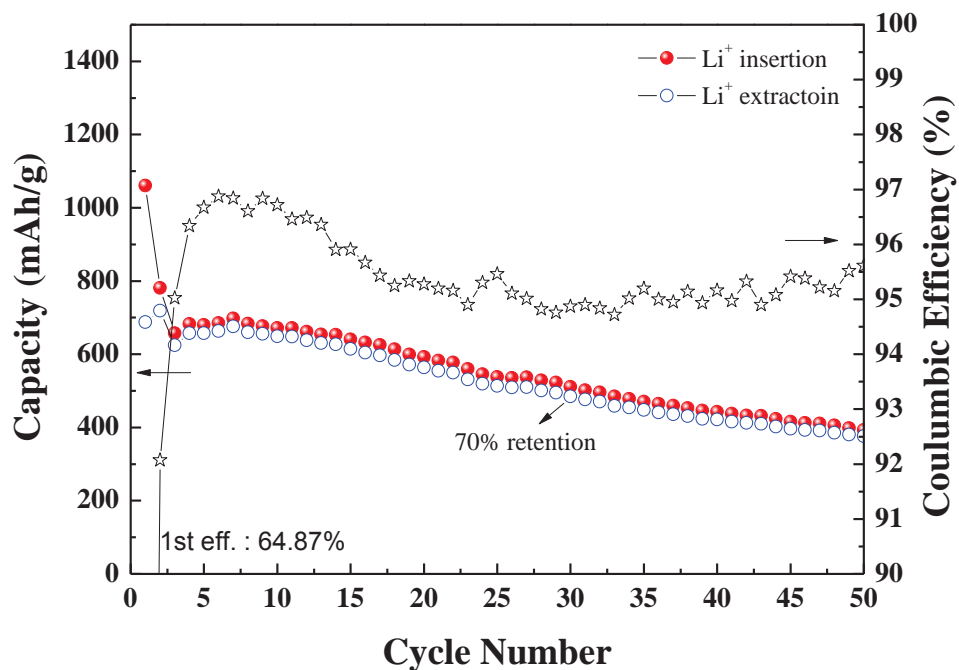
Figure 5.19 The capacity and coulombic efficiency vs. cycle number plot of ZS(100)C(P15%)HN900.
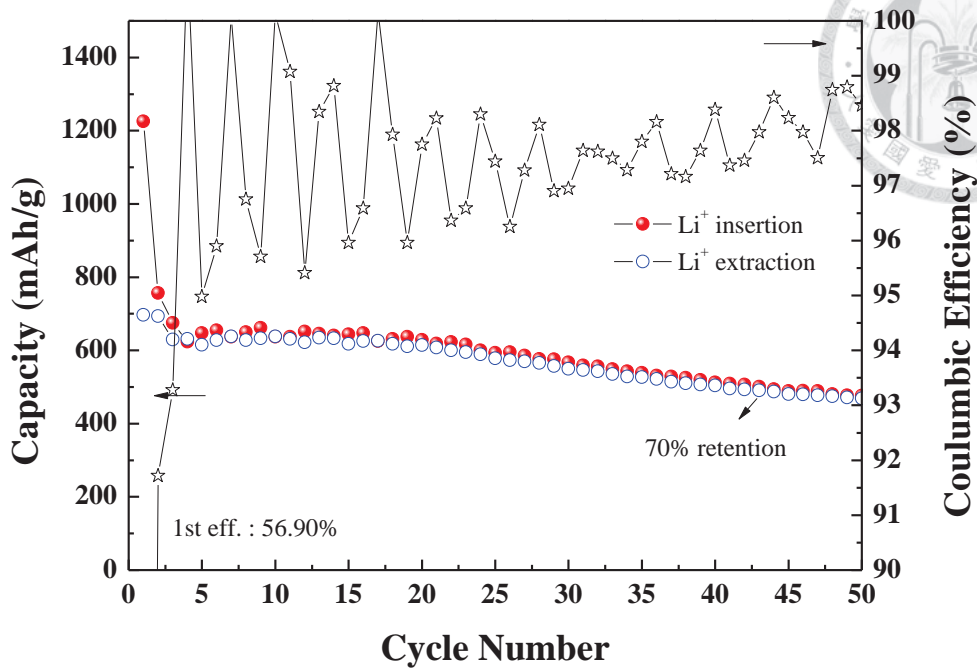
Figure 5.20 The capacity and coulombic efficiency vs. cycle number plot of ZS(100)C(F)V900.

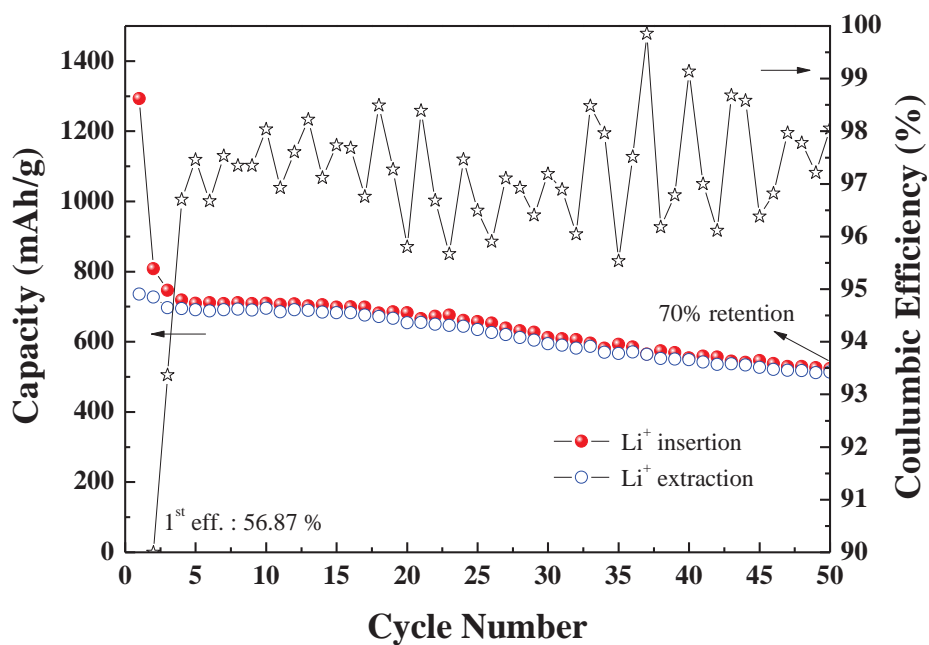**Figure 5.21** The capacity and coulombic efficiency vs. cycle number plot of ZS(100)C(FP)HN900.
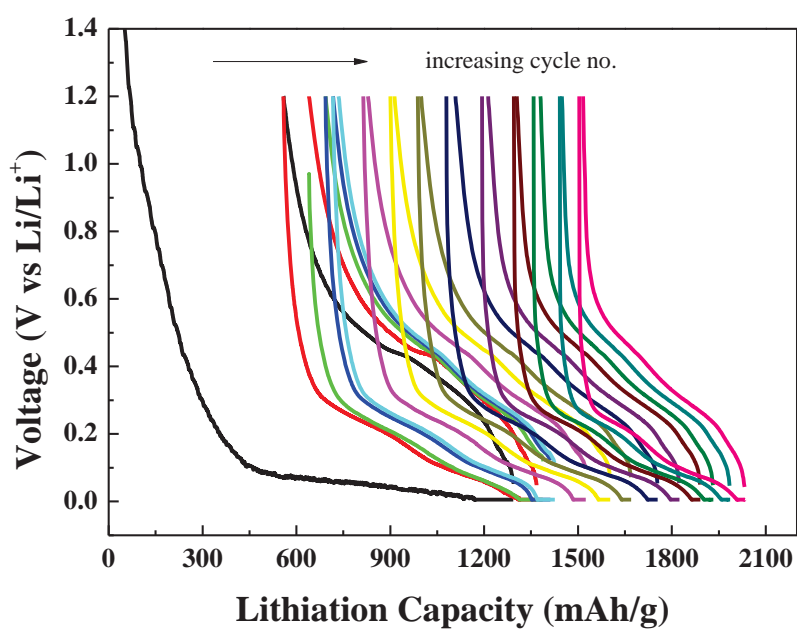
Figure 5.22 The voltage vs. lithiation capacity plot of ZS(100)C(FP)HN900, including the 1st , 2nd , 3rd , 4th , 5th , 10th , 15th , 20th , 25th , 30th , 35th , 40th , 45th , and 50th cycle.

5.5 Summary

The electrochemical performance of ZSC process has been illustrated in this chapter. The overall results are listed in Table 5.1 and Table 5.2 which have shown that combination of fructose and pitch carbon coating on ZSC matrix gave the best capacity retention results. Ths ZS(100)C(FP) can still keep 70% charge capacity retention to at 50th cycle while ZS(40)C(FP) still keep 56 % which are both much better than pure nano Si electrode. Besides, pitch carbon coating method can indeed decrease the 1st cycle irreversible capacity by reducing surface area of the porous structure. Table 5.3 and 5.4 give the tap density and electrode density comparison of ZS(40)C and ZS(100)C samples in this research.

In order to clarify the huge improvement of ZS(100)C composite, the comparative EIS analyses are listed in Fig. 5.22 and 5.23 separately. For ZS(40)C, we can see that the medium-high-f impedance which represented charge transfer impedance has been improved slightly; thus, the improvement on cyclic performance of ZS(40)C matrix should mainly attribute to its buffering structure from ZrO_2. On the other hand, we have known at chapter 5.2 that 100nm Si performs rather huge charge transfer resistance and diffusion resistance (low-f range) compared to 40nm Si. From Fig. 5.23, those resistances are sufficiently improved with immediate carbon-coating in overall matrix and even more, on Si "surface". Therefore, the guess which has been mentioned in chapter 5.2 that the poor electrochemical performance of 100nm Si might result from its thicker oxide layer or poor surface structure should be reasonable.

Figure 5.23 EIS spectra of different ZS(40)C composites (a) Nyquist plot (b) Bode plot.

The numbers in the legend indicate original x-axis intercept before shifting figure to

x=0. (f ranges from 0.01 Hz to 100,000 Hz).
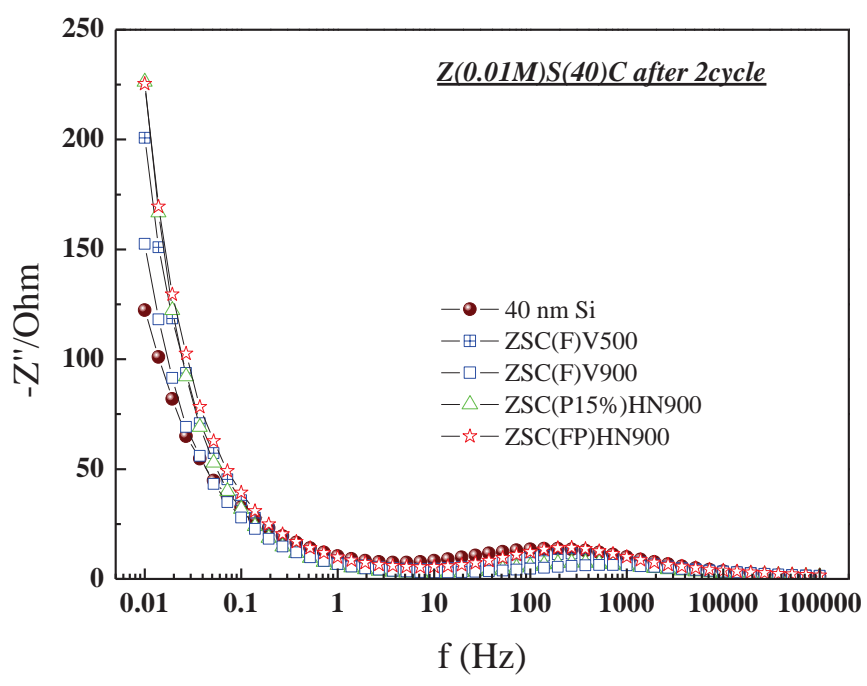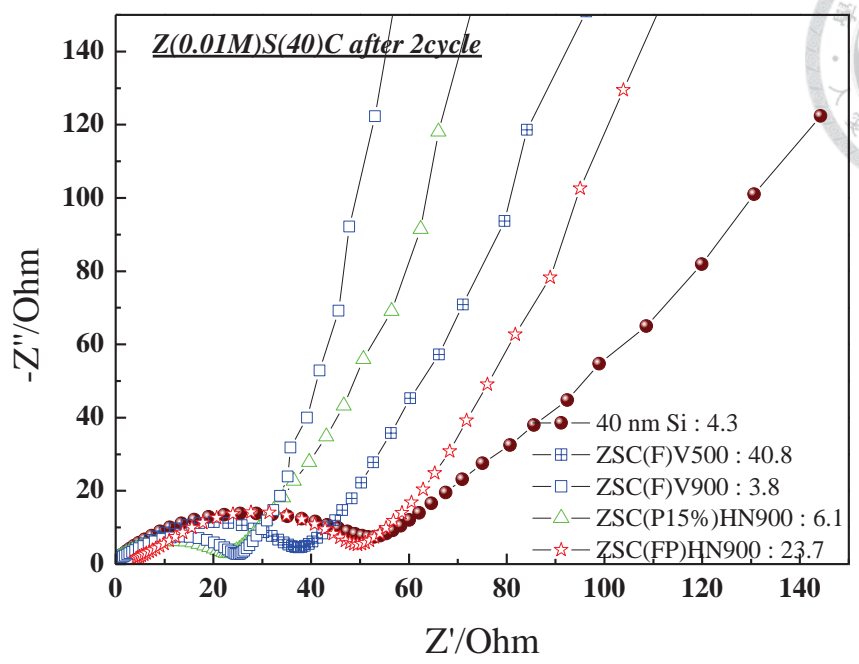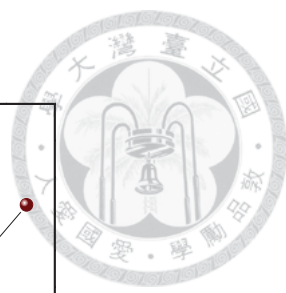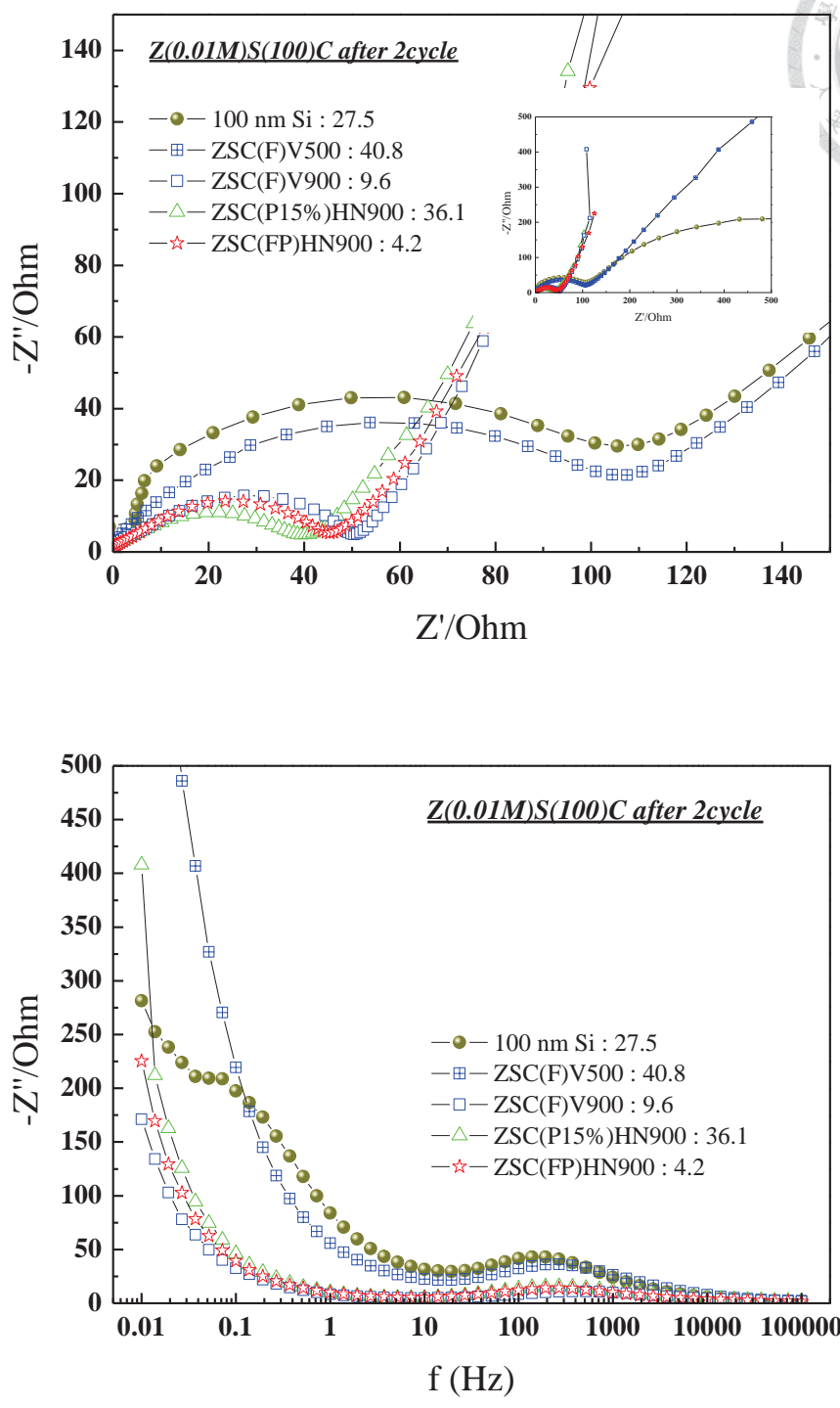
Figure 5.24 EIS spectra of different ZS(100)C composites (a) Nyquist plots (b) Bode plots. The numbers in the legend indicate original x-axis intercept before shifting figure to x=0. (f ranges from 0.01 Hz to 100,000 Hz).

Table 5.1 The comparison of ZrO_2/40nmSi/C composite (alginate as binder)

Sample Name	Carbon Content (w.t.%)	Theoretical Capacity[a] (mAh/g)	1st cycle DHG (mAh/g)	1st cycle CHG (mAh/g)	1st cycle Eff. (%)	50th cycle CHG capacity (mAh/g)	CCCR[b] get less than 70% at __ cycle
Pure 40nm Si	0	4200	3721	2988	80.3	378	3rd
Z(0.1)SC(F)V500	12	1310	1571	1024	65.2	212	5th
Z(0.01)SC(F)V500	13	1295	1456	1024	70.3	248	15th
Z(0.01)SC(F)V900	13	1295	1484	937	63.1	482	23rd
Z(0.01)SC(P5%)HN900	5	1413	1311	889	67.8	32	3rd
Z(0.01)SC(P10%)HN900	10	1340	1356	1028	75.8	206	12th
Z(0.01)SC(P15%)HN900	15	1265	1186	868	73.2	399	26th
Z(0.01)SC(P20%)HN900	20	1191	1256	892	71.0	518	27th
Z(0.01)SC(FP)HN900	18	1220	1323	846	63.9	473	24th

a : Except for pure 40 nm Si, theoretical capacity of other samples based on 1st DHG of pure 40 nm Si.

b: charge capacity retention ratio

Table 5.2 The comparison of ZrO_2/100nmSi/C composite (alginate as binder)

Sample Name	Carbon Content[*] (w.t.%)	Theoretical Capacity[a] (mAh/g)	1st cycle DHG (mAh/g)	1st cycle CHG (mAh/g)	1st cycle Eff. (%)	50th cycle CHG capacity (mAh/g)	CCCR[b] get less than 70% at __ cycle
Pure 100nm Si	0	4200	3063	1928	64.2	315	3rd
Z(0.01)SC(F)V500	~13	1066	1331	635	47.7	347	19th
Z(0.01)SC(F)V900	~12	1078	1225	697	56.9	469	44th
Z(0.01)SC(P15%)HN900	~15	1041	1061	688	64.9	376	31st
Z(0.01)SC(FP)HN900	~18	1005	1293	735	56.9	517	51st

a : Except for pure 100 nm Si, theoretical capacity of other samples based on 1st DHG of pure 100 nm Si.

b: charge capacity retention ratio

*: probably similar to ZS(40)C samples

Table 5.3 The tap density and electrode density of $ZrO_2/40nmSi/C$ electrodes

Sample Name	Tap Density (g/cm^3)	Electrode Density* (g/cm^3)
Pure 40nm Si	0.08	0.81
Z(0.1)SC(F)V500	0.32	0.97
Z(0.01)SC(F)V500	0.47	1.45
Z(0.01)SC(F)V900	0.51	1.32
Z(0.01)SC(P5%)HN900	0.48	1.35
Z(0.01)SC(P10%)HN900	0.47	1.34
Z(0.01)SC(P15%)HN900	0.43	1.40
Z(0.01)SC(P20%)HN900	0.43	1.20
Z(0.01)SC(FP)HN900	0.40	1.31
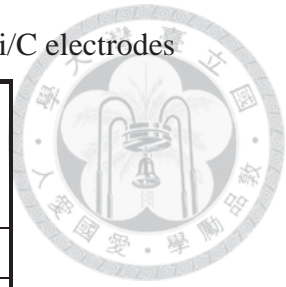
*: The solid-to-solvent weight ratio of slurry is around 0.25. The compression ratio of electrode is 30%-35%.

Table 5.4 The tap density and electrode density of $ZrO_2/100nmSi/C$ electrodes

Sample Name	Tap Density (g/cm^3)	Electrode Density* (g/cm^3)
Pure 100nm Si	0.12	0.91
Z(0.01)SC(F)V500	0.51	1.37
Z(0.01)SC(F)V900	0.54	1.33
Z(0.01)SC(P15%)HN900	0.47	1.40
Z(0.01)SC(FP)HN900	0.45	1.31

*: The solid-to-solvent weight ratio of slurry is around 0.25. The compression ratio of electrode is 30%-35%.

Chapter 6 Conclusions

In this study, the porous zircon-silicon-carbon (ZSC) matrix was made as anode material to solve severe volume expansion and poor conductivity problem during cycling. The overall logic of making ZSC composite was constructed step by step. Firstly, studying critical factors for making porous zirconia structure is necessary and on the basis of such experimental results, a porous ZS could be procurable. Besides, a novel idea of calcining gel in vacuum environment was realized and presented interesting results that it can retain more pore volume than under normal calcinations atmosphere, for instance, 3% H_2/N_2. Secondly, to solve the electronic insulation property, two different carbon coating method were adopted and each for different purpose. Pitch coating has indeed reduce the 1st cycle irreversibility by fulfilling pore volume which can sufficiently reduce surface area. Soaking gel in fructose solution showed better coverage of Si and more homogeneous carbon distribution which indeed improve the poor conductivity of silicon, especially for 100 nm Si.

Another important property of ZSC matrix should be its high tap density, which is around 4 to 5 times larger than nano Si. (ZSC: 0.4-0.5 g/cm^3,40 nm Si : 0.08 g/cm^3). Under the same conditions, like solid-to-solvent ratio of slurry, binder property, compression ratio, the higher tap density means larger electrode density. From Table 5.3 and 5.4, the electrode density of ZSC powder increases from 0.8 to 1.3-1.5 g/cm^3(increase more than 50%). Combination of better capacity retention and higher electrode density, ZSC powder gives much better volume-based capacity after 50th cycling. Finally, the space for improvement should be to find a better way to well disperse silicon particle in ZSC matrix which can definitely improve the cyclic performance.

References

[1] J. M. Tarascon and M. Armand, *Nature*, **414**, 359-367 (2001).

[2] B. Scrosati and J. Garche, *Journal of Power Sources*, **195**, 2419-2430 (2010).

[3] G. Pistoia, "Lithium batteries : science and technology", Kluwer Academic Publishers, Boston (2004).

[4] M. M. Thackeray, J. T. Vaughey, and L. M. L. Fransson, *Journal of the Minerals Metals & Materials Society*, **54**, 20-23 (2002).

[5] J. O. Besenhard, "Handbook of battery materials", Wiley-VCH, New York (1999).

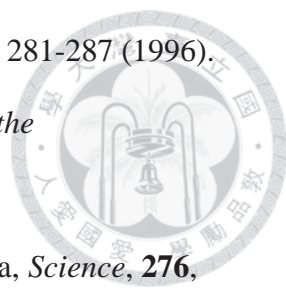[6] C. J. Wen and R. A. Huggins, *Journal of Solid State Chemistry*, **37**, 271-278 (1981).

[7] C.J. Brinker and G.W. Scherer, "Sol-gel science: The physics and chemistry of sol-gel processing", Academic Press: London (1990).

[8] H.S. Nalwa, "Handbook of Nanostructured Materials and Nanotechnology", Academic Press: New York, NY, USA, **5**, 501-575 (2000).

[9] J. D. Wright and Nico A.J.M. Sommerdijk, "Sol-gel materials: Chemistry and Applications", Amsterdam : Gordon and Breach Science Publishers (2001).

[10] J. Livage, M. Henry, J. D. Mackenzie and D. R. Ulnch, Eds. "Ultrastructure Processing of Advanced Ceramics", Willy: New York (1988).

[11] C. Sanchez, J. Livage, and M. Henry and F. Babonneau, *J. Non-Cryst. Solids*, **100**, 65 (1988).

[12] J. Livage, M. Henry and C. Sanchez, *Prog. Solid St. Chem.*, **18**, 259-341 (1988).

[13] R. Aelion, A. Loebel and F. Eirich, *J. Am. Chem. Soc.*, **72**, 5705 (1950).

[14] C. Sanchez and J. Livage, *New J. Chem.*, **14**, 513 (1990).

[15] J. C. Giuntini, W. Granier, J. V. Zanchetta, A. J., *Mater. Sci. Lett.*, **9**, 1383 (1990).

[16] J. Livage, C. Sanchez, M. Henry and S. Doeuff, *Solid State Ionics*, **32-33**, 633-638 (1989).

[17] F. Babboneau, A. Leaustic and J. Livage in *Better Ceramics Through Chemistry III*, Mater, Res. Soc. Symp. Rpoc. 121, edited by C.J. Brinker, D.E. Clark and D.R. Ulrich, p.317. Mater. Res. Soc. : Pittsburgh, Pa. (1988).

[18] A.J. Vega and G. W. Scherer, *J. Non-Cryst. Solids*, **111**, 153 (1989).

[19] R.D. Shoup, in Ultrastructure Processing of Advanced Ceramics, edited by J.D. Mackenzie and D.R. Ulrich, p.347. Wiley: New York (1988).

[20] A. H. Heuer, L. W. Hobbs, Eds., *Adv. Ceram.*, **3**, 475 (1981).

[21] F. Gallino , C. D. Valentin and G. Pacchioni, *Phys. Chem. Chem. Phys.*, **13**, 17667-17675 (2011).

[22] Ralph Nielsen "Zirconium and Zirconium Compounds" in Ullmann's Encyclopedia of Industrial Chemistry, Wiley-VCH, Weinheim (2005).

[23] G. Yi and M. Sayer, *Journal of Sol-Gel Science and Technology*, **6**, 65-74 (1996).

[24] J. Mrowiec-Bialon and L. Pajak, *Journal of Non-Crystalline Solids*, **225**, 115-119 (1998).

[25] C. Stocker and A. Baiker, *Journal of Non-Crystalline Solids,* **223**, 165-178 (1998).

[26] C. Stocker, M. Schneider, and A. Baiker, *Journal of Porous Materials*, **2**, 171-183 (1995).

[27] B. Scrosati, *Nature*, **373**, 557-558 (1995).

[28] M. Wakihara, *Materials Science & Engineering R-Reports*, **33**, 109-134 (2001).

[29] W. A. V. Schalkwijk and B. Scrosati, *Advances in lithium-ion batteries*, Kluwer Academic/Plenum Publishers, New York, NY (2002).

[30] M. S. Whittingham, *Science*, **192**, 1126-1127 (1976).

[31] A. N. Dey, *Journal of the Electrochemical Society*, **118**, 1547-1549 (1971).

[32] R. A. Sharma and R. N. Seefurth, *Journal of the Electrochemical Society*, **123**, 1763-1768 (1976).

[33] B. A. Boukamp, G. C. Lesh, and R. A. Huggins, *Journal of the Electrochemical Society*, **128**, 725-729 (1981).

[34] C. Vandermarel, G. J. B. Vinke, and W. Vanderlugt, *Solid State Communications*, **54**, 917-919 (1985).

[35] J. W. Kim, J. H. Ryu, K. T. Lee, and S. M. Oh, *Journal of Power Sources*, **147**, 227-233 (2005).

[36] W. J. Weydanz, M. Wohlfahrt-Mehrens, and R. A. Huggins, *Journal of Power Sources*, **81**, 237-242 (1999).

[37] B. Gao, S. Sinha, L. Fleming, and O. Zhou, *Advanced Materials*, **13**, 816-819 (2001).

[38] C. J. Wen and R. A. Huggins, *Journal of Solid State Chemistry*, **37**, 271-278 (1981).

[39] J. Saint, M. Morcrette, D. Larcher, L. Laffont, S. Beattie, J. P. Peres, D. Talaga, M. Couzi, and J. M. Tarascon, *Advanced Functional Materials*, **17**, 1765-1774 (2007).

[40] G. X. Wang, J. Yao, and H. K. Liu, *Electrochemical and Solid State Letters*, **7**, A250-A253 (2004).

[41] H. Li, X. J. Huang, L. Q. Chen, G. W. Zhou, Z. Zhang, D. P. Yu, Y. J. Mo, and N. Pei, *Solid State Ionics*, **135**, 181-191 (2000).

[42] P. Limthongkul, Y. I. Jang, N. J. Dudney, and Y. M. Chiang, *Acta Materialia*, **51**, 1103-1113 (2003).

[43] A. Netz, R. A. Huggins, and W. Weppner, *Journal of Power Sources*, **119**, 95-100

(2003).

[44] T. D. Hatchard and J. R. Dahn, *Journal of the Electrochemical Society*, **151**, A838-A842 (2004).

[45] J. Li and J. R. Dahn, *Journal of the Electrochemical Society*, **154**, A156-A161 (2007).

[46] J. H. Ryu, J. W. Kim, Y. E. Sung, and S. M. Oh, *Electrochemical and Solid State Letters*, **7**, A306-A309 (2004).

[47] C. M. Park, J. H. Kim, H. Kim, and H. J. Sohn, *Chemical Society Reviews*, **39**, 3115-3141 (2010).

[48] W. R. Liu, Z. Z. Guo, W. S. Young, D. T. Shieh, H. C. Wu, M. H. Yang, and N. L. Wu, *Journal of Power Sources*, **140**, 139-144 (2005).

[49] M. Holzapfel, H. Buqa, W. Scheifele, P. Novak, and F. M. Petrat, *Chemical Communications*, 1566-1568 (2005).

[50] M. Holzapfel, H. Buqa, F. Krumeich, P. Novak, F. M. Petrat, and C. Veit, *Electrochemical and Solid State Letters*, **8**, A516-A520 (2005).

[51] S. D. Beattie, D. Larcher, M. Morcrette, B. Simon, and J. M. Tarascon, *Journal of the Electrochemical Society*, **155**, A158-A163 (2008).

[52] D. Larcher, S. Beattie, M. Morcrette, K. Edstroem, J. C. Jumas, and J. M. Tarascon, *Journal of Materials Chemistry*, **17**, 3759-3772 (2007).

[53] M. Winter and J. O. Besenhard, *Electrochimica Acta*, **45**, 31-50 (1999).

[54] M. N. Obrovac and L. J. Krause, *Journal of the Electrochemical Society*, **154**, A103-A108 (2007).

[55] H. Li, X. J. Huang, L. Q. Chen, Z. G. Wu, and Y. Liang, *Electrochemical and Solid State Letters*, **2**, 547-549 (1999).

[56] Z. P. Guo, J. Z. Wang, H. K. Liu, and S. X. Dou, *Journal of Power Sources*, **146**, 448-451 (2005).

[57] J. Yang, M. Winter, and J. O. Besenhard, *Solid State Ionics*, **90**, 281-287 (1996).

[58] J. Yang, Y. Takeda, N. Imanishi, and O. Yamamoto, *Journal of the Electrochemical Society*, **146**, 4009-4013 (1999).

[59] Y. Idota, T. Kubota, A. Matsufuji, Y. Maekawa, and T. Miyasaka, *Science*, **276**, 1395-1397 (1997).

[60] I. A. Courtney, W. R. McKinnon, and J. R. Dahn, *Journal of the Electrochemical Society*, **146**, 59-68 (1999).

[61] U. Kasavajjula, C. S. Wang, and A. J. Appleby, *Journal of Power Sources*, **163**, 1003-1039 (2007).

[62] H. C. Wu, M. H. Yang, N. L. Wu, and W. R. Liu, "Anode materials of lithium secondary battery and method of fabricating the same," US patent 2006147797 (A1) (2006).

[63] D.Q. Shi, J.P. Tu, Y.F. Yuan, H.M. Wu, Y. Li, X. B. Zhao, *Journal of Electrochemistry Communications*, **8**, 1610-1614 (2006).

[64] X. L. Wang, J.P. Tu, J. Y. Xiang, and X. H. Huang, *Funct. Mater. Lett.* **2**, 23 (2009).

[65] H. Y. Lee and S. M. Lee, *Electrochemistry Communications*, **6**, 465-469 (2004).

[66] G. X. Wang, J. H. Ahn, J. Yao, S. Bewlay, and H. K. Liu, *Electrochemistry Communications*, **6**, 689-692 (2004).

[67] T. Hasegawa, S. R. Mukai, Y. Shirato, and H. Tamon, *Carbon*, **42**, 2573-2579 (2004).

[68] A. Magasinski, P. Dixon, B. Hertzberg, A. Kvit, J. Ayala, and G. Yushin, *Nature Materials*, **9**, 353-358 (2010).

[69] W. R. Liu, M. H. Yang, H. C. Wu, S. M. Chiao, and N. L. Wu, *Electrochemical and Solid State Letters*, **8**, A100-A103 (2005).

[70] N. Ding, J. Xu, Y. X. Yao, G. Wegner, I. Lieberwirth, and C. H. Chen, *Journal of*

Power Sources, **192**, 644-651 (2009).

[71] I. Kovalenko, B. Zdyrko, A. Magasinski, B. Hertzberg, Z. Milicev, R. Burtovyy, I. Luzinov, G. Yushin, *Science* 334, 75 (2011).

[72] "http://web.pdx.edu/~pmoeck/phy381/Topic5a-XRD.pdf.".

[73] W. R. Liu, J. H. Wang, H. C. Wu, D. T. Shieh, M. H. Yang, and N. L. Wu, *Journal of the Electrochemical Society*, **152**, A1719-A1725 (2005).

[74] Y. M. Lin, H. C. Wu, Y. C. Yen, and N. L. Wu, *Journal of The Electrochemical Society*, 152 8 A1526-A1532 (2005)

Appendix A

Figure A.1 The ZrO_2 gels with different concentration of precursor dried to certain state. (ZrO_2 (0.01M) just cracked and others were not far from cracking)

Figure A.2 The collected ZrO_2/Si gel from filtration process.

Figure A.3 (left) The viscous gel property of ZrO2(0.01M)-Dry 23hr (right) The crack image of ZrO2(0.01M)-Dry 23hr.
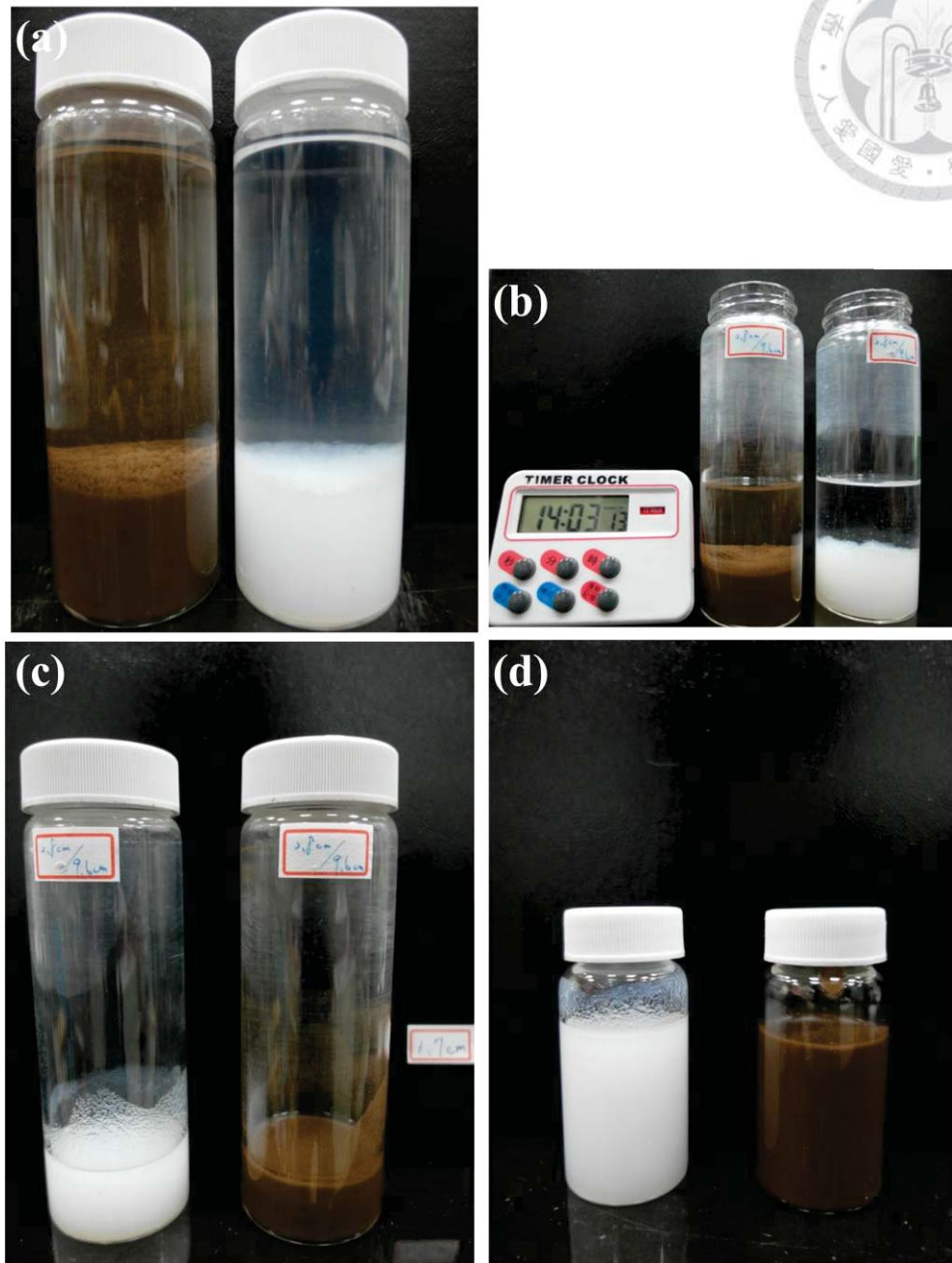
Figure A.4 The drying process illustration (a) after adding water to induce sol-gel transition and keep static for 30 min (b) drying after 14 hr (c) residual gel (d) decant the solution in (c) to smaller batch.

Figure A.5 40 nm Si and 100 nm Si disperse in 2-propanol. The solution color also reflects their different color in appearance.

Figure A.6 (Left) Z(0.1), Z(0.01)S(40), and Z(0.01) gel from left to right. (Right) the huge difference of left volume when crack just formed of Z(0.1) and Z(0.01) gel samples.
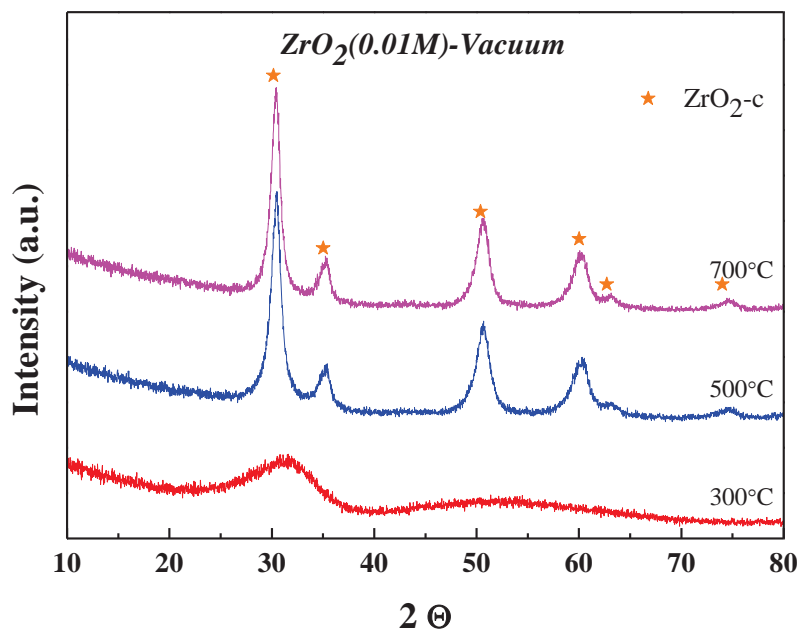
Appendix B

Figure B.1 XRD patterns of ZrO_2(0.01M) gel calcined at different temperature for 15 min under vacuum condition.

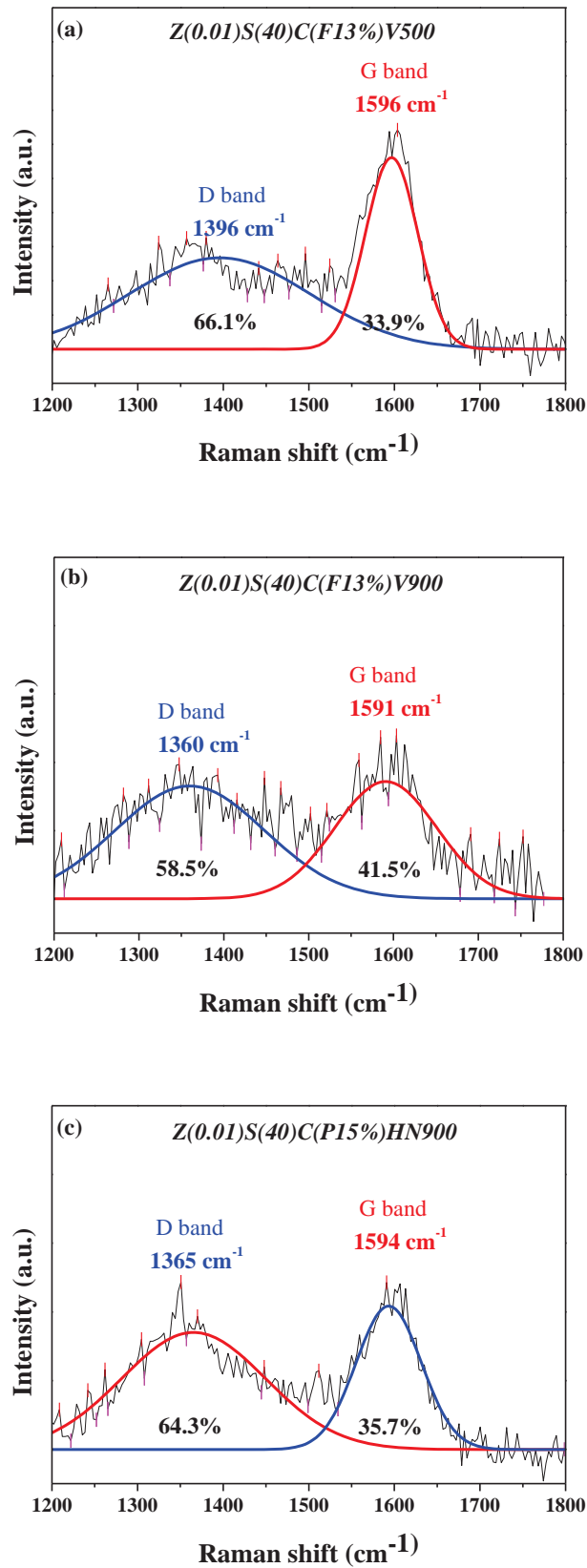**Figure B.2** Raman spectra showing the bonding structure of the C-coatings of (a) ZSC(F13%)V500, (b) ZSC(F13%)V900, and (c) ZSC(P15%)HN900.